Iowa State University
Digital Repository

Retrospective Theses and Dissertations

Iowa State University Capstones, Theses and Dissertations

2005

Synergy between chemical dissolution and mechanical abrasion during chemical mechanical polishing of copper

Wei Che
Iowa State University

Follow this and additional works at: https://lib.dr.iastate.edu/rtd

Part of the Applied Mechanics Commons

Recommended Citation
Che, Wei, "Synergy between chemical dissolution and mechanical abrasion during chemical mechanical polishing of copper " (2005). *Retrospective Theses and Dissertations*. 1229.
https://lib.dr.iastate.edu/rtd/1229

This Dissertation is brought to you for free and open access by the Iowa State University Capstones, Theses and Dissertations at Iowa State University Digital Repository. It has been accepted for inclusion in Retrospective Theses and Dissertations by an authorized administrator of Iowa State University Digital Repository. For more information, please contact digirep@iastate.edu.

المنارة للاستشارات

www.manaraa.com

Synergy between chemical dissolution and mechanical abrasion during chemical mechanical polishing of copper

by

Wei Che

A dissertation submitted to the graduate faculty

in partial fulfillment of the requirements for the degree of

DOCTOR OF PHILOSOPHY

Major: Mechanical Engineering

Program of Study Committee:
Ashraf Bastawros, Co-major Professor
Abhijit Chandra, Co-major Professor
Pranav Shrotriya
Thomas J. Rudolphi
Brian Gleeson

Iowa State University
Ames, Iowa
2005

Copyright © Wei Che, 2005. All rights reserved.

UMI Number: 3172205

INFORMATION TO USERS

The quality of this reproduction is dependent upon the quality of the copy submitted. Broken or indistinct print, colored or poor quality illustrations and photographs, print bleed-through, substandard margins, and improper alignment can adversely affect reproduction.

In the unlikely event that the author did not send a complete manuscript and there are missing pages, these will be noted. Also, if unauthorized copyright material had to be removed, a note will indicate the deletion.

UMI®

UMI Microform 3172205

Copyright 2005 by ProQuest Information and Learning Company.

All rights reserved. This microform edition is protected against unauthorized copying under Title 17, United States Code.

ProQuest Information and Learning Company
300 North Zeeb Road
P.O. Box 1346
Ann Arbor, MI 48106-1346

Graduate College
Iowa State University

This is to certify that the doctoral dissertation of

Wei Che

has met the dissertation requirements of Iowa State University

Signature was redacted for privacy.

Co-major Professor

Signature was redacted for privacy.

Co-major Professor

Signature was redacted for privacy.

For the Major Program

Table of Contents

List of Figures vii

List of Tables x

Abstract xi

Chapter 1 Introduction 1

1.1 CMP Polisher 4

1.1.1 Linear polisher 4

1.1.2 Orbital polisher 5

1.1.3 Pad feed polisher 6

1.2 CMP Process Variables and Their Associated Effects 6

1.2.1 Abrasive particles 6

1.2.2 Slurry 8

1.2.3 Pad 11

1.2.4 Carriers 13

1.3 Common CMP Defects 13

1.3.1 Metallic residuals and associated dishing and erosion 13

1.3.2 Surface defects and scratches 14

1.3.3 Pin-holes and microcracks 14

1.3.4 Corrosion and pitting 15

1.4 Existing Models for CMP Process 15

1.5 Objective 19

1.6 Thesis Outline 20

1.7 References 21

Chapter 2 A Scratch Intersection Model of Material Removal during Chemical Mechanical Planarization (CMP) 25

2.1 Abstract 25

2.2 Introduction 26

2.3 Material Removal Model Development 29

2.3.1 Determination of the average local pressure per asperity 30

2.3.2 Determination of the normal force per particle 34

2.3.3 Determination of indentation depth of a single abrasive particle 37

2.3.4 Estimation of the characteristic detached length, ℓ_c during scratch intersection 38

2.3.5 Determination of the volume of material removed in an intersection 40

2.3.6 Determination of the number of intersections per unit area per revolution 41

2.3.7 Estimation of the MRR 44

2.4 Comparison to Experimental Observations 47

2.4.1 Preston constant and variation of MRR with pressure and velocity 47

2.4.2 Variation of MRR with particle size and concentration 50

2.5 Discussion and Concluding Remarks 54

2.6 References 56

Chapter 3 Material Removal Mechanism Part I: Chemical Assisted Mechanical Abrasion by a Softened Layer Formation 60

3.1 Literature Review 60

3.2 Sample Preparation 63

3.3 Experimental Investigation Utilizing Nano Scratches 64

3.3.1 Mechanism of running scratch test by nano-indenter 66

3.3.2 Experimental procedure and data analysis of running nano-scratch 66

3.3.3 Experimental results for scratch data 74

3.4 Analytical Model for Scratch 82

3.4.1 Results for 0.6wt% NH_4OH slurry 84

3.4.2 Results for 5wt% H_2O_2 slurry 86

3.4.3 Results for 1.0wt% HNO_3+ 0.5wt% BTA slurry 87

3.5 Continuous Stiffness Measurement 88

3.5.1 Experimental procedure 89

3.5.2 Dynamic load function 89

3.5.3 Experimental results 91

3.6 Numerical Simulation for Single-Layer Structure 92

3.7 Conclusions 95

3.8 References 96

Chapter 4 Material Removal Mechanism Part II: Mechanically Assisted Chemical Dissolution by Introducing Residual Stress in the Sub Surface through Wear Test 100

4.1 Literature Review 100

4.2 Experimental Modeling by Nano Wear Experiment 102

4.2.1 How nano-indenter do wear test 103

4.2.2 Experiment procedures of nano-wear test 104

4.2.3 Data analysis of experimental data for wear test 106

4.3 Experimental Results 111

4.3.1 Chemical exposure followed by mechanical wear 111

4.3.2 Mechanical wear followed by chemical exposure 112

4.3.3 Wear test III (multi-pass wear test-chemical dissolution-multi-pass wear test, 0.6wt% NH4OH slurry) 116

4.4 Existing Thermodynamic Model for Wavelength Selectivity 118

4.5 Numerical Simulation for Residual Stress under Double Indentation 120

4.5.1 Numerical result for residual stress. 120

4.5.2 Analytical estimation for residual stress under single indentation 122

4.5.3 Experimental results for wavelength selectivity 123

4.6 Conclusion 125

4.7 References 126

Chapter 5 Conclusion and Future Work 128

5.1 Conclusion 128

5.1.1 Phenomenological material removal models 128

5.1.2 Synergy between mechanical abrasion and chemical dissolution 129

5.2 Future Work 132

Appendix 1: Experimental Scratch Data and Film Thickness Measurement Data 135

Appendix 2: Tip Radius Calibration. 141

List of Figures

Fig 1.1 Schematic of orbital CMP tool 3

Fig 1.2 Schematic of linear polisher 5

Fig 1.3 Schematic of pad feed polisher 5

Fig 1.4 MRR variation with particle size 7

Fig 1.5 MRR variation with particle size 7

Fig 1.6 Schematic of Poubaix diagram for the Cu-H_2O system 10

Fig 1.7 Copper scratch examples (a) razor, (b) chatter, and (c) skipping 14

Fig 2.1 An AFM scan of a representative scratch cross-section 28

Fig 2.2 Flow chart for calculating the MRR in a typical CMP process 30

Fig 2.3 SEM image of an IC1000 pad 31

Fig 2.4 Schematic representation of the multi-scale of the wafer/pad contact 33

Fig 2.5 Characteristic detachment length variation with the scratch depth 38

Fig 2.6 Schematic of scratch intersection 39

Fig 2.7 Schematic of volume of detached flake at intersection 39

Fig 2.8 A schematic of particle motion in CMP process 42

Fig 2.9 A schematic of particles train motion relative to unit cell 43

Fig 2.10 MRR variation with pressure for copper CMP data 49

Fig 2.11 MRR variation with velocity for Copper CMP) 49

Fig 2.12 MRR variation with particle size for a fixed 2wt% concentration 51

Fig 2.13 MRR variation with concentration for particle size of 0.2 μm 51

Fig 2.14 MRR variation with particle size for a fixed 10wt% concentration 52

Fig 2.15 MRR variation with particle size 53

Fig 3.1 Schematic of nano-indenter 2D transducer 66

Fig 3.2 Schematic of scratch load function 68

Fig 3.3 Output of scratch profile (upward) 70

Fig 3.4 Output of scratch profile (downward) 70

Fig 3.5 Schematic of scratch motion on the surface (a) upwards (b) downwards 72

Fig 3.6 Variation of mean scratch depth with normal force (600s etch) 75

Fig 3.7 Variation of mean scratch depth with tangential force (600s etch) 76

Fig 3.8 Comparison between different chemical exposure time 77

Fig 3.9 Variation of mean scratch depth with tangential force 78

Fig 3.10 Variation of mean scratch depth with normal force (5wt% H_2O_2) 79

Fig 3.11 Variation of mean scratch depth with tangential force (5wt% H_2O_2) 80

Fig 3.12 Experimental scratch data for 600s (1.0wt% HNO_3+ 0.5wt% BTA) 81

Fig 3.13 Schematic of abrasive particle-workpiece contact 82

Fig 3.14 XPS signal intensity ratio with take of angle from Cu surface 85

Fig 3.15 Schematic for ramping quasi-static load 90

Fig 3.16 Variation of normalized modulus with indentation depth 91

Fig 3.17 FEM Model description for axisymmetric indentation 93

Fig 3.18 Mesh for the axisymmetric model 94

Fig 3.19 Normalized modulus with normalized indentation depth 95

Fig 4.1 Schematic of nano wear test 103

Fig 4.2 Tilt correction for wear surface profile 107

Fig 4.3 A typical line profile showing wear depth 108

Fig 4.4 Schematic of region selection for wear data analysis 109

Fig 4.5 Experimental data for mechanism I test 112

Fig 4.6 Variation of wear depth with exposure time for mechanism II test 113

Fig 4.7 Variation of roughness with exposure time for mechanicsm II test 114

Fig 4.8 Experimental data for mechanism II (1wt% HNO_3 +0.5wt%BTA) 116

Fig 4.9 Wear depth evolution with number of wear pass (0.6wt% NH_4OH) 117

Fig 4.10 2-D double-indent FEM simulation model 121

Fig 4.11 Estimation of residual stress under wear track by FEM simulation 122

Fig 4.12 Experimental data showing roughness evolution (1wt% HNO_3 +0.5wt%BTA) 124

Fig 4.13 Experimental data showing roughness evolution (0.6wt% NH_4OH) 124

Fig appendix 2.1 Tip shape 141

List of Tables

Table 2.1 Range of parameters for Eq(2g.4) 48

Table 3.1 Experimental result for 0.6wt% NH_4OH 84

Table 3.2 XPS result for 0.6wt% NH_4OH 86

Table 3.3 Experimental result for 5wt% H_2O_2 86

Table 3.4 Experimental result for 1.0wt% HNO_3+ 0.5wt% BTA 88

Table Appendix 1.1 Scratch data for 600s exposure time (0.6wt% NH_4OH) 135

Table Appendix 1.2 Scratch data for 300s exposure time (0.6wt% NH_4OH) 135

Table Appendix 1.3 Scratch data for 90s exposure time (0.6wt% NH_4OH) 136

Table Appendix 1.4 Film thickness result for 600s exposure time 136

Table Appendix 1.5 Film thickness result for 300s exposure time 137

Table Appendix 1.6 Film thickness result for 90s exposure time 137

Table Appendix 1.7 Scratch data for 5wt% H_2O_2 137

Table Appendix 1.8 Film thickness result for 300s exposure time 138

Table Appendix 1.9 Film thickness result for 150s exposure time 139

Table Appendix 1.10 Film thickness result for 75s exposure time 139

Table Appendix 1.11 Scratch data for 1.0wt%HNO_3+0.5wt%BTA 139

Table Appendix 1.12 Film thickness results 140

Abstract

Copper has been chosen as an interconnecting material in integrated circuits (IC) because of its low resistivity and high electromigration resistance compared to aluminum and aluminum alloy interconnects. It has been shown recently that the patterning difficulty of copper is resolved by the dual damascene technique, combined with a chemical/mechanical planarization (CMP) process. CMP is becoming a very promising mainstream semiconductor processing method because of its demonstrated ability to achieve better local and global planarization for various materials, such as silicon oxide, tungsten and copper. However, the CMP process is influenced by a set of factors, which lead to a poor understanding of the material removal mechanisms involved during the CMP. The absence of reliable physically based models inhibits the migratability of the lab scale experiments to industrial practice. This work addresses the synergistic role of chemical dissolution rate (CDR) and mechanical abrasion rate (MAR) on the material removal mechanisms during CMP process.

Initial in situ wear test in a chemically active slurry showed an increased material removal rate (MRR) relative to dry wear test. To understand the synergistic effects between CDR and MAR, two plausible mechanisms of material removal; (i) chemical dissolution enhances mechanical abrasion and (ii) mechanical abrasion accelerates chemical dissolution, were investigated. In addition, a phenomenological material detachment mechanism based on scratch intersections to understand the role of consumables (e.g. slurry particle concentration and size, pad surface morphology and stiffness) and the process parameters (e.g. applied pressure and relative sliding velocity) on the MRR was formulated. The proposed models, through their mechanistic description, will facilitate an exploration of the design space and

identification of realistic CMP process domains. Moreover, it would enable understanding the root causes of defect generation mechanism and render remedies for yield improvements.

For the mechanism of mechanical abrasion enhanced by chemical dissolution, it is proposed that a soft layer of chemical products is formed on top of the polished surface due to chemical reaction at a rate much faster than the mechanical abrasion rate. This is then followed by a gentle mechanical abrasion of that soft layer. A combined experimental and modeling technique was devised to understand the mechanical properties of the soft layer formed due to chemical exposure in the CMP. The developed experimental approach, in collaboration with Hysitron Inc., utilized nano-scratch and a nano-dynamic mechanical analysis (DMA) tests under dry (without chemical exposure) or wet conditions (with chemical exposure). The methodology combines the limit analysis solution of surface plowing under a spherical traveling indenter to analyze the nano-scratch experimental measurements, in order to deduce the ratio of the film (soft layer) yield strength to the substrate yield strength as well as the film thickness. A nano-dynamic mechanical analysis (DMA) test was performed. The measured apparent modulus and hardness from a set of DMA tests at different indentation depth through the composite soft layer-substrate structure were assessed in view of a detailed finite element simulation for the single-layer structure to deconvolute the ratio of film elastic modulus to substrate modulus. It was found that, for pure copper treated with ammonium hydroxide solution, the yield strength of the film is about 50% of the substrate yield strength, and the film modulus is about 20% of the substrate modulus. The film thickness was found to be on the order of few nanometers, and increases with the exposure time.

For the mechanism of mechanical abrasion accelerating chemical dissolution, the wear

depth and surface topography evolution were investigated. We made use of the established fact of stress-enhanced chemical dissolution, wherein a flat surface of a stressed solid is configurationally unstable under chemical dissolution. The roughness with wavelength above a critical value grows while roughness of lower wavelength decays during dissolution. Here, a nano-wear experiment was performed to induce the local variation of the residual stress level, followed by chemical dissolution to investigate the variation of the wear depth and the evolution of surface topography due to dissolution. It is found that the residual stress caused by the mechanical wear enhances the chemical dissolution rate, as manifested by an increase in wear depth. The wavelength selectivity for stressed solid under etching could be beneficial to achieve a global and local smooth surface, since the mechanical polishing helps smooth the long wavelength and the chemical etching helps smooth the short wavelength.

The developed understanding from these experiments can be used in future studies to control the relative rates of CDR and MAR as well as investigating the various process-induced defects, like dishing, erosion, scratches, corrosion. The results can also be used to optimize process parameters, including: (i) particle shape, size and concentration; (ii) adapting slurry chemistry for required rates of chemical dissolution and mechanical abrasion; and (iii) selecting pads with the proper surface morphology and stiffness.

Chapter 1 Introduction

The shrinking dimension of integrated circuits (ICs) has led to faster devices, however, signal propagation through interconnects between devices is slower compared to traditional scaling laws (Moore's law). For ICs with gate lengths above 0.5 μm, circuit delay is primarily device delay, however for gate lengths below 0.5 μm, the interconnect delay becomes important since the device delay is also very small (Pai and Ting, 1989). For example, at 0.5 μm dimensions, the interconnect delay accounts for 20% of the circuit delay, while at 0.25 μm dimensions, about 50% of the circuit delay comes from the interconnect delay. In order to reduce the circuit delay, the interconnect delay should be reduced as the dimension becomes smaller and smaller. The widely used measure of interconnect delay is the RC time delay, in which R is the resistance of the metal line and C is the capacitance of the interlevel dielectric (ILD).

Copper has nearly 40% lower resistivity than aluminum and about 100% lower resistivity than aluminum alloy, which were formerly used as interconnect (Lide et al, 2003). Recently, copper also has a high melting temperature (1083°) than that of aluminum (660°), it is expected that copper has a better resistance to electromigration (Murarka, 1993). It has been shown that the mean time to failure due to electromigration for copper is approximately an order of magnitude higher than that for aluminum alloys (Kang et al 1992, Nitta et al 1993, Li et al 1993). Indeed, copper has become the interconnect material of choice in integrated circuits because of its low resistivity and high electromigration resistance compared to aluminum alloy interconnects.

CMP of copper has become an alternative of other processing techniques, such as

reactive ion etching (RIE), dry etching and wet etching. RIE of copper is not practical because of formation of fewer copper compounds at low temperatures with relatively high vapor pressures (Steinbruchel, 1995). Wet etching of copper is primarily isotropic in nature, which is not good for submicron patterning. The conventional dry etch technique are feasible at temperatures of about 200°. It is, however, difficult to find a stable masking material at such an elevated processing temperature (Steinbruchel, 1995). It has been shown recently that the patterning difficulty of copper is resolved by the dual damascene technique, combined with the CMP process.

CMP is becoming a promising technique in IC fabrication because of the following main reasons. (i) Multilevel metallization is used to increase the performance of the interconnection, since multilevel metallization can reduce the RC delay by decreasing the length of interconnection and increasing the width of interconnections. However, multilevel metallization requires a multilevel deposition process, which results in a highly uneven surface. In order to have good deposition at a higher level, the uneven surface due to the early deposition process should be planarized before the next level metal deposition. (ii) The patterning technique, especially lithography, requires that the wafer surface be planar over the whole die scale. To satisfy the depth-of-focus requirement of lithography, less than a 150nm difference in height across an entire stepper field should be attained (Murarka et al, 1993). Because of its demonstrated local and global planarization capability, CMP has become a critical fabrication step of mainstream semiconductor process in IC manufacturing. In addition, CMP is a room-temperature process and fits the process design trend of using a low processing temperature to reduce dopants diffusion into the silicon substrate.

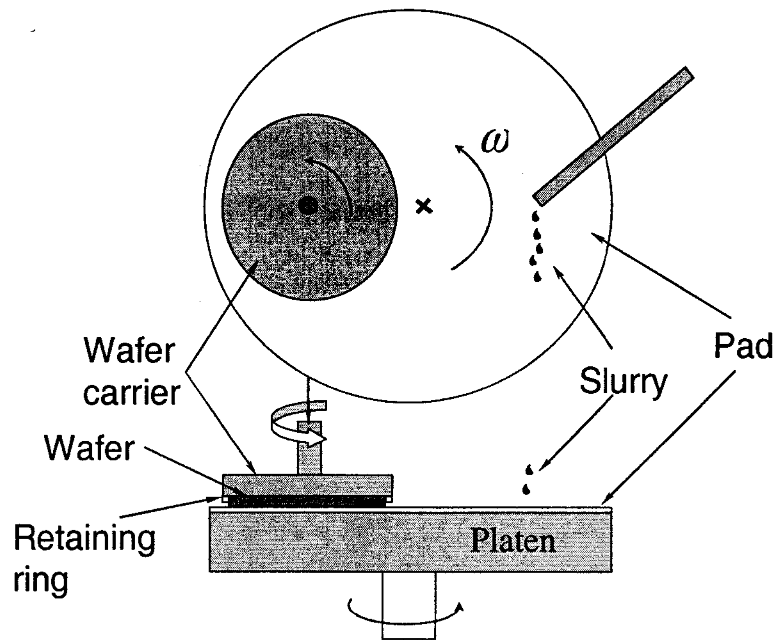

Fig 1.1 Schematic of orbital CMP tool.

CMP process employs nano abrasive particles in a chemically active slurry with a soft polishing pad to remove material from the wafer surface. A typical orbital CMP tool has a wafer carrier, a polishing pad and a slurry dispensing mechanism as depicted in Fig 1.1. The wafer is held on a rotating carrier, while the active surface being polished is pressed against a resilient polishing pad (typically porous polyurethane) attached to a rotating polish platen. Typically, a softer lower pad is used to conform to the wafer surface, while a stiffer upper pad is used to maintain the global planarization. The slurry used in the process could be either alkaline or acidic type, and usually an oxidizer is added to alkaline slurry, while corrosion inhibitor is added to acidic slurry for copper CMP. During CMP processes, if the carrier and table speeds are synchronized, the relative speed is constant across the entire wafer surface (Ouma, 1998). For typical settings, the velocity variation from center to edge is

small. However, the MRR variation from center to edge is large due to edge effect witch modifies the local pressure (Baker, 1996). The CMP process is usually used for tungsten, copper and silicon oxide; however it can also be used for other materials, such as low-k materials.

Although CMP process appears to be a very promising technique, it is usually optimized by iteration for a given wafer material and geometry. A good understanding of material removal mechanism during the CMP process would help to reduce the defect formation during the process, and can be utilized to propose some design optimization and yield improvement of the process.

1.1 CMP Polisher

There are different generations and types of CMP tools. The design improvement in CMP tools is driven by the need for high throughput and low cost of ownership. The high throughput can be achieved by either polishing multiple wafers at a given time, or increasing the material removal rate by adjusting the operational parameters, like pressure and rotational speed, or choosing appropriate abrasive particles size, concentration, slurry type and pad. Currently there are three types of polishers, linear polisher, orbital polisher, and pad feed polisher (Bibby and Holland, 2000). The main characteristics of these tools are high speed, low pressure and single polyurethane pad.

1.1.1 Linear polisher

As shown in Fig 1.2, the wafer is rotating while the active surface is faced down against a rapidly moving belt-type pad. The tension is controlled by the two rollers. The carrier usually rotates at a low speed to keep a relative uniform velocity through the wafer surface.

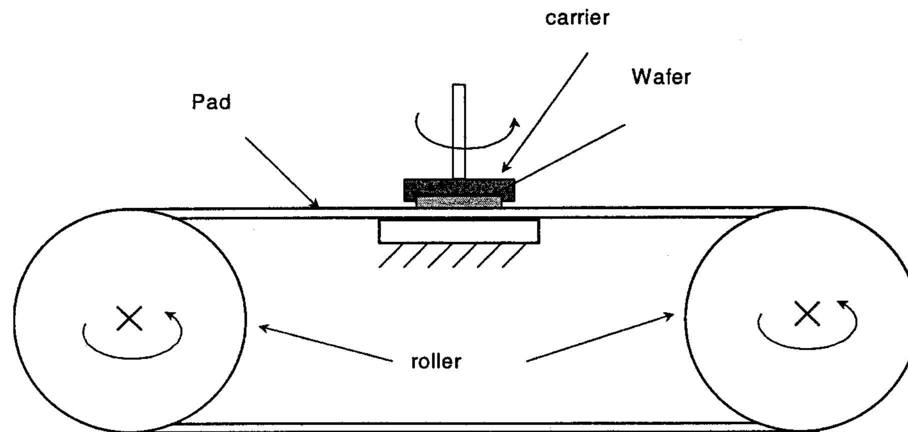

Fig 1.2 Schematic of linear polisher

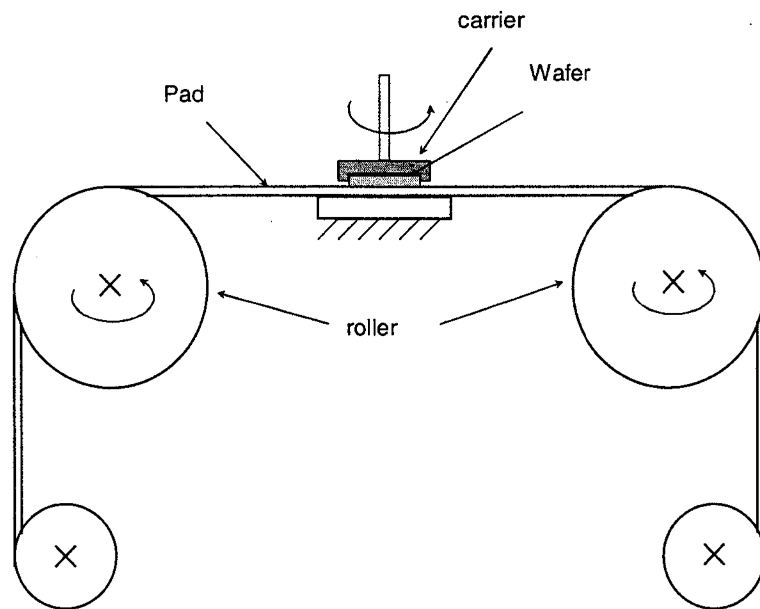

Fig 1.3 Schematic of pad feed polisher.

1.1.2 Orbital polisher

As shown in Fig 1.1, the wafer rests on a backing carrier, which is rotating about its own axis, and is pressed down against the pad, which is attached to a rotating platen disk. Its

major advantage is high relative speed with a small toll footprint. Usually the wafer and pad are rotating in the same direction.

1.1.3 Pad feed polisher

The polishing pad is roll-like as shown in Fig 1.3. The pad-roll is incrementally fed to the polishing table for simultaneous polishing of the current wafer and reconditioning for the incoming wafer. The major advantage of this system is the effective pad utilization and the low down time to change the pad.

1.2 CMP Process Variables and Their Associated Effects

The control parameters of a CMP process are the material removal rate and the quality of the polished wafer surface. However, the input parameters of a CMP process are slightly complex and difficult to control. The intrinsic parameter set includes four major groups: the abrasive particle, the slurry, the pad properties and the carrier design. These are in addition to the extrinsic control parameters of the applied down pressure and relative sliding velocity.

1.2.1 Abrasive particles

Abrasive particles are the cutting tools like the abrasives on the grinding wheel in the surface finishing process. It is delivered to the wafer surface with the slurry by the motion of wafer and pad. The commonly used abrasives are alumina, Al_2O_3, silica, SiO_2 and ceria, CeO_2. To get a better polishing result, the desired distribution of particle size has a smaller standard deviation and the particle shape is uniform.

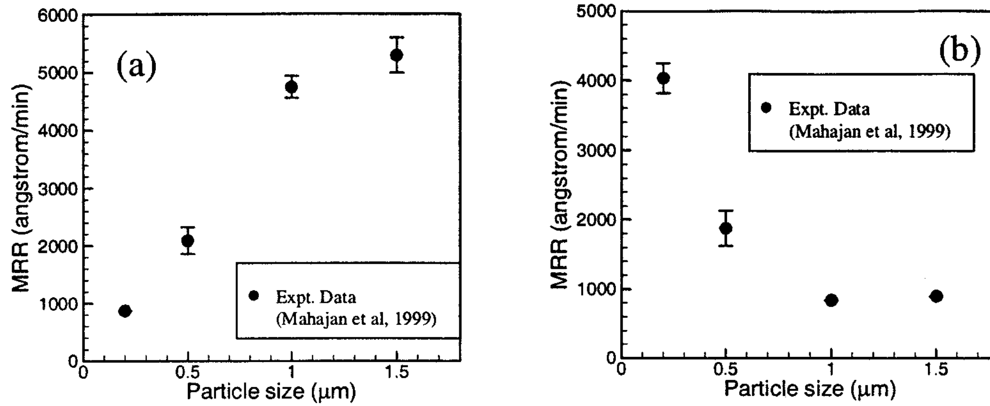

Fig 1.4 MRR variation with particle size (a) for a fixed 2wt% concentration, (b) for a fixed 10wt% concentration (SiO_2 CMP, Mahajan et al 1999).

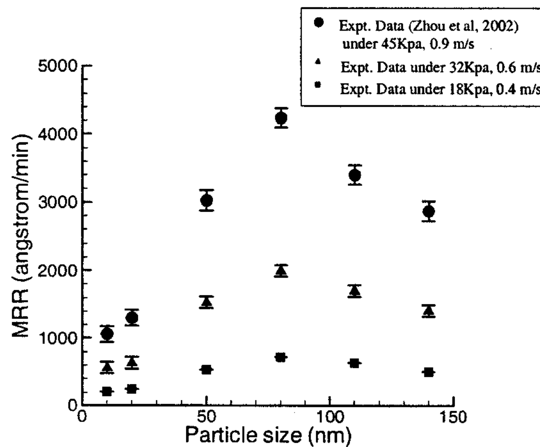

Fig 1.5 MRR variation with particle size (Zhou et al 2002).

In CMP process, the abrasive particle size is on the order of 50 to 500 nm, and the depth of cut is on the order of 1 to 10 nm. The material removal rate during CMP depends on abrasive particle through their size, concentration, hardness as well as their geometric shape. Some researchers (Jairath et al 1994, Xie et al 1996) have shown that the MRR will increase

with particle size and concentration, while others (Bielmann et al, 1999) have shown that MRR will decrease with particle size and concentration. Recently it is also observed that MRR will increase with particle size and concentration for small particle size and low concentration, and decrease with particle size and concentration for large particle size and high concentration as shown in fig 1.4 and 1.5 (Zhou et al 2002, Mahajan et al 1999).

For the sharper particles compared to the blunter particles, more material removal might be expected for the sharper one, since sharper one usually indents deeper and remove more material.

During CMP process, large particles are undesired because they will cause surface scratches. Even though the particle distribution is tightly controlled, large particles will still be present possibly due to particle agglomeration or oxide delaminations. To control the large particles, usually milling during the slurry manufacturing and filtration during the slurry distribution is commonly used (Li et al 2000).

1.2.2 Slurry

Slurry contains abrasive particles and solution with active chemical reagents. Abrasive particles provide mechanical abrasion, while chemical regents provide chemical dissolution. The major effects of the chemical reagents can be summarized as

(a) Soften the surface for easy abrasion by forming a soft surface layer.

(b) Dissolve the surface material by etching.

(c) Prevent recessed area from chemical exposure by forming a passivation layer.

(d) Prevent redeposition of detached material by increasing solubility.

(e) Provide polishing selectivity between two or more materials.

(f) Reduce agglomeration of abrasive particles and adhesion of particles to the polished surface.

For copper CMP, it is suggested that the successful slurry formulation will include chemicals to increase the solubility of the copper in the slurry and prevent the dissolution of copper in the recessed area (Steigerwald et al 1995, Carpio et al 1995). Two types of slurry are tested in their work. One is a complexing agent (increase solubility) plus an oxidizer (increase dissolution rate), such as NH_4OH plus ferricyanide; the other is oxidizing acid plus corrosion inhibitor, such as HNO_3 plus benzotriazole (BTA). By balancing the mechanical abrasion rate to the chemical dissolution rate of detached species, a good planarization will be achieved. The alkaline slurry, NH_4OH plus another oxidizer $NaClO_3$, is tested by Luo et al (1997). It is shown in their study that MRR is increased significantly by adding the oxidizer to the slurry compared to the slurry without the oxidizer. The corrosion inhibitor BTA is also tested with alkaline slurry NH_4OH, it is shown that the dissolution rate drops significantly, while the polishing rate is not affected.

The Pourbaix (1966) diagram, shown in Fig 1.6, indicates that alkaline slurry with high PH value facilitates formation of a passivation layer on the surface, thus an oxidizer is usually added to increase the dissolution rate. In acidic solutions with low PH value, copper ions are stable, thus a corrosion inhibitor is added to form a passivation layer to prevent the recessed area from chemical exposure. Another type of slurry, hydrogen peroxide plus glycine is studied by Seal et al (2002), in which hydrogen peroxide is an oxidizer and glycine is a complexing agent for copper.

For tungsten CMP, it is suggested that a passivation layer WO_3 forms naturally in the slurry solution, followed by the mechanical abrasion of this layer (Kaufman et al, 1991). A

bare tungsten surface is not thermodynamically stable, so WO_3 forms very quickly in the slurry, and prevents the further oxidization and dissolution of tungsten in the slurry. Accordingly, a repetitive process of surface layer formation and removal cause planarization of the tungsten.

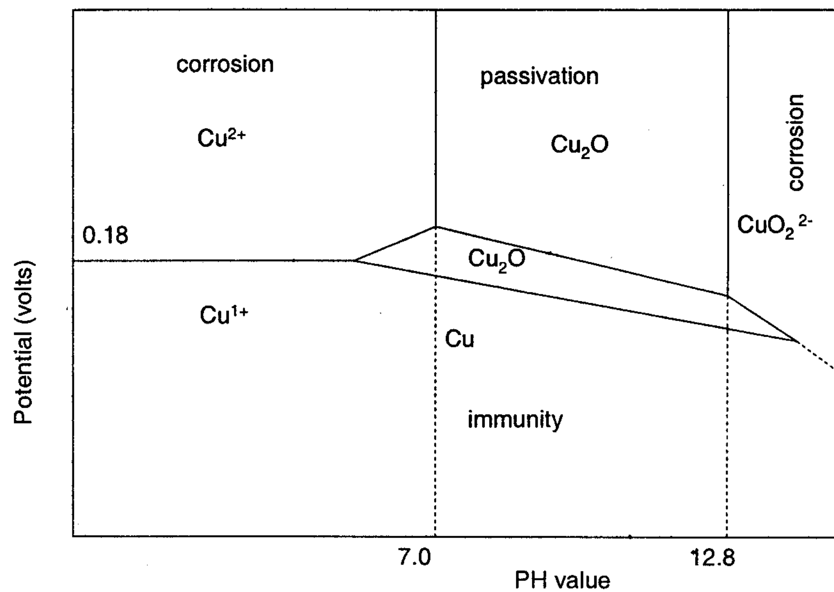

Fig 1.6 Schematic of Poubaix diagram for the Cu-H2O system

For silicon oxide CMP, a hydroxilated layer will be formed according to the reaction $\{SiO_2 + 2H_2O \leftrightarrow Si(OH)_4\}$. The original strong Si-O bond is broken, and a weak Si-OH bond forms, facilitating the formation of a soft layer for mechanical abrasions. In oxide CMP, common solutions are KOH based or NH_4OH based with high PH value. Silicon dioxide is partially dissolved so that the hydration is further enhanced. It is also suggested that high PH solutions will decrease particle agglomeration and reduce CMP scratches (Li et al, 2000).

1.2.3 Pad

The pad is a polymer material (usually polyurethane). The mechanically effective stiffness of the pad is affected by the details of its microstructure and its surface roughness. The pad properties which influencing the quality of CMP process are:

(a) The base Young's modulus and Poisson's ratio for the dense polymers and the effective one's for the porous pad structures.

(b) The effective hardness and compressibility of the pad.

(c) The viscoelastic characteristics of the pad.

(d) The surface topography of the pad.

During the CMP process, the slurry is transferred to the wafer surface by pad. Also, the pad aids the abrasive plowing action, as well as removes the abraded material from the wafer-pad contact area. To realize these goals, the pad is either perforated or grooved to facilitate a better transportation of slurry.

The pad surface topography determines the force partition between active slurry and direct pad-wafer contact. At high asperities of the pad surface, the pressure is higher, while at recessed area of the surface cell pores, there is little or no pressure. Accordingly, the pressure distribution across the wafer surface depends on the stiffness of the pad, as well as the density and spatial distribution of the elevated features on the pad.

The viscoelastic behavior of the pad plays an important role in the planarization process. As the pad passes from high features to low features of the wafer surface, it cannot conform to the low features instantly because of its viscous behavior. Thus, less pressure is applied on the lower features, which leads to low MRR. As the pad passes from low features to high features, it also cannot conform to the high feature immediately. Thus, high pressure is

applied on the high features, which leads to high MRR. From this point, viscoelasticty of the pad should aid in the planarization of the wafer surface.

During CMP of metal, overpolishing is required to remove all metallic residues on dielectric surface. In general, metal is polished faster than oxide due to variation of the contact stiffness, resulting in dishing of the metal lines. Dishing is not desirable if a step height between metal line and dielectric is too high. During overpolishing, the oxide layer at the edges close to a metal line is also slightly polished. This is called erosion. The dishing and erosion are two major defects in metal CMP, which cause difficulty of next level metallization.

Different pads have been developed to meet the current CMP requirement. Some pads are designed for high MRR, while others are designated for the final surface finish. Cook (2000) classified pads into four kinds according to their structure.

(a) Felts and polymer impregnated felts (Suba IV) --- The microstructure is continuous channels between felted fibers with a polymer binder. It is mainly used for Si stock polishing and tungsten damascene CMP.

(b) Microporous synthetic leathers --- The microstructure is complex foam with vertically oriented channels. There is a high porosity film on the substrate. It is mainly used for Si final polishing and metal damascene CMP.

(c) Filled polymer films (IC1000) --- The microstructure is closed cell and open cell foam. It is a solid urethane sheet with filler such as voids, silicon dioxide. It is mainly used for ILD CMP and metal damascene CMP.

(d) Unfilled textured polymer films --- This is solid polymer sheet with certain surface texture and is mainly used for ILD CMP.

During the CMP process, pad wear will occur. The result is that the slurry transportation is impeded. The abraded material cannot be removed from the system, so the pad has to be treated to have repeatable and consistent results.

1.2.4 Carriers

Carrier is one of the important components in CMP tool design and its functions are (Bibby and Holland, 2000):

(a) To load and unload the wafer.

(b) To keep the wafer in kinematical motion.

(c) To compensate for small amount of wafer tilt, bow or warp by using carrier film.

(d) To reduce the within wafer nonuniformity (WIWNU).

One of the biggest concerns in carrier design is WIWNU. The goal is to achieve the uniform pressure throughout the wafer-pad surface.

1.3 Common CMP Defects

The defects detection and reduction are among the important issues in CMP process, since the CMP defects are the yield killers. There are several copper related defects that affect yields of the overall manufacturing process, and they are described below.

1.3.1 Metallic residuals and associated dishing and erosion

Metallic residuals are frequently noted in the IC manufacturing industry as "yield killers", since it can damage the devices by the electrical short circuits. Because of the different material removal rate within each wafer and within each die in the wafer, there are within-wafer-non-uniformity and within-die-non-uniformity of CMP which will cause non-planarity of the next layer, inducing copper residuals to exist over the dielectric on the wafer

surface. A certain amount of overpolishing is needed to remove all metallic residues on dielectric surface to ensure the isolation between adjacent circuits. However, dishing and erosion may occur during the step of overpolishing, causing an undesired line thinning.

1.3.2 Surface defects and scratches

Copper is very soft compared to tungsten and silicon oxide, so it is easier to be scratched during the CMP process. Common scratches in copper CMP may be classified as, razor scratches, chatter scratches and skipping scratches as shown in Fig 1.7 (Guha et al (2001)). While the reason of each of these scratches is not well understood, it is speculated that they are related to intergranular failure along the scratch path (Stechenrider et al 2001).

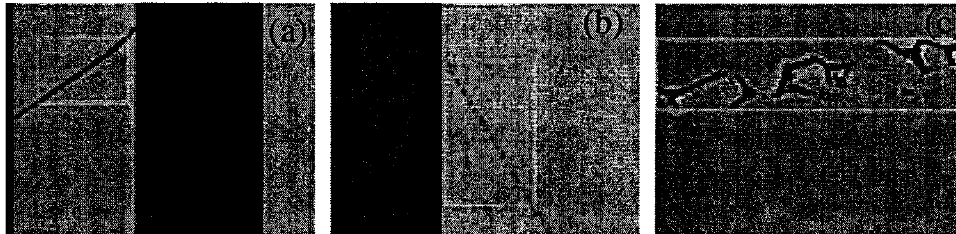

Fig 1.7 Copper scratch examples: (a) razor scratch, (b0 chatter scratch, and (c) skipping scratch.

1.3.3 Pin-holes and microcracks

Electroplated copper is a polycrystalline material. The grain boundaries and triple-point junctions are mechanically and chemically vulnerable. Shear stresses generated during the CMP process can lead to material fracturing (inter-grain cracking) and stress induced chemical attacks (inter-grain corrosion). A microcrack can also trap chemicals due to capillary forces, and the crack will continue to propagate along the grain boundary. In

addition to intergranular cracks created under stress and corrosion, pin-holes in the film are observed frequently. Pin-holes can extend deep into the film and render the chip useless. Currently, the nucleation and propagation characteristics of these pin-holes are not well understood. These defects also might occur during the regular polish phase as well as the overpolishing phase.

1.3.4 Corrosion and pitting

Line corrosion is usually due to the CMP slurry chemistry. Another mode of observed corrosion is edge corrosion, which frequently occurs at the interfaces between different materials (e.g., interface between dielectric/barrier layers and the Cu fill). Any separation of the interface generates gaps that serve as sites for corrosion and microcracking. Currently, nucleation and propagation characteristics of edge corrosion in Cu layers are poorly understood. These types of defects are dependent upon feature geometries and can occur during both phases of a CMP polish.

1.4 Existing Models for CMP Process

It is known that the material removal in CMP occurs due to the coupling between the chemical dissolution and the mechanical abrasion. Previously, the role of the chemistry and the mechanics are addressed separately. For example, the chemical effects could be accounted for by assuming that a soft layer of chemical product layer is formed, then it is mechanically abraded. Then, a mechanistic model can be constructed to understand the process.

Generally, there are two typical mechanical models in the CMP process, either by considering the formation of a continuous film according to lubrication theory, or the

possibility of direct wafer-pad contact according to contact mechanics. In the lubrication model, it is assumed that the pressure is very low, and the fluid (or slurry) speed is very high. So there is a fluid layer between the wafer and the pad, so that they do not contact each other during the polishing process. The material removal is due to the fluid flow, and lubrication theory is used to formulate the shear force on the wafer surface. In this case, the mechanical effect of abrasive particles is not considered, and the resulting MRR is very low. This model could be used as a lower bound of MRR in CMP process. In the direct wafer-pad contact model, the pressure is usually very high compared to the lubrication model, and fluid speed is low. A three-body contact of the wafer, abrasive particles and pad exists during the polishing process. The material removal is due to repeated sliding, rolling, nano-indentation and ploughing of the abrasives against the wafer surface.

There are several MRR models for CMP process. The earliest model of CMP is from glass polishing technology, and it is derived by Preston (1927). Preston's equation represents a wafer scale phenomenological model, where all the physical and chemical effects are lumped into the Preston's coefficient. Although such an equation has been widely used in CMP process, it cannot show the effect of the various process parameters on the MRR. Recent experiment results have shown that pad properties as well as abrasive particles size and concentration have significant effects on the MRR variation. Further development of the modeling framework is needed to address the various aspects and process parameters of the CMP process.

Among the various models available for the MRR during CMP process, Brown (1981) has developed a mechanistic model for optical polishing of metals. They assumed full solid-solid contact, and developed a governing equation similar to the Preston's equation with

Preston's coefficient to be $1/(2E)$. Tseng and Wang (1997) proposed a modification to the assumption of linearity in Preston's equation. They derive a feature scale model with ($MRR \sim P_0^{5/6} \cdot u^{1/2}$) based on combined solid and fluid interactions. Here, P_0 is the applied nominal pressure, u is the relative sliding velocity. Their model predictions fit plausibly with the experimental results of thermal oxides CMP. Based on fluid mechanics, a 40 to 65 microns slurry film thickness was assumed in their formulation.

Bulsara et al (1997) have developed a mechanistic model to determine the number of the abrasive particles involved in material removal, referred as active particles, and the normal force acting on a single active abrasive. They stated that the forces are only transferred from the pad to the wafer by the active particles, and then the average force per particle could be derived. This model is applicable for hard pads, low applied pressures and high abrasives concentration. An interesting result was that the active particles were at the tail end of the particle size distribution (less than 0.5% of the total abrasive particles). These authors suggested that the abrasive particles with peaked size distribution should be used in the CMP polishing process.

Shi and Zhao (1998) developed a model for CMP process with soft pads. They also predict a nonlinear pressure dependence of MRR with ($MRR \sim P_0^{2/3} \cdot u$). It was shown that the fundamental mechanism of the pressure dependence of MRR with a soft pad was totally different from that with a hard pad. Recently Zhao and Shi (2000) develop a new model with ($MRR \sim \left(P_0^{2/3} - P_{th}^{2/3}\right) \cdot u$). In this model, a threshold pressure was introduced, and only the pressure over this limit would cause material removal. Some experimental data fitted well with this equation, but no better physical explanation supported this threshold pressure. Also

the fitting parameter involved in their equation was not dimensionless, which suggested that some other process parameters were required to be accounted.

Luo and Dornfeld (2001) developed a particle scale model based on fully plastic contact among the wafer, abrasive particles and pad. They proposed a new model with ($MRR = C \cdot P_0^{1/2} \cdot u$). It is worth noting that the constant C is not only related to the material properties, but also a function of pressure. This relation is derived by introducing a particle size distribution that depends on the applied pressure, and assuming a very hard pad, which may be in conflict with the soft pad assumption. Although there were some ambiguities, this was a new MRR model that gave insights to the role of material property and surface roughness of the pad, as well as the abrasives shape and size distribution.

Fu et al (2001) had developed a proposed plasticity based model for the material detachement from the wafer, while modeling the cell level interaction of the pad as beams to determine the relationship between the MRR and the process parameters, such as pressure, velocity, pad property, abrasive shape, abrasive size and abrasive concentration. The model suggests two different contact modes between the wafer, abrasive particles and pad. A non-contact mode for which the applied down pressure is transferred only by abrasive particles from the wafer to the pad) and ($MRR \sim P^{3/2} V$). The other mode is direct pad-wafer contact, wherein the applied down pressure is shared between the active abrasive particles and the direct pad-wafer contact, and ($MRR \sim P^{9/8} V$). An analytical solution for this transition condition is established. The model prediction matches well with a set of experimental data by comparing the MRR trend with the applied pressure, velocity, particle size and concentration.

Bastawros et al (2002) developed a phenomenological model based on numerical simulation of the pad-particle-wafer interactions, while accounting for pad porosity and surface morphology. The model indicated the existence of three domains of interactions among the pad, abrasive particles and the polished wafer. These are no contact between the pad and the wafer, partial contact and full contact; based on the level of the applied pressure, pad modulus and particles concentration. The predicted MRR relations with slurry characteristics were in agreement with the experiment trends.

1.5 Objective

The intent of this work is to understand the fundamental material removal mechanism for the Cu CMP process by investigating the synergy between chemical dissolution and mechanical abrasion during the CMP process.

The developed understanding can be used in future studies to investigate the various process-induced defects, like dishing, erosion, scratches, corrosion. The results can also be used to optimize the process parameters, including (i) particle shape, size and concentration, (ii) adapting slurry chemistry for required rates of chemical dissolution and mechanical abrasions and (iii) selecting pads with the proper surface morphology and stiffness.

To understand the material removal mechanism, first the mechanical detachment of material from the surface at the nano-scale is experimentally investigated. The experimental results are used to devise a phenomenological model for the MRR. Then the synergistic effects of chemical dissolution and mechanical abrasion are investigated from two aspects; (i) chemical enhanced mechanical abrasion and (ii) mechanical abrasion affected chemical dissolution. The interactions between mechanical abrasion and chemical dissolution are

believed to be the key factors influencing the MRR and quality of the surface.

Chemical enhanced mechanical abrasion arises from forming a soft surface layer due to chemical reaction. This soft layer has different material properties and surface topography relative to the original surface. It is easier to be detached compared to the base reference surface, which leads to an increased MRR. This phenomenon will be addressed experimentally, and then modeled using FEM. The experimental protocol utilizes nano-scratch and nano-DMA test to show the difference in surface layer response between dry (surface without chemical exposure) and wet (with chemical exposure) conditions. The modeling technique uses the analytical model for travel indenter and FEM model.

Mechanical abrasion affected chemical dissolution is investigated by nano-wear experiments. It is anticipated that the residual stress enhances chemical dissolution. Accordingly, two sets of nano-wear experiments are performed, mechanical wear followed by chemical dissolution and chemical exposure followed by mechanical wear. It is expected that the wear depth should be increased in each individual wet test compare to the dry test. The topography evolutions during the process are investigated to find the quality of the surface during the process.

1.6 Thesis Outline

The thesis is laid in five chapters. Chapter 1 is the introduction of CMP process, process parameters and typical CMP equipments. Different MRR models are reviewed in this chapter. Chapter 2 describes a phenomenological MRR model based on scratch intersection. Chapter 3 shows the chemical enhanced mechanical abrasion by soft layer formation. The experimental and modeling technique is elaborated upon. Chapter 4 shows the mechanically

assisted chemical dissolution. The nano-wear experiment and modeling technique are elaborated upon. The concluding remarks and prospective future work are given in Chapter 5.

1.7 References

1. Baker, A.R., The origin of edge effect in chemical mechanical planarization, Proceedings of Electro. Chem. Soc. Meeting, Vol. 96, No. 22, pp 228, 1996.

1. Bastawros, A.-F., Chandra, A., Guo, Y., and Yan, B., Pad effects on material removal rate in chemical mechanical planarization, Journal of Electronic Materials, Vol. 31, No. 10 SPEC., pp 1022-1031, October 2002.

2. Bibby, T. and Holland, "equipment", Semiconductors and Semimetals, San Diego, CA, USA, Academic Press, Vol. 63, pp 5-46, 2000.

3. Bielmann, M., Mahajan, U. and Singh, R.K, Effect of particle size during tungsten chemical mechanical polishing, Electrochemical and Solid-State Letters, Vol. 2, No. 8, pp 401-403, Aug 1999.

4. Brown, N.J., Baker, P.C. and Maney, R. T, Optical polishing of metals, Proc. of SPIE, Vol. 306, pp 42-57, 1981.

5. Bulsara, V.H., Ahn, Y., Chandrasekar, S. and Farris, T.N., Mechanics of polishing, Manufacturing Science and technology, ASME, Vol. 1, pp 225-233, 1997.

6. Carpio, R., Farkas, J. and Jairath, R., Initial study on copper CMP slurry chemistries, Thin Solid Films, Vol. 266, No. 2, pp 238-244, Oct 1995.

7. Cook, L.M., CMP Consumables II: Pad, Semiconductors and Semimetals, San Diego, CA, USA, Academic Press, Vol. 63, pp 5-46, 2000.

8. Fu, G., Chandra, A., Guha, S. and Subhash, G., A plasticity based model of material

removal in chemical mechanical Polishing (CMP), IEEE Trans. Semiconductor. MFG., Vol. 14, No. 4, pp 406-417, 2001.

9. Guha, S., Sethuraman, A., Gotkis, Y., Kistler, R. and Steckenrider, S., Navigating yield through the maze of copper CMP defects, Solid State Technology, Vol. 44, No. 4, pp 63-64+67-68+70, April 2001.

9. Jairath, R., Desai, M. and Tolles, R., Consumables for the chemical mechanical polishing (CMP) of dielectrics and conductors, Materials Research Society Symposium - Proceedings, Advanced Metallization for Devices and Circuits - Science, Technology and Manufacturability, Vol. 337, pp 121-131, 1994.

10. Kang, H.K., Cho, J.S. and. Wong, S.S, Electromigration properties of electroless plated Cu metallization, IEEE Electron Device Letters, Vol. 13, No. 9, pp 448-450, 1992.

11. Kaufman, F.B., Thompson, D.B., Broadie, R.E., Guthrie, W.L., Pearson, D.J. and Small, M.B., Chemical-mechanical polishing for fabricating patterned W metal features as chip interconnects, Journal of the Electrochemical Society, Vol. 138, No. 11, pp 3460-3465, Nov 1991.

12. Li, J., Blewer, R. and Mayer, J.W., Copper Metallization, Mater. Res. Soc. Bull, XVIII, pp 18-56, 1993.

13. Li, S.H. and Miller, R.O., Semiconductors and Semimetals, San Diego, CA, USA, Academic Press, Vol. 63, pp 5-46, 2000.

14. Lide, D.R., CRC Handbook of Chemistry and Physics, Boca Raton, FL, CRC Press, 79th, 1998-1999.

15. Luo, J. and Dornfeld, D.A., Material removal mechanism in chemical mechanical polishing: theory and modeling, IEEE Trans. Semiconductor. MFG., Vol. 14, No. 2, pp

112-133, 2001.

16. Luo, W., Campbell, D.R. and Babu, S.V., Chemical-mechanical polishing of copper in alkaline media, Thin Solid Films, Vol. 311, No. 1-2, pp 177-182, Dec 1997.

17. Mahajan, U., Bielmann, M. and Singh, R.K., Abrasive effects in oxide chemical mechanical polishing, Materials Research Society Symposium Proceedings: Chemical Mechanical Polishing – Fundamentals and Challenges, Vol. 566, pp 27-32, 1999.

18. Murarka, S.P., Metallization, Butterworth-Heinemann, Boston, pp 100, 1993.

19. Murarka, S.P., Steigerwald, J.M. and Gutmann, R.J., Inlaid copper multilevel interconnections using planarization by chemical-mechanical polishing, MRS Bulletin, Vol. 18, No. 6, pp 46, Jun 1993.

20. Nitta, T., Ohmi, T., Hoshi, T., Sakai, S., Sakaibara, K., Imai, S. and Shibata, T., Evaluating the large electromigration resistance of copper interconnects employing a newly developed accelerated life-test method, Journal of the Electrochemical Society, Vol. 140, No. 4, pp 1131-1137, Apr 1993.

21. Pai, P.L. and Ting, C.H., Selective electroless copper for VLSI interconnection, IEEE Electron Device Letters, Vol. 10, No. 9, pp 423-425, Sep 1989.

22. Preston, F.W., The theory and design of plate glass polishing machine, J. Soc. Glass Tech., Vol. 11, No. 44, pp 214-256, 1927.

23. Pourbaix, M., Atlas of Electrochemical Equilibria in Aqueous Solutions, Pergamon, Oxford, 1966.

24. Seal, S., Suiry, S.C., Heinmen, B., Effect of glycine and hydrogen peroxide on chemical-mechanical planarization of copper, Thin Solid Films, Vol. 423, No. 2, pp 243-251, Jan 2003.

25. Shi, E.G. and Zhao, B., Modeling of chemical-mechanical polishing with soft pads, Appl. Phys. A, Vol. 67, pp 249-252, 1998.

26. Stechenrider, J.S., Guha, S., Sethuraman, A., Ra, Y. and Kim, H., Classifying defects for copper CMP process modules, MICRO, Vol. 19, No. 8, pp 33-45, September 2001.

27. Steigerwald, J.M., Murarka, S.P., Gutmann, R.J, and Duquette, D.J., Chemical processes in the chemical mechanical polishing of copper, Materials Chemistry and Physics, Vol. 41, No. 3, pp 217, Aug 1995.

28. Steinbruchel, Ch., Patterning of copper for multilevel metallization: reactive ion etching and chemical-mechanical polishing, Applied Surface Science, Vol. 91, No. 1-4, pp 139-146, Oct 1995.

29. Tseng, W.T. and Wang, Y.L., Re-examination of pressure and speed dependences of removal rate during chemical-mechanical polishing processes, J. Electrochem. Soc., Vol. 144, No 2, pp L15-L17, 1997.

30. Xie, Y. and Bhushan, B., Effects of particle size, polishing pad and contact pressure in free abrasive polishing, Wear, Vol. 200, No. 1-2, pp 281-295, Dec 1996.

31. Zhao, B., and Shi, F. G., Chemical mechanical polishing in IC processes: new fundamental insights, Int. J. CMP, Vol. 1, No. 1, pp 13-25, 2000.

32. Zhou, C., Shan, L., Hight, R., Danyluk, S., Ng, S. H. and Paszkowski, A. J., Influence of colloidal abrasive size on material removal rate and surface finish in SiO_2 chemical mechanical polishing, Lubrication Eng., pp 35-41, August 2002.

Chapter 2 A Scratch Intersection Model of Material Removal during Chemical Mechanical Planarization (CMP)

2.1 Abstract

A scratch-intersection-based material removal mechanism for CMP processes is proposed in this paper. The experimentally observed deformation pattern by SEM and the trends of the measured force profiles (Che et al, 2003) reveal that, for an isolated shallow scratch, the material is mainly plowed sideway along the track of the abrasive particle with no net material removal. However, it is observed that material is detached close to the intersection zone of two scratches. Motivated by this observation, it is speculated that the deformation mechanism changes from ploughing mode to shear-segmentation mode as the abrasive particle approaches the intersection of two scratches under small indentation depth for ductile metals.

The proposed mechanistic material removal rate (MRR) model yields the Preston constant similar to those observed experimentally for CMP processes. The proposed model also reveals that the nature of the slurry – pad interaction mechanism, and its associated force partitioning mechanism, which is important for determining the variation of MRR with particle size and concentration. It is observed that under relatively soft pads, small particles and low particle concentration, the pad undergoes local deformation, yielding an increased MRR with increasing particle size and concentration. At the other extreme, the intact walls of the surface cells and the connecting cell walls between the surface pores deforms globally, resembling a beam or a plate, and a decreasing trend in MRR is observed with increasing

particle size and concentration. The predicted MRR trends are compared to existing experimental observations.

2.2 Introduction

Precision finishing and planarization are becoming integral process steps in multilevel metallization designs for integrated circuit (IC) manufacturing. This is needed to ensure local and global surface planarization before the next layer is deposited. The surface finishing process (industrially known as Chemical-Mechanical Polishing, CMP) employs micro and nano abrasive particles in a chemically active slurry with a soft polishing pad to remove material from the surface. In common CMP processes, material removal is accomplished by pressing a wafer into a relatively soft porous pad flooded with an abrasive slurry, while both the pad and the wafer have a relative orbital motion (Fig. 1.1). The wafer rests on a backing plate, which is rotating about its own axis, and is pressed down against the pad, which is attached to a rotating platen disk. An abrasive slurry with various process specific chemical compounds is typically used in a CMP process. The chemical aspects of the process are thought to be softening and/or dissolving the top layer of the surface while mechanically removing it. Such interaction facilitates usage of soft abrasives in CMP.

This work focuses on understanding the mechanical aspects of the surface material detachment mechanisms during the CMP process. The experimentally observed deformation patterns and force profiles from the micro-scale scratch experiments (Che et al, 2003) are used to provide a plausible mechanism for material detachment through a combination of surface plowing and shearing under the abrasive particles. The gained insights are integrated into mechanism-based models for the material removal rate (MRR).

The process of mechanical surface polishing is usually envisioned through the phenomenological Preston formula (Preston 1927); wherein the height reduction rate, is given by:

$$\frac{dh}{dt} = K \cdot P_0 \cdot u \tag{1a}$$

and the corresponding volumetric material removal rate (MRR) is given by:

$$MRR = A_w \cdot \frac{dh}{dt}. \tag{1b}$$

Here, P_0 is the applied nominal pressure, u is the relative sliding velocity, A_w is the wafer surface area, and K is the Preston proportionality constant (encompassing the chemical effects). All the unforeseen process parameters are lumped into the proportionality constant. Detailed analysis (Luo and Dornfeld 2001, Fu et al 2001, Bastawros et al 2002, Seok et al 2003) have shown that the pressure dependence is non-linear with an exponent that ranges from 0.33 to 1.5 based on the details of the models. These models use a proportionality constant similar to the Preston constant to scale the magnitude of model predictions to experimental measurements. Currently, no complete physical basis is attached to the Preston constant. The framework of these polishing models assumes that each active particle under the applied load generates a continuous trench, and the material removed is equivalent to the volume of the generated trench. Such a framework is applicable at the macro-scale and is in agreement with the conventional card model used in metal cutting and coarse grinding operations (e.g. Shaw 1984).

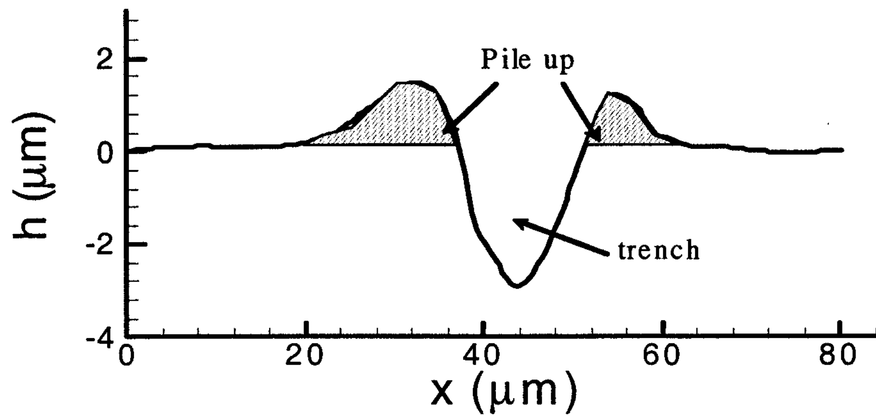

Fig 2.1 An AFM scan of a representative scratch cross-section during single grit scratching of Copper (depth of cut 3 μm). The volume in the trench is about the same as the pile-up volume.

However, for oblique cutting with high negative rake angle, it has been observed by Che et al (2003) that the local deformation and the nano-scale material removal mechanisms for ductile materials (e.g., copper) are quite different from what is commonly observed in macro-scale processes. At these very small "depth of cut", the abrasive particle forms a continuous trench, but the material is not detached from its parent surface. It merely flows from the bottom of the trench to the side via stable plastic deformation and form "pile up". Such deformation pattern has been observed (as shown in Fig. 2.1 from an AFM scan) in micro-scale scratching of copper (Che 2002, Che et al 2003), nano-scale AFM indentation and scratch tests (Kuehn 2000), and is akin to profile rolling of gears (Lange and Kurz 1984, Chandra 1989). It is further hypothesized that detachment occurs later as a result of plastic instability due to interaction of scratches. This interaction may be in the form of intersection of two scratches or may be due to the vicinity of two parallel scratch-tracks (Xie et el, 1993). It can also result from metal fatigue due to repeated plastic deformation in the pile-up region

beside the trenches produced by the abrasive particles. Che et al (2003) have investigated only a particular form of this interaction (orthogonal intersection) and established a "*characteristic detachment ratio*" (CDR), which is ratio of the detached material segment at an intersection relative to the depth of cut. In their model formulation, Che et al (2003) assume that the cross section is dictated by the indenter or abrasive particle profile. However, no experimental study investigating the relationship of scratch characteristics (e.g., aspect ratio) to the width of the detached flake has been carried out.

The present paper extends this concept of scratch intersection by employing the characteristic detachment ratio to develop a phenomenological MRR model during the CMP process of annealed copper. The model development steps are given in section 2. The model predictions showing the various domains of MRR are given in Section 2g. Section 3 provides comparison of the model prediction with documented experimental measurements. The discussion and concluding remarks follow in Section 4. Throughout the paper, the subscript "*p*" stands for pad, "*w*" for wafer, "*a*" for asperity and "c" for the abrasive cutting particles.

2.3 Material Removal Model Development

To predict the MRR for a CMP process, the transfer of the applied pressure to individual abrasive particle has to be characterized. Following the approach of Luo and Dornfeld (2001) and Bastawros et al 2002, a flow chart for analyzing the MRR in a CMP process is schematically shown in Fig. 2.2. Each step is elaborated in the following sections.

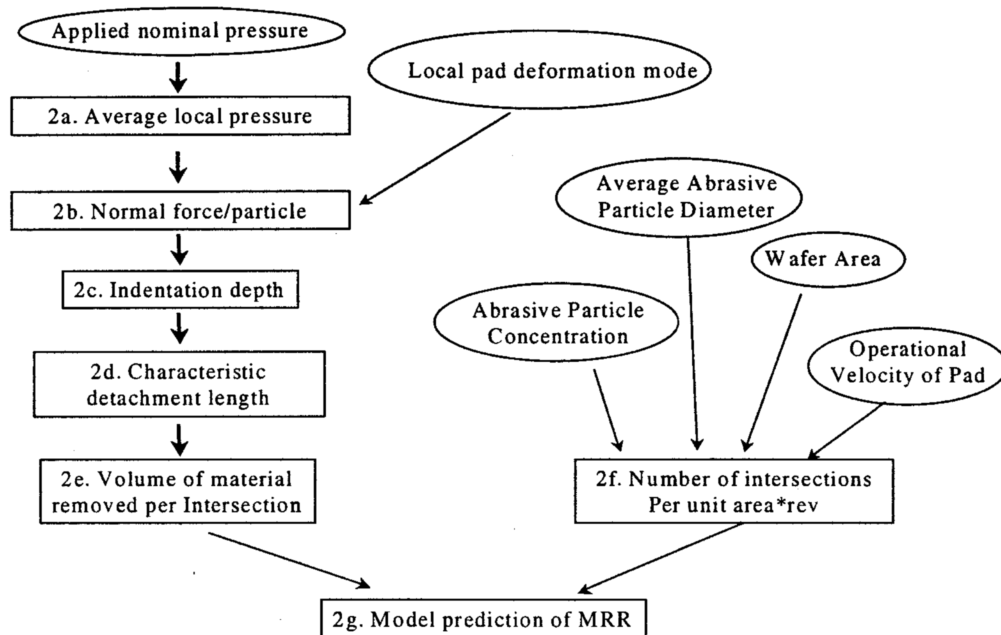

Fig 2.2 Flow chart for calculating the MRR in a typical CMP process.

2.3.1 Determination of the average local pressure per asperity

Generally there are four classifications of pad response ranging from soft to hard according to their surface properties (Cook, 2000). Hard pad is ideal for global planarization and reduction of the dishing problem, but it may cause some surface defects like scratches. Soft pad is good for reducing surface defects, but prone to the dishing problem. Accordingly, there is a trade off in selecting the pad for a Cu-CMP process. The topography structure of a frequently used IC1000 (relatively soft pad) is shown in Fig. 2.3, (Bastawros et al 2002). The average pore diameter is about $50\mu m$, and the pad surface density is about 35%. The analysis of pad surface roughness has shown the existence of multiple wave length roughness. A long wavelength is observed with length scale about 15 to 20 times the pore diameter, with

amplitude about 0.1 to 0.2 times the pore diameter. Within this long wavelength, there are clusters of pad asperities of about 2-4 times the cell diameters. The short wavelength of the local cell surface roughness is about $1-2\mu m$. Accordingly, the applied nominal pressure is supported by the high regions (or asperities) of the pad, which is in contact with the wafer surface. Since the typical abrasive particle diameter is of the order of 100 nm, only those particles residing on the high regions of the pad are active in cutting the wafer surface material. Therefore the local contact pressure between the pad asperities and the wafer surface has to be estimated.

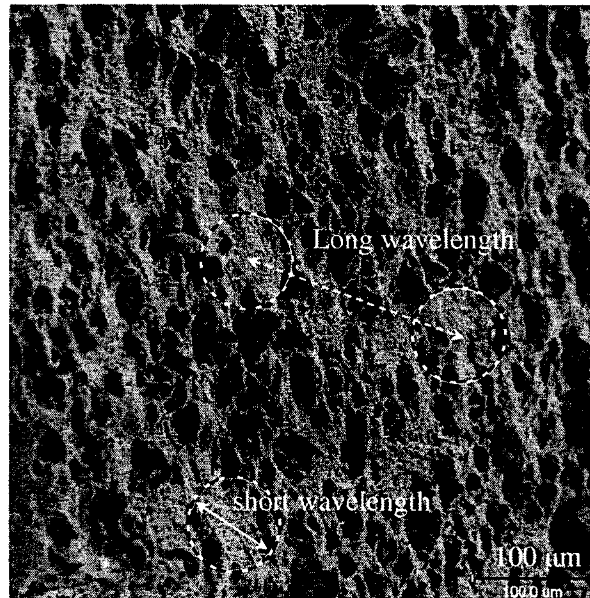

Fig 2.3 SEM image of an IC1000 pad. The pad surface is tilted 60° of the viewing axis to show the relative surface topography. The average pore diameter is about $d_p = 50\mu m$.

A simple model is developed to describe this relationship based on the force equilibrium. Following the approach of Luo and Dornfeld (2001), Bastawros et al (2002) and Seok et al

(2003), a periodic roughness with number of asperities per unit area, ρ_a, over the pad surface is assumed. ρ_a is a characteristic of the pad surface topography. As a first approximation, we will consider that ρ_a does not evolve with pad deformation and wear. Accordingly, the normal force per asperity will be:

$$F_a = \frac{P_0}{\rho_a} \tag{2a.1}$$

The long wavelength asperities are assumed to have a radius of curvature R_a. The evolution of the contact area between the asperity and the wafer surface is represented by Hertzian elastic contact. In this model the asperity is assumed to be deformable while the wafer surface is assumed to be relatively rigid. Accordingly, the contact radius a is given as a function of P_0 by

$$a = \left[\frac{3}{4}\frac{P_0}{\rho_a}\frac{R_a}{E}\right]^{1/3}, \tag{2a.2}$$

$$\frac{1}{E} \equiv \frac{1-\nu_w^{\;2}}{E_w} + \frac{1-\nu_p^{\;2}}{E_p} \approx \frac{1}{\overline{E}_p}\;. \tag{2a.3}$$

Here E is the equivalent elastic modulus, E_w, E_p, ν_w and ν_p are the elastic moduli and Poisson's' ratio of the wafer and the porous pad respectively, and $\overline{E}_p = E_p / \left(1-\nu_p^{\;2}\right)$. Accordingly, each pad asperity will have a summit with an area, $A_a = \pi\, a^2$. The total wafer/pad contact area is given by the total number of asperities and the area of each asperity

$$A \equiv (\rho_a A_w) A_a = \lambda\, A_w \left(\frac{P_0}{\overline{E}_p}\right)^{2/3}$$
$$\lambda = \pi \left[\frac{3}{4} R_a \sqrt{\rho_a}\right]^{2/3} \tag{2a.4}$$

where λ is a dimensionless parameter that represents the pad surface topography. λ is about 0.6 for IC1000 pad based on Bastawros et al, (2002) definition of contact area ration $A/A_w = \pi\beta(R_a/\lambda)^2$, wherein β is the pad surface density of about 35%. From force equilibrium as illustrated in Fig. 2.4(a, b), the average local pressure at the asperity level is given by

$$P \equiv \frac{P_0 \cdot A_w}{A} = \frac{\bar{E}_p^{\,2/3} P_0^{\,1/3}}{\lambda} \tag{2a.5}$$

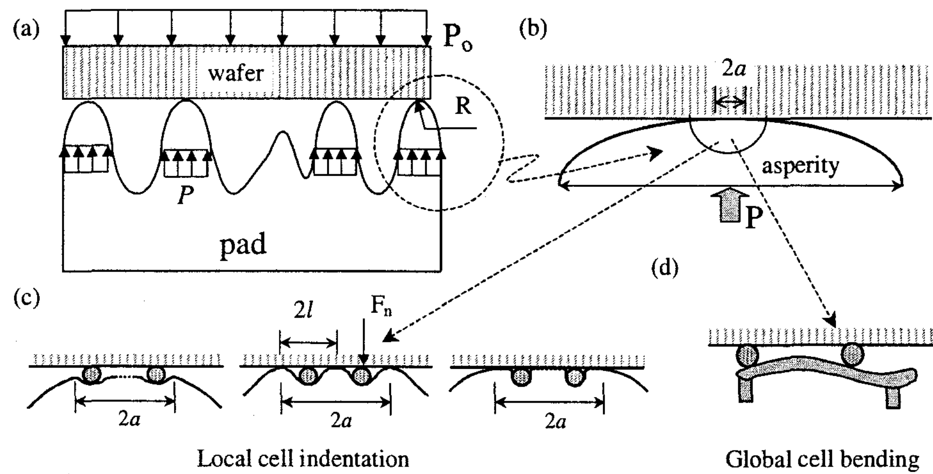

Fig 2.4 Schematic representation of the multi-scale of the wafer/pad contact. (a) Long wavelength multi asperity contact; (b) Details of individual pad asperity contact under local pressure, *P*; (c, d) cell level deformation as a local indentation (with no, partial, or full contact of the wafer/pad interface; d) bending of the entire cell.

The assumptions implied so far are similar to those of Hertz elastic contact model, and

the pad surface roughness has a non-evolving periodic asperities. It is also assumed that the pressure at the asperity level is represented by an equivalent uniform local pressure, instead of the actual local pressure distribution over each asperity.

2.3.2 Determination of the normal force per particle

At the scale of the abrasive particle, Fig. 2.4 shows that the load is carried out either by the wafer/pad or wafer/particle/pad contact. Locally, two deformation mechanisms can be identified and primarily linked to the pad structure based on (I) local cell indentation by individual abrasive particles as depicted on Fig. 2.4(c) (Bastawros et al 2002, Gouda et al 2003) and (II) by overall cell bending as depicted by Fig. 2.4(d) (Fu et al 2001). Based on these two deformation modes, we have identified four deformation mechanisms. Mechanisms (i) through (iii) are associated with local cell indentation and (iv) is associated with overall cell bending.

Local cell indentation depicted in Fig. 2.4(c) is usually associated with soft porous pads similar to the IC1000 pad, wherein the abrasive particle progressively indents the pad surface cells. Deformation mechanism (i) represents the initial state of the wafer pad interaction, wherein the pad and wafer will not come to contact. Mechanism (ii) corresponds to the establishment and evolution of partial pad/wafer contact, wherein each abrasive particle forms the shown "hut" shape over the pad surface. Mechanism (iii) corresponds to the final hypothetical state of a very soft pad or very low slurry concentration, wherein the pad fully enclaves the abrasive particles and comes to full contact with the wafer. Alternatively, Fig. 2.4(d) depicts deformation mechanisms (iv) associated with a fibrous pad like the TWP817 pad, wherein the cells or fibers globally bend around the abrasive particles. This deformation

mode can associate with the porous IC1000 pad if the surface cell thickness are small and large abrasive particles are employed (approximately μm range). More detailed discussion of the combination of different pad deformation modes is given in Gouda et al (2003). These modes of deformation dictate the average local pressure within the long wavelength pad asperities, and the imparted normal forces on individual abrasive particles. The force per particle will be calculated for both modes of deformation as follows.

For mechanism (i) of local pad deformation and no established wafer/pad contact, all the applied pressure will be carried out by the particles within the contact area of the asperity. The slurry is assumed to have an average particle size of diameter *d*, and a homogeneous volumetric concentration α. If the height of the gap between the pad asperities and the wafer is assumed to be the average particle diameter *d* (Zhou et al 2002), then the number of particles that is in contact with the wafer can be given by:

$$N_{partical} \equiv \frac{\alpha A d}{\pi d^3/6} = \frac{6\alpha A}{\pi d^2} \qquad (2b.1)$$

Accordingly, by employing Eq. (2a.5) for the local pressure *P* within individual asperity, then the force per particle F_n will be

$$F_n \equiv \frac{P \cdot A}{N_{partical}} = \frac{\pi}{6} \cdot \frac{\overline{E}_p^{\,2/3}}{\lambda} \cdot \frac{d^2}{\alpha} \cdot P_0^{1/3} \qquad (2b.2)$$

For mechanism (ii) of partial pad/particle/wafer contact, it can be assumed that the normal force per particle is simply the product of the contact pressure between the pad and the particle and the suspended area of the "hut". Based on this assumption and the FEM results of Bastawros et al (2002) for IC1000 pad, the normal force F_n on an individual particle is given by

$$F_n = \frac{\pi}{4}\xi_3 P l^2 \tag{2b.3}$$

where $\xi_3 \approx 1.55$ is a geometric factor used to account for the difference in pressure distribution at the edge in the FEM model (Bastawros et al 2002, dashed line in their Fig 4). The suspended radius l of the "hut" is given by (Bastawros et al, 2002),

$$l = d\xi_2 \left(\frac{P}{E_p^*}\right)^{-m} \tag{2b.4}$$

where $\xi_2 \approx 1.22$, $m \approx 0.38$, are also proportionality and exponent constants respectively, used to represent the power law relation between average local pressure P and the suspended radius l of the "hut" made by the particle in FEM simulation. E_p^* is the elastic modulus of dense pad material (i.e. the modulus of dense polyurethane ~1.7 GPa). Accordingly, F_n will be

$$\begin{aligned} F_n &= \frac{\pi}{4}\xi_3 \left(\frac{\overline{E}_p^{\,2/3}\, P_0^{1/3}}{\lambda}\right)\left(d^2\xi_2^2\left(\frac{\overline{E}_p^{\,2/3}\, P_0^{1/3}}{\lambda E_p^*}\right)^{-2m}\right) \\ &= \frac{\pi\,\xi_2^2\,\xi_3}{4}\cdot\frac{\overline{E}_p^{\,\frac{2}{3}(1-2m)}\, E_p^{*\,2m}}{(\lambda)^{1-2m}}\cdot d^2\cdot P_0^{\frac{1}{3}(1-2m)} \end{aligned} \tag{2b.5}$$

For mechanism (iii) of full pad/particle/wafer contact, the non-contact domain length $2l$ approaches the particle diameter d. Such a mode has been adopted by Luo and Dornfeld (2001), Seok et al (2003) and shown by Bastawros et al (2002) as the limiting case of mechanisms (ii). The normal force per particle is given by

$$F_n \equiv \frac{\pi}{4} d^2 P = \frac{\pi}{4}\cdot\frac{\overline{E}_p^{\,2/3}}{\lambda}\cdot d^2 \cdot P_0^{1/3} \tag{2b.6}$$

For mechanisms (iv) where the pad surface cells or fibers globally bend around the abrasive particles, the cell level deformation can be approximated by bending of a beam or a

plate as depicted in Fig. 2.4(d). For this mechanism, Fu et al (2001) has given the normal force per particle to be:

$$F_n = \left(\left(\frac{4}{3}\right)^5 E_p^* \cdot T_p^3 \cdot \frac{d}{2} \cdot \left(\frac{A}{N_{partical}}\right)^2 \cdot P^3 \right)^{1/4} . \qquad (2b.7)$$

Here T_p is the pad cell wall thickness. Utilizing Eq. (2b.1) for the $A/N_{partical}$ ratio, and Eq. (2.a5) for P, then F_n can be expressed as:

$$F_n = \left(\frac{2}{3}\right)^{7/4} \sqrt{\pi} \cdot \frac{T_p^{3/4} \cdot E_p^{*1/4} \cdot \overline{E}_p^{1/2}}{\lambda^{3/4}} \cdot \frac{d^{5/4}}{\sqrt{\alpha}} \cdot P_0^{1/4} . \qquad (2b.8)$$

Each of the equations for F_n includes three parameter groups. Aside from a scaling factor, the first parameter depends on the pad morphology and elastic modulus. The second group represents the slurry properties and the third is the applied nominal pressure. These groups of parameters can be further expanded to include the stochastic of the process as manifested in particle size distribution and pad surface asperity distribution.

2.3.3 Determination of indentation depth of a single abrasive particle

Once the force per particle is known from the different local pad deformation mechanism, grove depth on the wafer surface can be estimated. First we assume that the chemical reaction in a CMP process creates a "*chemical product*" layer on the wafer surface that can be modeled as a perfectly plastic material. Following Fu et al (2001) to establish the force equilibrium at the particle-wafer interface, the indentation depth can be estimated as

$$h = \frac{F_n}{\pi \cdot \sigma_y \cdot d} \qquad (2c.1)$$

where σ_y is yield strength of material in the chemically reacted layer (taken as

equivalent yield strength) and d is the diameter of the spherical abrasive particle.

2.3.4 Estimation of the characteristic detached length, ℓ_c during scratch intersection

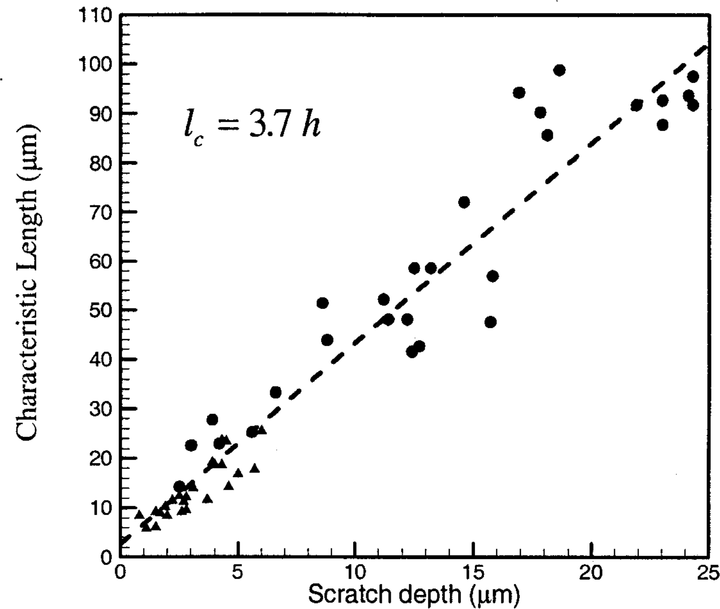

Fig 2.5 Characteristic detachment length variation with the scratch depth.

In our previous work (Che et al 2003) for micro-scratch experiment, it has been shown that the deformation ahead of a moving indenter changes from plowing mode into a shear segmentation mode, triggered by plastic instability near an intersecting scratch. The experiments were carried out on oxygen free, 99.99% high purity copper discs with a 90° included angle conical indenter. The scratch depth is in the range of 1-30μm. The length of the sheared segment ℓ_c is consistently measured for all tested cases and is plotted in Fig. 2.5 against the scratch depth, h at the point of intersection. It is found that the CDR is about 3.7. Using a statically admissible state of stress as that shown in Fig. 2.6 under the indenter for a 2-D orthogonal cutting with negative rake angle, a simple shear failure criterion is derived.

The estimated CDR is found to be 7.6. This higher value of ℓ_c may be due to the approximations involved in comparing results from 3-D experiments against a 2-D orthogonal cutting theory model. Here, we will use a CDR of 4 for the calculation of the MRR.

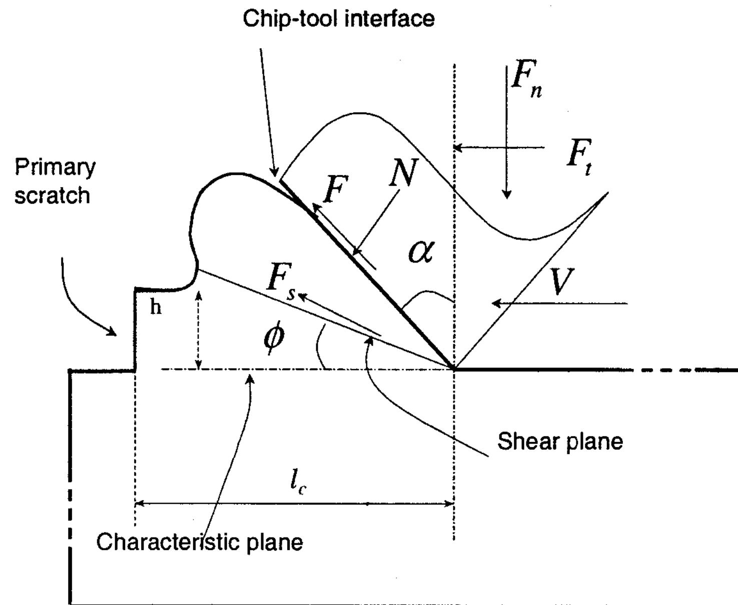

Fig 2.6 Schematic of scratch intersection.

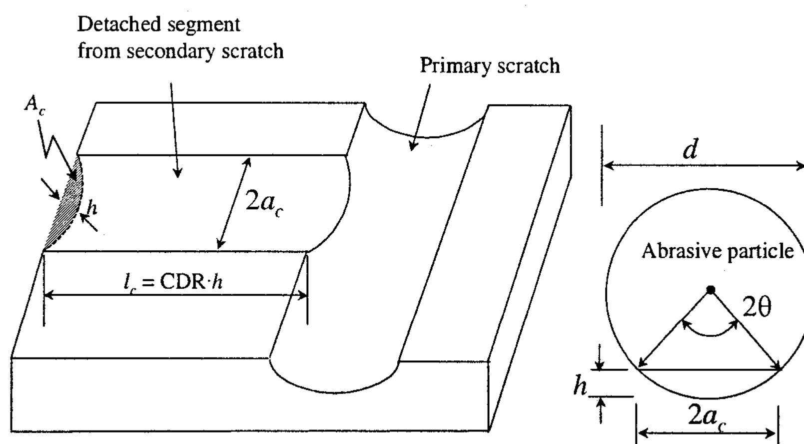

Fig 2.7 Schematic of volume of detached flake at intersection.

2.3.5 Determination of the volume of material removed in an intersection

The volume of removed material per intersection will be function of the indenter (or abrasive particle) profile and ℓ_c. For a spherical particle with diameter d, the formed trench will be having a cross-section, A_c in the form of a segment of a circle, as shown in Fig. 2.7. In CMP, the abrasive particle diameter is about 100nm or greater, while the indentation depth is within a few nanometer. It can be safely assumed that the contact angle 2θ is small. Accordingly, $\sin\theta \cong \theta$ and θ may be approximated as $2\sqrt{h/d}$. For small penetration depth h, the radius of the contact impression a_c can be written as

$$a_c = \sqrt{\frac{d^2}{4} - \left(\frac{d}{2} - h\right)^2} \cong \sqrt{dh}\,, \tag{2e.1}$$

and the cross-section area A_c can be written as

$$A_c \cong \frac{2}{3} \cdot 2a_c \cdot h = \frac{4}{3} h \sqrt{dh}\,. \tag{2e.2}$$

The volume removed per scratch intersection, V_c can be written as

$$\begin{aligned} V_c &\equiv \ell_c \cdot A_c = CDR \cdot h \cdot \left(\frac{4}{3} h \sqrt{dh}\right) \\ &= \frac{4}{3} CDR\ h^{2.5}\ d^{0.5} \end{aligned} \tag{2e.3}$$

Employing Eq. (2c.1), V_c can be rewritten as a function of F_n and σ_y

$$V_c = \frac{4}{3\pi^{2.5}} \frac{CDR}{d^2} \left(\frac{F_n}{\sigma_y}\right)^{2.5} \tag{2e.4}$$

It should be noticed that existing MRR models assume that all the material in the trench is removed, and the volume per unit time is taken as the product of A_c with the velocity of the

particle. Such approach is quite different from the intersection model proposed here.

2.3.6 Determination of the number of intersections per unit area per revolution

The number of intersections per unit wafer area per revolution of wafer depends on several characteristics of the CMP process. The slurry is assumed to have an average particle size of diameter d, and a homogeneous volumetric concentration α. The linear particles velocity, u relative to the wafer is assumed to be uniform across the entire wafer surface (Ouma, 1998). Moreover, the height of the slurry in the gap between protruding pad asperities and the wafer surface is assumed to be the same as the average particle diameter d (Zhou et al 2002). Accordingly, the volume concentration may be represented as a function of the inter-particle distance L_{p-p}

$$\alpha = \frac{\pi d^3 / 6}{L_{p-p}^2 \cdot d} = \frac{\pi d^2}{6\, L_{p-p}^2} \tag{2f.1}$$

Or alternatively,

$$L_{p-p} = \sqrt{\frac{\pi d^2}{6\alpha}} \tag{2f.2}$$

To derive an evolution equation for the scratch intersection, we will follow the abrasive particles trajectories relative to the wafer and forming the first set of track trajectories at time instant t. Then calculate the time increment Δt needed for the wafer to rotate such that the already formed tracks rotate by an angle β_t to allow for the incoming particles to intersect with the previously formed tracks. Fig 2.8 is a schematic representation of a wafer being polished, showing the relative approach of the abrasive particles into the rotating wafer around its axis. A unit cell with edge length L_{p-p} at the wafer center is selected at time t, and its rotated new position $t + \Delta t$.

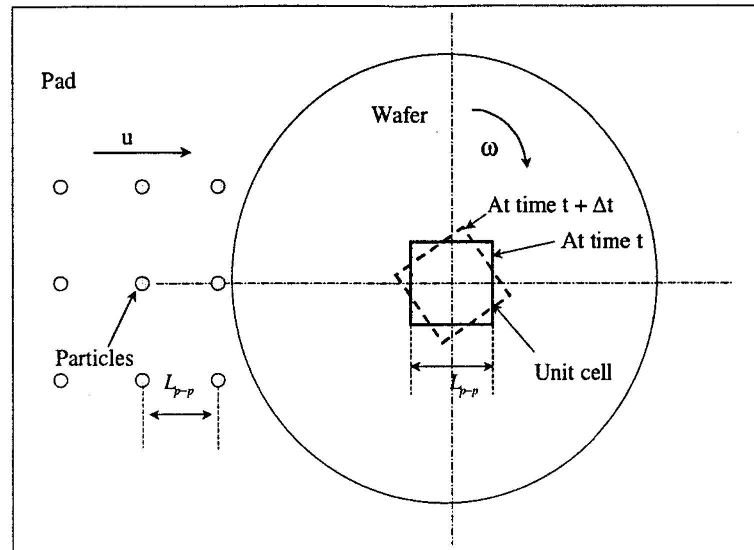

Fig 2.8 A schematic of particle motion in CMP process

By selecting a coordinate axis attached to the wafer, then the unit cell shown in Fig. 2.9 will see the approaching train of particles with different incident angles. Accordingly, each particle in the approaching train will induce a trench with different angle. And the intersection of all these trenches will contribute to the cumulative MRR. However, when the first particle of the train induce a trench in the unit cell at time t, the following particles in this train will not form a new trench until the separation distance x increases beyond a critical value. When the separating distance exceeds this critical value, the i-th particle of train will form a new trench in this unit cell at time $t+\Delta t$. Thus, it is speculated that a new trench is formed only after the wafer rotates by a critical angle of rotation, β_t. Based on this assumption, a simple model is developed to represent the number of intersections per revolution per unit area.

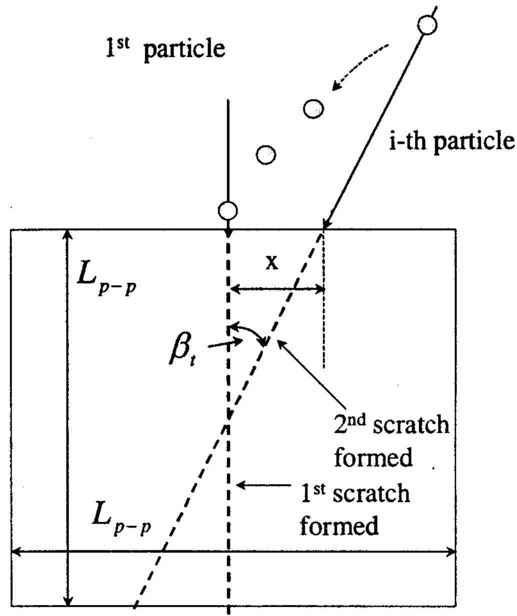

Fig 2.9 A schematic of particles train motion relative to unit cell.

The trailing angle β_t can be approximated by

$$\beta_t = \tan^{-1}\left(\frac{2\,x}{L_{p-p}}\right). \tag{2f.3}$$

A new trench is formed for every β_t angle of rotation. In each full revolution, the number of trenches is

$$N_{rev} = \frac{2\pi}{\beta_t}. \tag{2f.4}$$

Since each pair of the formed trenches may intersect once, then the number of intersections per revolution in this unit cell is given by

$$\begin{aligned} N_{in-cell} &\equiv C_{N_{rev}}^2 = \frac{N_{rev}!}{2!\cdot(N_{rev}-2)!} = \frac{N_{rev}\cdot(N_{rev}-1)}{2} \\ &= \frac{1}{2}\frac{2\pi}{\beta_t}\cdot\left(\frac{2\pi}{\beta_t}-1\right) \end{aligned}. \tag{2f.5}$$

Employing Eq. (2f.2) to normalize Eq. (2f.5) by the area of the unit cell, the number of intersections per revolution per unit area, N_{in} is

$$N_{in} \equiv \frac{N_{in-cell}}{L_{p-p}^2} = \frac{6\alpha}{d^2\beta_t}\left(\frac{2\pi}{\beta_t}-1\right). \quad (2f.6)$$

2.3.7 Estimation of the MRR

Based on our scratch intersection experiment (Che et al 2003), it is more reasonable to apply our new observed material removal mechanism to the MRR model. The MRR is now function of the volume of each scratch intersection V_c, the number of intersection over the percentage of wafer surface that is in contact with the pad $(N_{in} \cdot A)$, and the rotational speed ω. Accordingly, the rate of height reduction is given by

$$\frac{dh}{dt} \equiv \frac{MRR}{A_w} = \frac{\omega \cdot (A \cdot N_{in}) \cdot V_c}{A_w} \quad (2g.1)$$

Utilizing Eq. (2a.4) for the contact area ratio, Eq. (2e.4) for V_c and Eq. (2f.6) for N_{in}, then the height reduction rate can be simplified to be:

$$\begin{aligned} \frac{dh}{dt} &= \omega\lambda\left(\frac{P_0}{\bar{E}_p}\right)^{2/3}\left(\frac{6\alpha}{d^2\beta_t}\left(\frac{2\pi}{\beta_t}-1\right)\right)\frac{4}{3\pi^{2.5}}\frac{CDR}{d^2}\left(\frac{F_n}{\sigma_y}\right)^{2.5} \\ &= \frac{8}{\pi^{2.5}}\left\{\frac{CDR}{\beta_t}\left(\frac{2\pi}{\beta_t}-1\right)\right\}\left\{\frac{\lambda}{\bar{E}_p^{\,2/3}}\right\}\left\{\frac{\alpha}{d^4}\right\}\left\{\frac{1}{\sigma_y}\right\}^{2.5}\left\{\omega \cdot P_0^{2/3}\right\} \cdot F_n^{2.5} \end{aligned} \quad (2g.2)$$

The rate of height reduction is explicitly written in terms of five parameter groups, marked by the curly brackets. These groups are as follows; (1) the process kinematics, (2) the pad surface roughness and mechanical properties (E_p, ν_p, λ), (3) the slurry properties (d, α), (4) the mechanical properties of the chemical product layer (σ_y) and (5) the

external control parameters (P_0, ω). The remaining term is the force per particle. Its implicit dependence on the whole parameter set is dictated by the local mode of pad deformation at the pad cell level. Such dependence will be shown next as the main source for the various (and sometimes contradictory) experimentally observed trends for the MRR.

Mechanism (i) represents the early stage of pad deformation at relatively low applied pressure. It is especially prevalent for a stiff pad and high particle concentration. At this stage, no direct pad wafer has been established. However, it is believed that this regime is usually rare in a CMP process. For this mechanism, the pad deformation mode is predominantly a cell level local indentation by the abrasive particles. Accordingly, by employing Eq. (2b.2) into Eq. (2g.2), the height reduction is given by

$$\frac{dh}{dt} = \frac{8}{6^{2.5}} \left\{ \frac{CDR}{\beta_t} \left(\frac{2\pi}{\beta_t} - 1 \right) \right\} \left\{ \frac{\bar{E}_p}{\lambda^{1.5}} \right\} \left\{ \frac{1}{\sigma_y} \right\}^{2.5} \left\{ \frac{d}{\alpha^{1.5}} \right\} \omega P_0^{1.5}$$
$$\frac{dh}{dt} \propto \frac{d \cdot \omega \cdot P_0^{1.5}}{\alpha^{1.5}} \qquad (2g.3)$$

During this mode of local pad deformation and according to Eq. (2.g3), the MRR should be increasing with the increase of the abrasive particle size and reduced particle concentration.

Mechanism (ii) commences upon increasing the applied pressure, wherein partial pad/wafer contact takes place around the local cell indentation zones by the abrasive particles. This mechanism is believed to widely occur during the CMP processes for soft fumed closed pore pads and relatively small abrasive particle sizes ($\sim 100nm$). Accordingly, by employing Eq. (2b.5) into Eq. (2g.2), the height reduction is given by

$$\frac{dh}{dt}=\frac{\xi_2^5\ \xi_3^{2.5}}{4}\left\{\frac{CDR}{\beta_t}\left(\frac{2\pi}{\beta_t}-1\right)\right\}\left\{\frac{\overline{E}_p^{\frac{1}{3}(3-10m)}\cdot E_p^{*5m}}{\lambda^{1.5-5m}}\right\}\left\{\frac{1}{\sigma_y}\right\}^{2.5}\alpha\ d\ \omega\ P_0^{\frac{1}{3}(4.5-5m)} \qquad (2g.4)$$

$$\frac{dh}{dt}\propto d\cdot\alpha\cdot\omega\cdot P_0^{0.87}\ \text{(for IC 1000 pad)}$$

In contrast with the initial no contact regime (Eq. 2g.3), the MRR is now increasing with both the particle diameter and the concentration increases. Moreover, it has a near linear dependence on the applied pressure.

Mechanism (iii) commences at the hypothetical limit where in the pad fully wrap around each abrasive particles and establish contact with the wafer. Accordingly, by employing Eq. (2b.6) into Eq. (2g.2), the height reduction is given by

$$\frac{dh}{dt}=\frac{1}{4}\left\{\frac{CDR}{\beta_t}\left(\frac{2\pi}{\beta_t}-1\right)\right\}\left\{\frac{\overline{E}_p}{\lambda^{1.5}}\right\}\left\{\frac{1}{\sigma_y}\right\}^{2.5}\alpha\ d\ \omega\ P_0^{1.5} \qquad (2g.5)$$

$$\frac{dh}{dt}\propto d\cdot\alpha\cdot\omega\cdot P_0^{1.5}$$

During this mode of pad deformation, the MRR continue to increase linearly with both the abrasive particle diameter and concentration as set by the pervious stage of mechanism (ii). However, it recovers the strong dependence on the pressure as set by mechanism (i).

Mechanism (iv) accounts for the fibrous structure of CMP pads wherein the deformation mode is approximately bending of the strands. Under partial pad/wafer contact and by employing Eq. (2b.8) into Eq. (2g.2), the height reduction is given by

$$\frac{dh}{dt}=5.68\left\{\frac{CDR}{\beta_t}\left(\frac{2\pi}{\beta_t}-1\right)\right\}\left\{\frac{T_p^{15/8}\cdot\overline{E}_p^{\ 0.583}\cdot E_p^{*5/8}}{\lambda^{7/8}}\right\}\left\{\frac{1}{\sigma_y}\right\}^{2.5}\left\{\frac{1}{\alpha^{1/4}\cdot d^{7/8}}\right\}\omega\ P_0^{1.292}$$

$$\frac{dh}{dt}\propto\frac{\omega\cdot P_0^{1.292}}{\alpha^{1/4}\cdot d^{7/8}} \qquad (2g.6)$$

For this mode of deformation, the MRR becomes inversely proportional with both the

particle sizes and their concentration. However, the pressure dependence remains within the same range.

2.4 Comparison to Experimental Observations

Examining the different forms of the MRR prediction models indicate variable trends on both the particle size and concentration. In some instances, it could be increasing, decreasing or showing no dependence on these two variables. To show the capability of these set of models, we will compare them next to groups of experimental MRR measurements, gathered from literature under different operating conditions.

2.4.1 Preston constant and variation of MRR with pressure and velocity

The first set of experimental results are those of Luo et al (1998) for Cu CMP. These tests were carried out on a Strasbaugh 6CA polisher. The copper-coated wafers (from Silica Source Technology) were used in these experiments. The abrasive particles are α-alumina and γ-alumina particles that are supplied by Universal Photonics. The polishing experiments were performed either with a SUBA IV pad or with a stacked SUBA IV and perforated IC 1000 with IC 1000 on top. The polishing parameters were set 3.5ml/s slurry flow rate. The downward pressure was varied from 10 to 50 kPa. The rotational speed of table and quill was varied from 15 rev/min (7.2 m/min) to 75 rev/min (35.9 m/min). For the results reported here, an abrasive concentration of 5wt%, and mean abrasive size of 100 nm were used.

Since the particle size is relatively small with low concentration, the pad is expected to undergo local deformation for this set of experiments. Thus, the deformation mechanism (ii) is expected to prevail and Eq. (2g.4) will apply be applied. The estimates of model

parameters are shown in Table 1. Pad modulus E_p and v_p is taken for the IC1000 pad (Bastawros et al, 2002). Yield strength of pure copper is taken from the literature. CDR is the proportionality constant for "characteristic detachment ratio" (Che et al, 2003). λ is evaluated to be a constant for IC 1000 pad. β_t is an estimated value. The predicted K is calculated based on Eq. (2g.4), and experimental K is taken from the experimental data from Luo et al, (1998). It is interesting to notice that the model prediction for Preston constant is about 80% of the measured one, despite the fact that no accurate topology measurements of the utilized pad in this experiment has been done. The reported prediction is based on atypical morphology of a used IC1000 pad for about an hour of polishing with intermittent conditioning. Moreover, the variation of the local temperature field may also affect the chemical reaction rate, an aspect of the process that has not been addressed here. The current MRR model resemble the form of Preston formula (Eq. 1a) except that the Preston constant is given here by the detailed pad morphology, the ductile film properties, as well as particle sizes and distributions, rather than using it as a fitting parameter.

Table 2.1 range of parameters for Eq(2g.4)

CDR	λ	β_t	E_p (MPa)	v_p	σ_y (MPa)	d (nm)	α (vol %)	Predicted K (preston's constant)	Experimental K (preston's constant)
4	0.6	10°	180	0.15	70	100	1.25	~1500	~1900

The model prediction is superimposed on the experimental data in Fig. 2.10 for the variation of the MRR with applied nominal pressure, at a rotational speed of $\omega = 35 rev/\min$ (corresponds to 16.8m/min). The variation of the MRR with the relative velocity is shown in Fig 2.11, for a down pressure, $P_0 = 30KPa$.

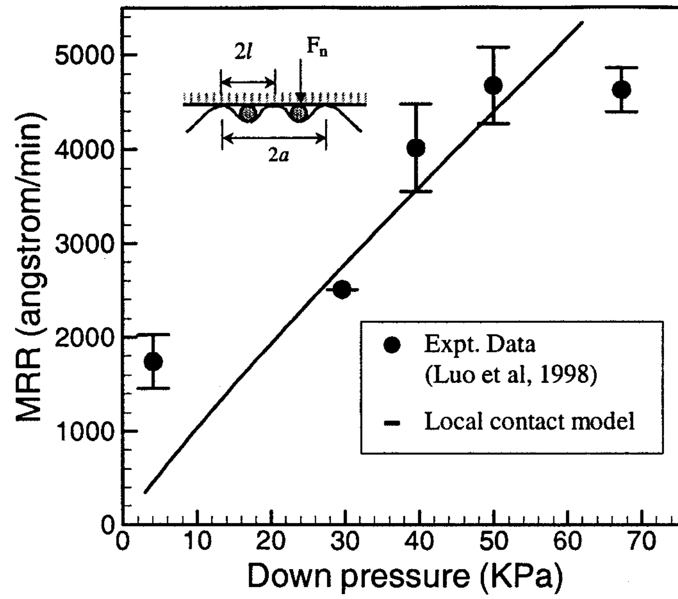

Fig 2.10 MRR variation with pressure for copper CMP data.

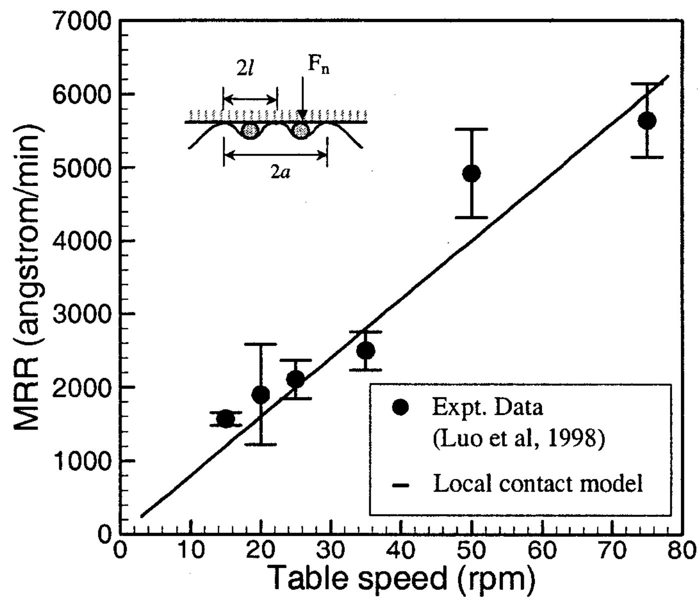

Fig 2.11 MRR variation with velocity (Copper CMP).

It may be observed from both Fig. 2.10 and Fig. 2.11 that model predictions of MRR compare well with the experimental data. It should be noted here, that comparisons shown in Fig. 2.10 and Fig. 2.11 do not involve any "fitting parameter" other than those shown in Table 2.1.

Since the trailing angle is an estimated value, it is imperative to examine how sensitive the MRR estimates relative to variations in β_t. For the sample calculations shown in Table 1, β_t is taken to be 10 degrees as a physically acceptable value to allow three particle diameters spacing before starting new trench. However, if the trailing angle is reduced by 50%, then the ratio of model predicted MRR is about 3 times the experimental MRR. If the trailing angle is increased by 50%, then the model predicted MRR drops to about 1/3 of the experimental MRR data for copper. Accordingly, the choice of $\beta_t=10^{\circ}$ seems kinematically admissible.

2.4.2 Variation of MRR with particle size and concentration

By comparing Eq. (2g.4) with Eq. (2g.6), it is interesting to note that the trend of MRR variation with particle size and concentration completely reverses when the pad deformation mode changes from local deformation to global beam mode deformation. Mahajan et al (2000) have investigated the effects of particle size and concentration on the CMP of silicon oxide film for relatively large (0.2 – 1.5 μm) abrasive particles. These experiments are carried on Struers Rotopol 31 polisher with 7psi down pressure and a rotational speed of 150 rpm for both the wafer and pad. IC1000 and Suba IV stacked pads (supplied by Rodel Inc.) are used. The abrasive particles (obtained from Geltech Corporation) have a very narrow particle size distribution, and the particle size and shape are determined by TEM and SEM. They have also varied the particle concentration from 2wt.% to 15wt.%. Comparisons of

model predictions to their experimental data are presented in Figs. 2.12-2.14. Since the required model parameters are not known, especially the yield stress of the hydroxilated layer, the Preston constant is used as a fitting parameter for these comparisons.

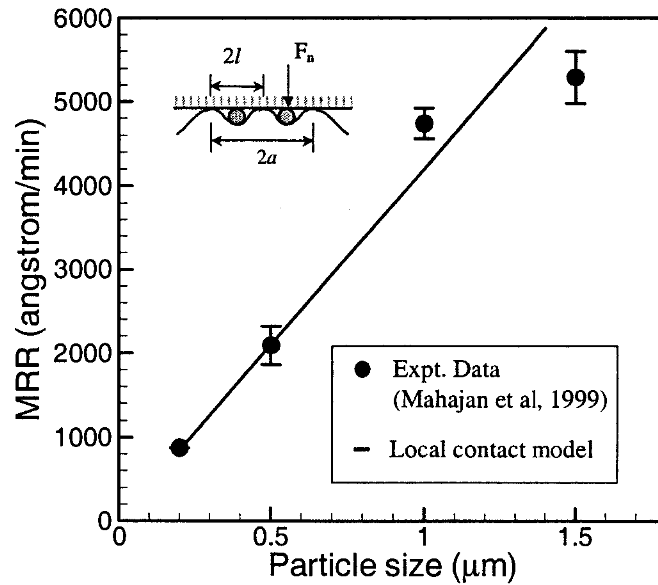

Fig 2.12 MRR variation with particle size for a fixed 2wt% concentration (SiO_2 CMP).

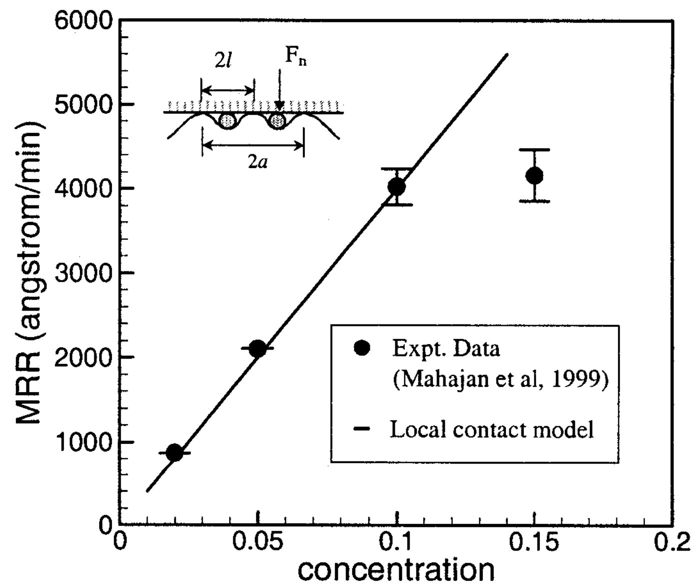

Fig 2.13 MRR variation with concentration for particle size of 0.2 μm (SiO_2 CMP).

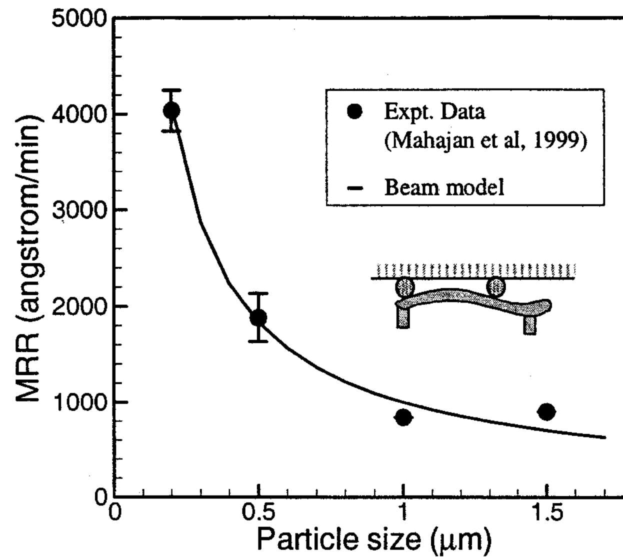

Fig 2.14 MRR variation with particle size for a fixed 10wt% concentration (SiO_2 CMP).

The MRR variation with particle size at a relatively low concentration of 2wt% is shown in Fig. 2.12. In this regime, the pad is expected to undergo local deformation, and equation (2g.4) is anticipated to apply. It is observed that model predictions from Eq. (2g.4) compare well to the experimental trend. As the abrasive size increases, the pad has a greater tendency to be dominated by cell or strand bending deformation, rather than local surface cell indentation. This mode of deformation would cause the experimental trend to "fall off" the linear trend predicted by Eq. (2g.4). Similarly, Fig. 2.13 compares the model prediction of Eq. (2g.4) with the observed experimental trend for MRR variation with particle concentration. The comparison is done for a low concentrations (<15%) and a relatively small particle size of 0.2 μm. Again, good correlation is observed between the model prediction and the experimental measurements for a low particle concentration. As concentration increases, so does the tendency for global beam mode of deformation, and the experimental trend "falls

off" the linear trend predicted by Eq. (2g.4). At a particle concentration of about 10% and higher, the cell or strand bending dominate the response of the pad. This situation is depicted in Fig. 2.14. It is observed that MRR decreases with increasing particle size in this regime. The experimental trend correlates very well to the prediction obtained from the beam model (Eq. 2g.6).

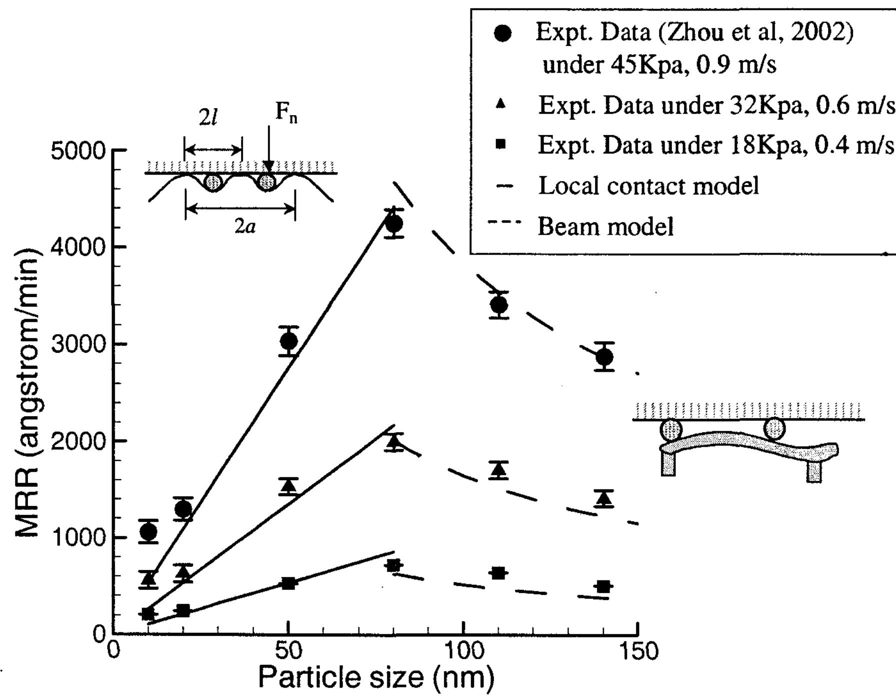

Fig 2.15 MRR variation with particle size (SiO_2 CMP).

Another set of experimental measurements, investigating the effect of abrasive particle size is carried out by Zhou et al (2002). These experiments are carried on Struers Rotopol 35 polisher. The grooved IC1000 pad (supplied by Rodel Inc.) is used in all the experiments. The abrasive particles have a very narrow particle size distribution with average particle diameters of 10, 20, 50, 80, 110 and 140 nm. The abrasive concentration was varied by

diluting the 30wt% concentration slurry with DI water to obtain 1, 5, 10, 15, 20 and 25wt%. The pressure was varied from 18 kPa to 45 kPa, and the table speed was varied from 0.4 m/s to 0.9 m/s. Similarly the Preston constant is used as a fitting parameter for model prediction in Fig. 2.15 by fitting a single data point to get the scaling factor then use it for the entire data set.

Figure 2.15 shows the variation of MRR with particle size for relatively small particles (10-140 nm) at a relatively high concentration of 30wt% by weight. It is observed that the MRR initially increases with particle size, saturates at around particle size of 80 nm, and decreases with further increase in particle size. Zhou et al (2002) have conducted these experiments at three different operating pressures and velocities. The experimental data points are shown by symbols. The experimental trends are then compared to model predictions from two different regimes. It may be assumed that the pad undergoes local deformation at smaller particle sizes, and Eq. (2g.4) is thus applicable at smaller particle sizes. At larger particle sizes, the pad undergoes global beam mode of deformation, thus Eq. (2g.6) is applied in that regime. It is observed that the model predictions in both regimes fit the experimental trend very well.

2.5 Discussion and Concluding Remarks

A new mechanism for ductile material detachment from the parent surface based on scratch intersection is proposed in this paper, and applied to MRR prediction of CMP processes. This is a departure from existing MRR models, where it is assumed that a moving abrasive particle removes material all along its track. The present model assumes that material is plowed to the side (but not detached) along a particle's track. However, it is only

detached when the deformation profiles of two tracks intersect each other at a favorable angle. The proposed scratch intersection model is physically motivated, and provides predictions for Preston constants with the same order as those measured experimentally for CMP of copper (Figs.2.10 and 2.11). This is in contrast to existing practice where Preston constant has typically been used to fit the model predictions to experimental observations. To further realize the model utility of the scratch intersection concept, if one would compare any of the existing models that relies on the assumption of removal of materials along the entire track of the abrasive particle, then the predicted MRR would be about three order of magnitude higher than experimental measurements. Moreover, the scratch intersection model prediction of MRR variations with pressure and velocity are also very similar to observed experimental trends.

It has been observed in the literature (e.g., Zhou et al 2002, Luo et al 1998, Mahajan et al 1999) that under different conditions, the MRR may show an increasing or decreasing trend with increasing particle size and concentration. It is observed in our model developments that this apparent ambiguity is due to different regimes of slurry-pad interactions, which induce completely different deformation modes and its associated force partitioning in the CMP process. The proposed scratch intersection based CMP model delineates these different regimes of operation. It is noted that for soft pads subject to relatively small particle sizes and low particle concentrations, the pad undergoes a local deformation pattern where the abrasive particle indents the pad surface. The force partition associated with such a deformation mode causes increasing trend in MRR with increasing particle size and increasing particle concentration. As the particle size and concentration increases, the pad deformation mode changes from the local "indentation" deformation mode

to more global deformation, where cells or strands on the pad surface deform globally by bending. In this regime of slurry-pad interaction, the nature of force partition changes, causing decreasing trend in MRR with increase in either particle size or particle concentration. The proposed scratch intersection models can capture both regimes, and the model predictions correlate quite well to experimental observations.

As predicted by the proposed scratch intersection model, the MRR trend with increasing particle size and concentration is seen to switch from an increasing trend to a decreasing trend as a critical value of particle size and concentration (relative to pad stiffness) is exceeded. Such a trend is clearly observed in the experimental data of Mahajan et al (2000). The transition point also shifts depending on specific particle size and concentration. Determination of such transition points is the focus of our further research in this area.

The proposed model provide a handle on understanding the origin of the Preston constant and provides means to predict this constant as a function of the full process parameters, including detailed pad morphology, particle size and concentration, polished surface mechanical properties as well as the external control variables of applied pressure and relative velocities. Such detailed model would provide the means to explore the design space and optimize the process parameters. Moreover, by including the details of the pad morphology, one would be able to predict the performance degradation and generation of defects due to pad wears and pore clogging. These issues are currently being addressed within the proposed framework of models.

2.6 References

1. Bastawros, A.-F., Chandra, A., Guo, Y., and Yan, B., Pad effects on material removal rate

in chemical mechanical planarization, Journal of Electronic Materials, Vol. 31, No. 10 SPEC., pp 1022-1031, October 2002.

2. Chandra, A., Profile rolling of gears: a boundary element analysis, J. Eng. Ind., ASME, Vol. 111, pp 48-55, 1989.

3. Che, W., A Study on material detachment mechanism in CMP process, MS Thesis, Dept. of Mechanical Engineering, Iowa State University, 2002.

4. Che, W., Guo, Y. Chandra, A. and Bastawros, A.-F, Mechanistic understanding of material detachment during micro-scale polishing, Journal of Manufacturing Science and Engineering, Transactions of the ASME, Vol. 125, No. 4, pp 731-735, 2003.

5. Cook, L. M., Chemical mechanical polishing in silicon processing, Semiconductors and Semimetals, San Diego, CA, USA, Academic Press, Vol. 63, pp 156-166, 2000.

6. Fu, G., Chandra, A., Guha, S. and Subhash, G., A plasticity based model of material removal in chemical mechanical Polishing (CMP), IEEE Trans. Semiconductor. Mfg., Vol. 14, No. 4, pp 406-417, 2001.

7 Gouda, S. D., Bastawros, A.-F. and Chandra, A., Multi-scale characterization of pad role on material removal rate in CMP, Materials Research Society Symposium - Proceedings, Vol. 767, pp 95-100, 2003.

8. Johnson, K. L., Contact Mechanics, Cambridge, New York, Cambridge University Press, 1985.

9. Kuehn, J., Particle scale and wafer scale effects in chemical and mechanical planarization (CMP), MS Thesis, Dept of Mechanical Engineering and Engineering Mechanics, Michigan Technological University, 2000.

10. Lange, K. and Kurz, N., Theoretical and experimental investigation of the "Groz" cold

shape-rolling process, Inst. for Metal Forming Report, University of Stuttgart, Germany, 1984.

11. Luo, J. and Dornfeld, D.A., Material removal mechanism in chemical mechanical polishing: theory and modeling, IEEE Trans. Semiconductor. MFG, Vol. 14, No. 2, pp 112-133, 2001.
12. Luo, Q., Ramaranjan, JS. and Babu, S., Modification of the Preston equation for the chemical-mechanical polishing of copper, Thin Solid Films, Vol. 335, pp 160-167, 1998.
13. Mahajan, U., Bielmann, M. and Singh, R.K., Abrasive effects in oxide chemical mechanical polishing, Materials Research Society Symposium Proceedings: Chemical Mechanical Polishing – Fundamentals and Challenges, Vol. 566, pp 27-32, 1999.
14. Ouma, D.O., Modeling of chemical mechanical polishing for dielectric planarization, Ph.D Thesis, Dept. Electrical Engineering and Computer Science, Massachusetts Institute of Technology, 1998.
15. Preston, F.W., The theory and design of plate glass polishing machine, J. Soc. Glass Tech., Vol. 11, No. 44, pp 214-256, 1927.
16. Seok, J., Sukam, C. P., Kim, A. T., Tichy, J. A. and Cale, T. S., Multiscale material removal modeling of chemical mechanical polishing, Wear, Vol. 254, pp 307-320, 2003.
17. Shaw, M.C., Metal Cutting Principles, Oxford, Clarendon Press, 1984.
18. Xie, Y, and Williams, J. A., The generation of worn surfaces by the repeated interaction of parallel grooves, Wear, Vol. 162-164, pp 864-872, 1993.
19. Zhou, C., Shan, L., Hight, R., Danyluk, S., Ng, S. H. and Paszkowski, A. J., Influence of

colloidal abrasive size on material removal rate and surface finish in SiO_2 chemical mechanical polishing, Lubrication Eng., pp 35-41, August 2002.

Chapter 3 Material Removal Mechanism Part I: Chemical Assisted Mechanical Abrasion by a Softened Layer Formation

3.1 Literature Review

The mechanisms of wafer surface deformation under the abrasive particles are cutting, ploughing, or forming intermittent pileups with successive shearing, based on the study of Hokkirigawa et al (1988) and Gahilin et al (1998). The cutting process resembles macroscopic surface machining, wherein the surface material is detached through a micro-shear localization process. In the ploughing process, the surface material ahead of the abrasive particle is plastically flowing to the trench sides with no net material losses. A third mechanism has been also observed wherein the deformed surface material is piled ahead of the abrasive particle, and then it is sheared off, forming intermittent debris. The competition between these mechanisms depends on the applied loads, relative sliding velocity, the abrasive particle shapes (rake angle), and the ability of material to withstand high plastic deformation without shear localization (material's ductility).

Generally fracture mechanism is predominant in brittle materials, and plastic shearing mechanism is predominant in the polishing process. Brown (1987) showed that the difference between these two mechanisms can be triggered by different cutting depths and abrasive size, and the mechanism transitions could be related to both physical and chemical properties. So in silicate materials, the transition from brittle to plastic may be explained in this way.

Tomozawa (1997) proposed a material removal mechanism for oxide CMP. The surface was softened by friction heat, and further weakened by hydration. Then the abrasive particles

easily scraped off the hydrated surface. So the plastic deformation and hydration of oxides were the main mechanism in oxide CMP.

Zhao and Bhushan (1998) used SEM and TEM to study the material removal mechanism of single-crystal silicon on nano-scale. It was shown that at ultra-low loads, material was removed from single-crystal silicon by abrasive wear with plastic deformation. At heavy loads, the material was primarily removed by a cutting process, like machining of ductile metals.

The mechanical aspect of material removal mechanism during CMP had been investigated. Detailed analysis (luo et al 2001, Fu et al 2001, Bastawros et al 2002, Seok et al 2003) had shown that the pressure dependence on MRR was non-linear with exponent ranging from 0.33 to 1.5 based on the details embraced by the models. All of the existing polishing models assumed that each abrasive particle under the applied load generated a continuous trench, and all the material in the trench was removed from the surface. Such a model was applicable at the macro-scale and was in agreement with the conventional card model (Shaw 1984) used in metal cutting. However, it was suggested that the material removal mechanism at the micro- and nano-scale was different. At these very small depths of cut, the abrasive particle formed a continuous trench, but the material was not detached from its parent surface. It merely flew from the bottom of the trench to the side via stable plastic deformation. Such deformation pattern had been observed in nano-scale AFM indentation and scratch tests (Kuehn 2000, Xie et al 1993), and was akin to profile rolling of gears (Lange et al 1984, Chandra et al 1989). It was shown that material removal occurred later as a result of plastic instability due to interaction of scratches. This interaction may be in the form of intersection of two scratches (Che et al 2003) or may be due to the vicinity of two

parallel scratch-tracks (Xie et al 1993). It can also result from metal fatigue due to repeated plastic deformation in the pile-up region beside the trenches produced by the abrasive particles.

The chemical aspect of material removal mechanism was first proposed by Kaufmann (1991) to explain CMP of tungsten. In this mechanism, it was proposed that mechanical abrasion removed the passivated oxide layer on the top asperity followed by accelerated chemical dissolution of exposed metal. The intact oxide in the recessed area protected the surface from dissolution. This mechanism could be applied to noble metal, copper, in alkaline solutions, since passivating oxide formed on the surface. For acid solutions, corrosion inhibitors such as benzotriazole (BTA), which formed passivating layers, were added in the slurries. These passivating films would play the role of oxide layer in the abrasion-dissolution mechanism (Capio et al 1995, Luo et al 1997). Steigerwald (1995) described a dissolution-abrasion mechanism. The role of chemicals was to dissolve the abraded metallic debris left by abrasion. The material removal rate was just the mechanical abrasion rate, which was equal to the chemical dissolution rate.

As the name of chemical mechanical planarization, this process has not only the chemical effects but also the mechanical effects. Usually the chemical effects and mechanical effects are considered individually and independently, and the interaction patterns of the chemical dissolution and mechanical abrasion are not taken into account. During CMP process, we may imagine that material removal is due to a combination of chemical effects and mechanical effects (individual and coupled chemical and mechanical effects). The goal is to get a high MRR and a good surface quality by a good combination of chemical and mechanical effects. For example, the chemical dissolution may be enhanced by mechanical

abrasion, fluid flow and other factors in the mechanical removal. Chemical exposure may also soften the surface by forming a soft chemical product layer. So a desired MRR model and planar surface are the combined results of chemical and mechanical effects.

Instead of considering chemical or mechanical aspect independently for CMP process, this chapter focuses on the interaction patterns between chemical dissolution and mechanical abrasion, especially the effect of soft layer formation on mechanical abrasion. The different types of slurries, which are commonly used for CMP, are chosen to study the effect. It is speculated that the chemical interactions will weaken the mechanical strength of the top surface layer and form a soft layer; which is much easier to be removed than the original reference material. A complimentary technique (in development with Hysitron, Inc.) utilizing nano-scratch, nano-DMA test and FEM simulation is used to explore the characteristics of the soft layer. The nano scratch tests are described in section 3.3 and 3.4. The DMA test and FEM are addressed in section 3.5 and 3.6.

3.2 Sample Preparation

The experimental techniques utilized nano-scratch, nano-DMA on the copper surface in dry (without chemical exposure) and wet conditions (with chemical exposure). Copper film is electrodeposited onto oxygen free, 99.99% high purity copper (101-alloy series) discs in order to get a similar microstructure of copper used in semiconductor process. The plating bath is $CuSO_4 \cdot 5H_2O$ and H_2SO_4 based on Weisenberger et al (1978). Copper is deposited for 1 hour under constant voltage 0.5 V. A thick layer (more than 50 μm) is achieved based on the experimental conditions (Weisenberger et al, 1978). Then the specimen is recrystallized under room temperature for more than 1 day to achieve the grain size in the order of 1-2 μm

(Gignac et al 1999). Finally the specimen is gently polished with 1 and 0.05μm alumina particles to get a smooth surface with roughness in the order of 3-4 nm over 20μm by 20μm window. Then the specimen is stored in a vacuum chamber. Before each individual test, the specimen is cleaned with 2wt% HNO_3 for 1 minute to remove the native oxide layer.

3.3 Experimental Investigation Utilizing Nano Scratches

Nanoscratch testing can be used for analysis of both thin films and bulk materials. It provides the capability to study modes of deformation and fracture that are not possible using standard indentation techniques. It is done by applying a normal load in a controlled loop of force feedback while measuring the force required to move the tip laterally across the sample. By selecting the appropriate load function and lateral displacement pattern, many different types of tests can be performed. (www.hysitron.com).

When copper surface is exposed to certain slurry with for some time, a surface layer should form due to chemical reaction. This layer could be hard or soft compared to the substrate material, thus affect the deformation mode when the indentation depth is comparable to layer thickness. A thin film characterization technique is devised and conducted to understand the thickness and properties of the formed surface layer due to chemical reaction. It is reasonable to think that, by doing scratch tests in the near surface (assuming scratch depth is comparable to layer thickness), the mechanical response should be different between dry test (copper surface without chemical exposure) and wet test (copper surface with chemical exposure). Whether the film is hard or soft can be identified by comparing the scratch depth at the same normal force, or the scratch depth at the same tangential force between wet and dry conditions. So a set of scratch tests with different

nominal normal force are conducted on the dry and wet copper surface in the same specimen. The scratch depth, normal and tangential force are measured along the scratch, and the results for dry and wet conditions are compared to find out the characteristics of the surface reacted layer.

Three different slurries that are commonly used for CMP (Steigerwald et al 1997, Carpio et al 1995, Singh et al 2002) process are selected to generate a top layer with different layer thickness and properties. The first slurry is 0.6wt% NH_4OH that is an alkaline solution. The second slurry is 5wt% H_2O_2. The third one is 1.0wt% HNO_3+ 0.5wt% BTA that is an acidic type solution plus inhibitor. The nano scratch experiments are conducted on Hysitron Tribo-indenter. The length of the scratch is set to be 5 μm by using a tip with sub micron radius. For 0.6wt% NH_4OH slurry, the applied nominal normal force during scratch is 10μN, 20μN, 30μN and 40μN individually; For 5wt% H_2O_2 slurry, the applied nominal normal force during scratch is 60μN, 80μN, 100μN and 120μN individually; For 1.0wt% HNO_3+ 0.5wt% BTA slurry, the applied nominal normal force during scratch is 40μN, 60μN, 80μN and 100μN individually. At each normal force, the scratch test is repeated 4 times. A total of 16 scratches are made for each experiment. The scratch test is performed first on copper under dry condition (without chemical exposure), then the specimen is etched with selected slurry for a certain time (For 0.6wt% NH_4OH slurry, the exposure time is 90, 300 and 600s; For 5wt% H_2O_2 slurry, the exposure time is 75, 150 and 300 s; For 1.0wt% HNO_3+ 0.5wt% BTA slurry, the exposure time is 600s) and dried by using air duster, after that another 16 scratches are made on the chemically exposed surface immediately..

3.3.1 Mechanism of running scratch test by nano-indenter

Lateral (X-axis) forces using a 2D transducer system are applied and measured in the same manner as they are using indentation system (Z axis). The forces are applied electro-statically and the displacements are measured with a different capacitor technique. During the scratch, the X-axis is under displacement control, rather than the load control used for Z-axis measurement. This means there is a control loop to apply the proper forces.

Fig 3.1 shows schematic of 2D transducer of nano-indenter. There are two additional force-displacement sensors to monitor and control the position in the X-direction.

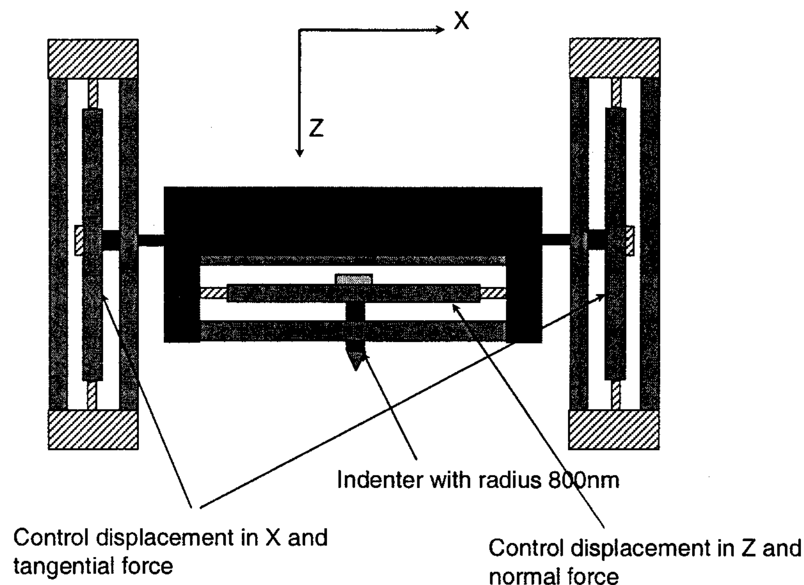

Fig 3.1 schematic of nano-indenter 2D transducer (Hysitron Corp)

3.3.2 Experimental procedure and data analysis of running nano-scratch

1. Experimental procedures of running scratch test.

Scratch test is done by the Hysitron nano-indenter. The testing procedure is elaborated

below, which is designed to find out the different material response between dry test and wet test.

1) Start the nano-indenter and run standard calibration same as running nano indentation.
2) Calibration of X-axis by running an air scratch (repeat calibration of X-axis every 1 hour to make sure the calibration constants are OK).
3) Set up the scratch load function for desired normal force, such as 10uN, 20uN, 30uN and 40uN. A typical scratch load function is shown in Fig 3.2 and described in next section.
4) Determine the surface tilt direction by running a single scratch using imaging panel. Then decide the scratch direction in scratch load function in order to keep the indenter tip in contact with the surface.
5) Select the scratch positions for different normal force and scratch patterns. Set up the method to run scratches automatically.
6) First run dry scratch tests using method on the dry copper surface (without chemical exposure) at desired group of normal force.
7) After dry test, the copper is exposed to the slurry (such as 0.6wt% $NH4OH$) for a certain time (90, 300 or 600 s). Then the surface is carefully dried by pure air.
8) Repeat the calibration of X-axis.
9) The wet scratch tests are immediately made using the same scratch load function on the surface close to the testing area where dry scratches were made.

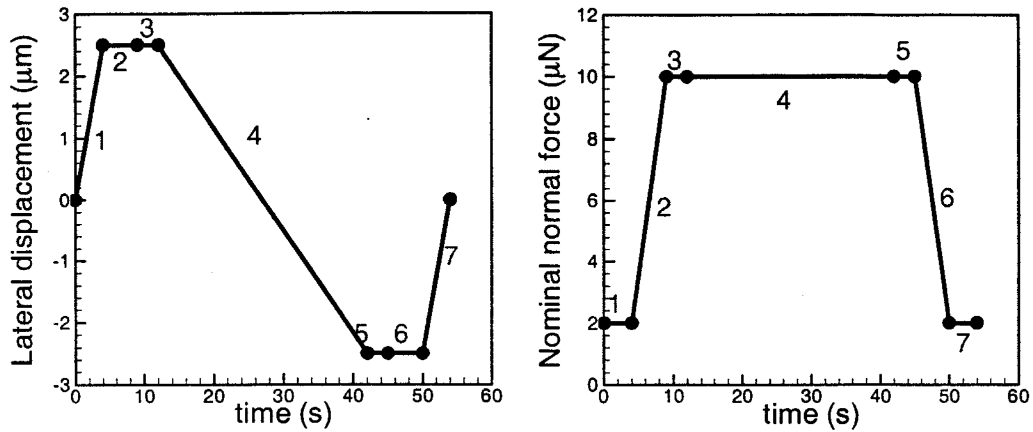

Fig 3.2 Schematic of scratch load function (a) Lateral displacement of indenter vs. time, (b) Nominal normal force of indenter vs. time.

2. Description of the scratch load function.

Typical applied scratch load function is shown in Fig 3.2. Fig 3.2 (a) shows the variation of lateral displacement with time. The scratch length is set to be 5 μm, and the scratch direction is from positive X to negative X (nano-indenter stage coordinate). Fig 3.2 (b) is applied nominal normal force with time. The expected normal force during scratch is 10μN, and the tip contact force before scratch is 2μN. There are 7 segments in the scratch load function. The description of each segment is as follows:

1) 1st segment: The indenter tip moves to +2.5um in X axis (Nano-indenter moving stage coordinate system) as normal load remains 2 uN (set point for contact force, can be changed.), which is the contact normal force to keep the tip in contact with the surface.

2) 2nd segment: The indenter tip holds at +2.5 um in X axis for 5 s to stabilize. During this hold, the normal load is ramped up to the normal scratch force (10 uN in this case).
3) 3rd segment: The indenter tip holds at +2.5 um in X axis for 4 s to stabilize. Normal force holds at the scratch load (10 uN) to stabilize. Suggested by the manual, the hold periods will stabilize the transducer before the start of the movement, and will allow the control loop to keep up with the movement.
4) 4th segment: This scratch is performed on the surface. The indenter tip moves from +2.5um to – 2.5um in X axis over 30 s periods. During this time, the normal load is held at the scratch force, and the tangential load is monitored during the scratch.
5) 5th segment: The indenter tip holds at the end of scratch to stabilize. Normal load is also held.
6) 6th segment: The indenter tip holds to stabilize. Normal load is removed.
7) 7th segment: The indenter tip returns to zero position in X axis (origin). The normal load is at contact force.

3. Data analysis of scratch data output

a) Actual scratch profile output description:

Fig 3.3 and 3.4 are typical scratch profiles output with different scratch direction. Fig 3.3 shows a scratch running from positive X to negative X. it can be seen from Fig 3.3(c), the tip moves upwards along the surface from the origin to the beginning of the scratch position, which is the negative Z direction.

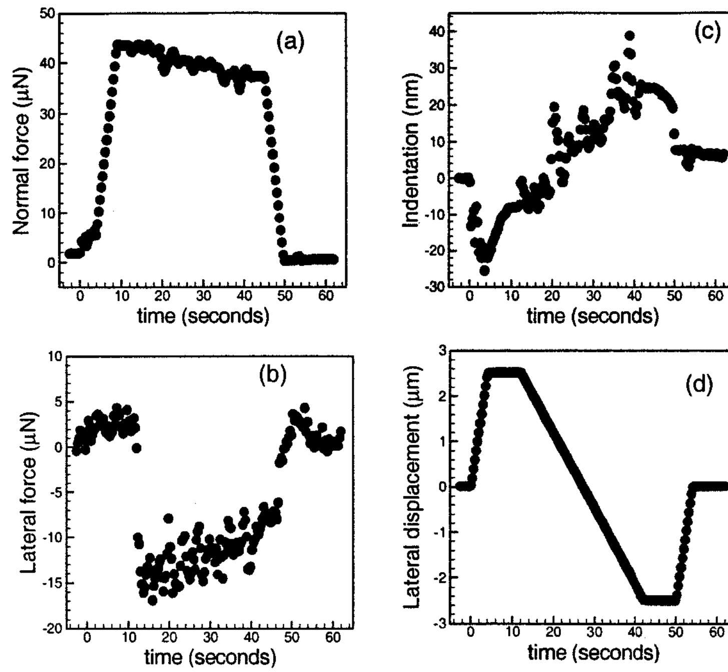

Fig 3.3 Output of scratch profile (uphill)

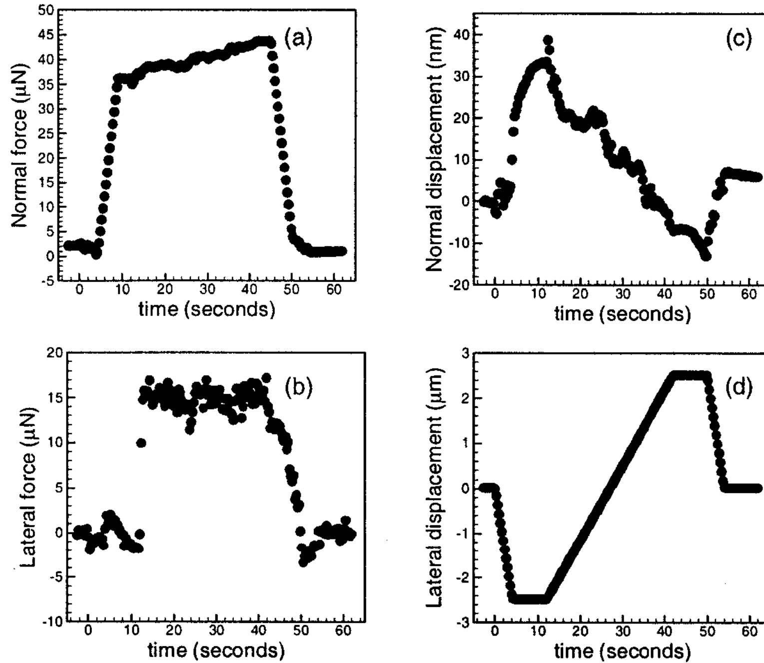

Fig 3.4 Output of scratch profile (downhill)

Fig 3.4 shows a scratch running from negative X to positive X. As shown in Fig 3.4(c), the tip moves downwards along the surface from the origin to the beginning of the scratch position, which is the positive Z direction. Fig 3.3(a) and 3.4(a) shows the variation of applied normal force with time; Fig 3.3(b) and 3.4(b) shows the variation of tangential force with time; Fig 3.3(c) and 3.4(c) shows the variation of the scratch depth with time; Fig 3.3(d) and 3.4(d) shows the variation of lateral displacement with time which is set in scratch load function.

Since the surface is slightly tilted during the experiment as shown in Fig 3.3(c) and Fig 3.4(c), it should be corrected before measuring the scratch depth. It is suggested in the manual that surface tilt should be corrected based on the 1st segment, because the tip is supposed to travel half of the scratch length along the surface in the 1st segment. So the slope of the 1st segment in Fig 3.3(c) or Fig 3.4(c) is measured and taken as the slope of the surface in the scratch direction, and then this slope is removed from the rest of the data by subtraction. However, from Fig 3.4 (a), it is clearly shown that the nominal normal force is nearly 0μN at the end of 1st segment, which means the tip is in the air because the contact force should be 2μN when the tip is in contact with the surface. So the slope of the 1st segment is not the slope of the surface, the surface tilt correction based on the subtraction of the slope of the 1st segment has undetermined error. Similarly, from Fig 3.3(a), at the end of 1st segment, the nominal normal force is larger than the set point 2uN, which means there is a preload. So the tip actually indented into the surface with that preload, then the slope of 1st segment is also not the surface slope in scratch direction. So the surface tilt correction method suggested by the manual doesn't work in the current experimental conditions.

b) Description of the actual scratch track

Since the surface is tilted in a small angle, even if it is less than 1 degree; the results will be biased for a 5μm long scratch with scratch depth in the order of 10nm if no surface tilt correction is made.

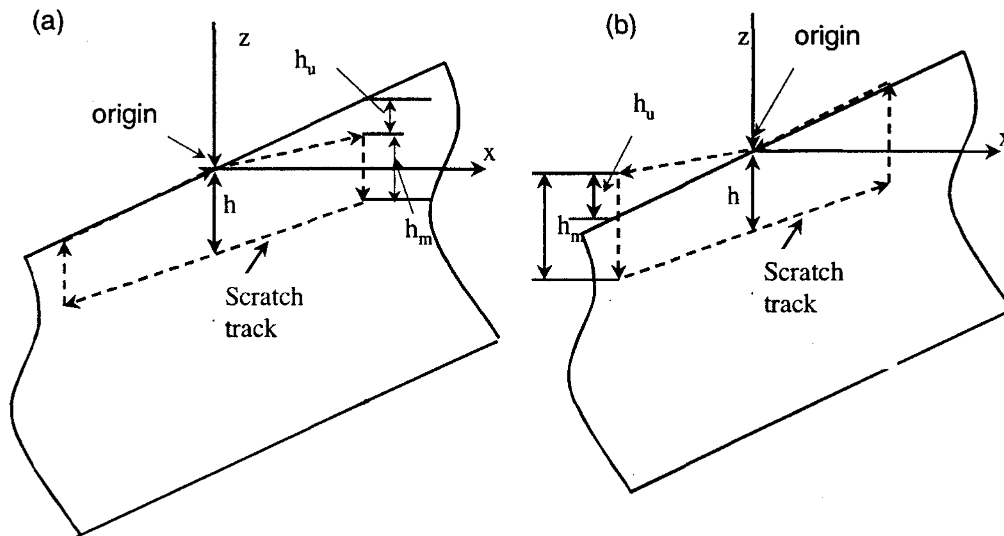

Fig 3.5 Schematic of scratch motion on the surface (a) upwards (b) downwards

When the tip move upward, the actual scratch track is schematically shown in Fig 3.5(a). In the 1st segment of the scratch, when the indenter tip moves along the surface from 0 (origin) to 2.5um in X axis (beginning of the scratch), the control loop of nominal normal force is turned off (it is the way the scratch works in nano-indenter). So as the indenter tip moves upwards, the indenter will indent into the surface. There is a preload larger than the set point force before applying the nominal normal force as shown in the 1st segment in Fig 3.3(a). It is also clearly shown in Fig 3.5(a) that the slope of scratch track in the 1st segment is different from the slope of the actual surface. If we look at the actual data, as shown in Fig

3.3(a), when the tip moves upwards, before the beginning of the scratch, there will be a preload in the range of 6 to 10uN depending on the surface roughness and the tilted angle. During the scratch, as the tip go downwards, the normal force is reduced continuously because the actual scratch depth is continuously decreased as shown in Fig 3.5(a), and the absolute normal displacement is increased as shown in fig 3.3(c).

When the indenter tip moves downward as shown in Fig 3.5(b), the indenter tip will set in the air at the beginning position of the scratch, losing contact with the surface. As shown in fig 3.4(a), the nominal normal force is smaller than the set point 2uN, which is set to keep the tip in contact with the surface. When the nominal normal force is applied in the 2nd segment, the indenter tip will first travel in the air, then go into the surface. This phenomenon can be seen clearly in the experimental data. As shown in the force displacement plot of the 2nd segment, the increasing rates are different if the tip is traveling in the air or in the specimen.

In this experiment, the tilted height is about 30nm over 5um long segment. So it will influence the accuracy of the scratch depth measurement if surface tilt is not corrected. Since the surface tilt correction suggested by the manual doesn't work well in this case, other scratch depth measurement technique has to be developed.

c) Scratch depth measurement.

As discussed in the above section, when surface is tilted, the tip is no longer on the surface of specimen at the beginning of the scratch; the tilt correction based on the 1st segment will not give an accurate tilt correction. A better way of measuring the mean scratch depth should be investigated.

Can we measure the mean scratch depth at the beginning of the scratch? Since the

normal displacement is taken as 0 at origin in X-axis as shown in fig 3.3(c) or fig 3.4(c), so the other positions during the scratch track are all absolute values in this configuration. At the beginning of the scratch there is an unknown depth h_u as shown in fig 3.5(a) and (b), and the measured scratch depth by nano-indenter is h_m. However, the actual scratch depth is $h_u + h_m$ as shown in Fig 3.5 (a) (when tip moves upward) or $h_m - h_u$ in Fig 3.5 (b) (when tip moves downward). Clearly, the measured scratch depth at the beginning of the scratch is not exactly the correct scratch depth.

If we consider the center point of the actual scratch, it is the point right below the origin. At the beginning of the 1st segment (the origin), the tip is in contact with the surface, and the position is set to 0 in X-axis and 0 in Z-axis. During the scratch, when the indenter tip crosses the center position (0 in X-axis) again, the absolute z position (value in Z-axis) is measured. So it is a more accurate measurement if the scratch depth is measured at the center point of the scratch (0 in X-axis). At this point, the absolute z position (value shown fig 3.3(c) or fig 3.4(c)) is the scratch depth. So the means scratch depth can be measured at the center point of the scratch, which is right below the origin,. Since the surface has a short wavelength of about 100 to 200nm, the data is averaged in half cycle before and half cycle after the center point to reduce the effect of surface roughness. The interspacing between two data point during scratch is set to be below 5nm to get an accurate measurement.

3.3.3 Experimental results for scratch data

For copper CMP, NH_4OH, H_2O_2.and HNO_3 plus BTA are three commonly used base slurries (Steigerwald et al 1997, Carpio et al 1995, Singh et al 2002). For NH_4OH and H_2O_2 type slurries, copper oxides, Cu_2O or CuO, is identified to be the surface layer material on

the copper surface based on XPS (X-ray photo-electron spectroscopy) measurement (Steigerwald et al 1997). However, surface layer characteristics, such as layer thickness and mechanical properties, are not investigated. For HNO_3 plus BTA, a non-native surface layer, Cu-BTA, is formed on the surface (Steigerwald et al 1997), but the characteristics of this layer are not studied. These three different types of slurry have been chosen to investigate the characteristics of soft layers formed.

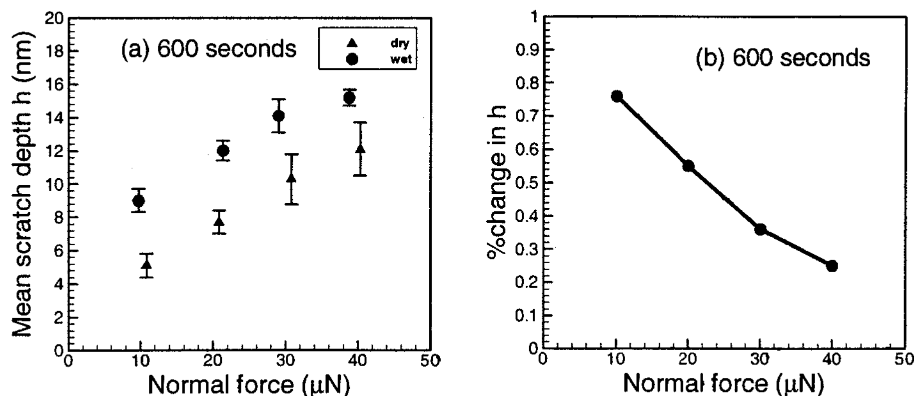

Fig 3.6 (a) Variation of mean scratch depth with nominal normal force (b) Percent change in mean scratch depth at certain nominal normal force (600s).

A. 0.6wt% NH_4OH slurry

It is expected that chemical product layer formed due to chemical reaction should grow with exposure time. Accordingly, 90s, 300s and 600s of chemical exposure time are selected to form the soft layer with different layer thickness but similar material property. The experimental results for dry scratch test and wet scratch test with 600s exposure time are shown in Fig 3.6 and Fig 3.7, from which normal force, tangential force and mean scratch

depth can be found.

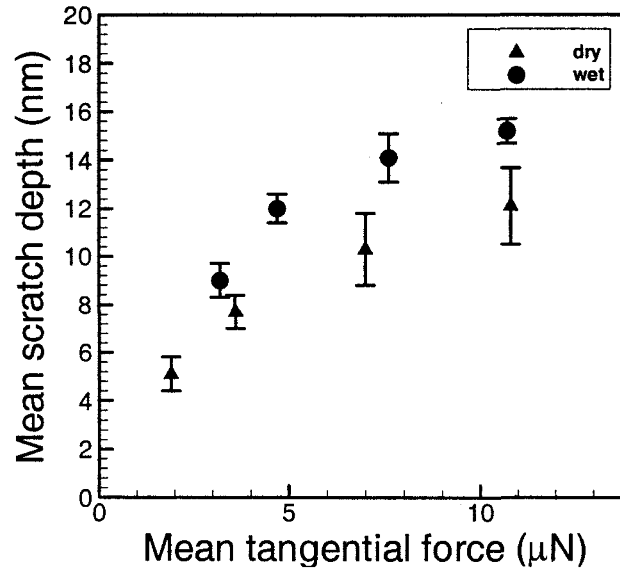

Fig 3.7 Variation of mean scratch depth with mean tangential force (600s).

Fig 3.6(a) shows the variation of mean scratch depth with normal force for both dry and wet conditions, where dry scratch depth ranges from 5 to12nm and wet scratch depth ranges from 9nm to 15nm. The "dry" test refers the scratch tests on copper surface without chemical exposure, and the "wet" test refers the scratch tests on chemically exposed surfaces. The experimental results (symbols in Fig 3.6 and Fig 3.7) are an average of 4 data points with the error bars representing the data range. As expected, the mean scratch depth for wet condition is higher than that for dry condition at certain normal force, which is the evidence of a soft layer formation on the surface during chemical exposure. Fig 3.6(b) shows the percent change in mean scratch depth between dry and wet tests with normal force, as expected, a decreasing trend is observed. It shows that the difference of mean scratch depth between dry

and wet tests is large at small normal force (or small scratch depth), and small at large normal force (or large scratch depth). If the normal force (or scratch depth) is large enough, it is expected that the difference between them will saturate. It can be concluded that for CMP process, given an applied normal pressure, the smaller the scratch depth under wet condition, the more efficient polishing we would have compared to dry polishing process.

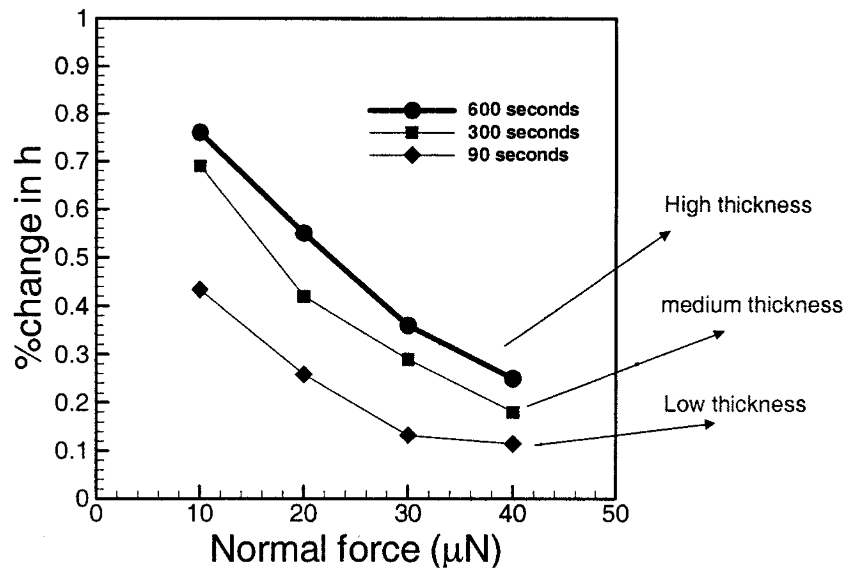

Fig 3.8 Comparison between different chemical exposure times

Fig 3.7 shows the variation of mean scratch depth with mean tangential force for 600s chemical exposure time. At the same tangential force, the wet scratch depth is higher than the dry scratch depth, showing that a softened layer exists under wet conditions. Similarly at the same scratch depth (meaning that the material ahead of the indenter tip is same for both dry and wet conditions), as expected, the tangential force for material under wet conditions is smaller than that for material under dry conditions. So a soft layer is formed on the surface

when ammonium hydroxide is present on the surface of copper.

Fig 3.8 shows the percent change in mean scratch depth between dry and wet tests with normal force for 90s, 300s and 600s. The same decreasing trends with different amplitude are observed for different chemical exposure times. At lower normal force (lower scratch depth), 10μN, the difference in mean scratch depth between dry and wet tests ranges from ~40% to ~80%, where 600s test yields highest difference and 90s test yields lowest difference. At higher normal force (higher scratch depth), 40μN, the difference in mean scratch depth between dry and wet tests ranges from ~10% to ~30%, where 600s test yields highest difference and 90s test yields lowest difference. So the experimental data not only show the soft layer formation on top of the reference surface for all these three tests, but also shows qualitatively that soft layer formed with 600s chemical exposure time is thickest, and soft layer formed with 90s chemical exposure time is thinnest.

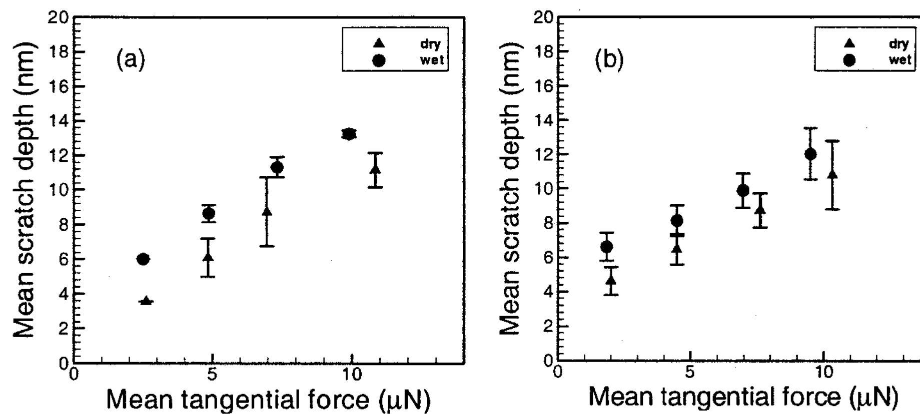

Fig 3.9 Variation of mean scratch depth with mean tangential force (a) 300s (b) 90s.

Fig 3.9 shows mean scratch depth between dry and wet tests with tangential force for

scratch tests under 90s and 300s chemical exposure time. The mean scratch depth under wet tests is higher than that in dry test. These are also the evidence of soft layer formation on the surface when chemicals are present for 90s and 300s tests.

The experimental results of scratch test for 0.6wt% NH_4OH slurry show a soft layer formation when surface is exposed to the slurry chemicals. The characteristics of the soft layers formed in this slurry will be analyzed in section 3.4.

B. 5wt% H_2O_2 slurry

This slurry is selected to form the similar type of surface layer (copper oxide), but different layer thickness. So the experimental results from this slurry can be used to compare to the experimental results from 0.6wt% NH_4OH.

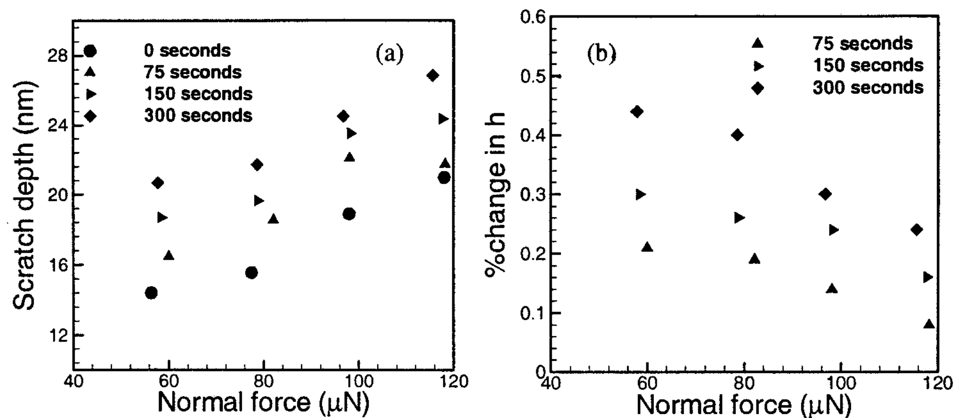

Fig 3.10 (a) Variation of mean scratch depth with nominal normal force (error bar is not shown) (b) Percent change in mean scratch depth at certain nominal normal force (5wt% H_2O_2)

Fig 3.10(a) shows the variation of mean scratch depth with normal force for 0s, 75s, 150s and 300s chemical exposure time. The error bars for the experimental data are not

shown for the clarity of the figure. The percent change in mean scratch depth between dry and wet tests with normal force are shown Fig 3.10(b). As described for Fig 3.8, the similar decreasing trends with different amplitude are observed for different chemical exposure times. It can also be qualitatively concluded that a soft layer formed on the surface, and the thickness of soft layer grows with chemical exposure time based on the experimental results for slurry 5wt% H_2O_2.

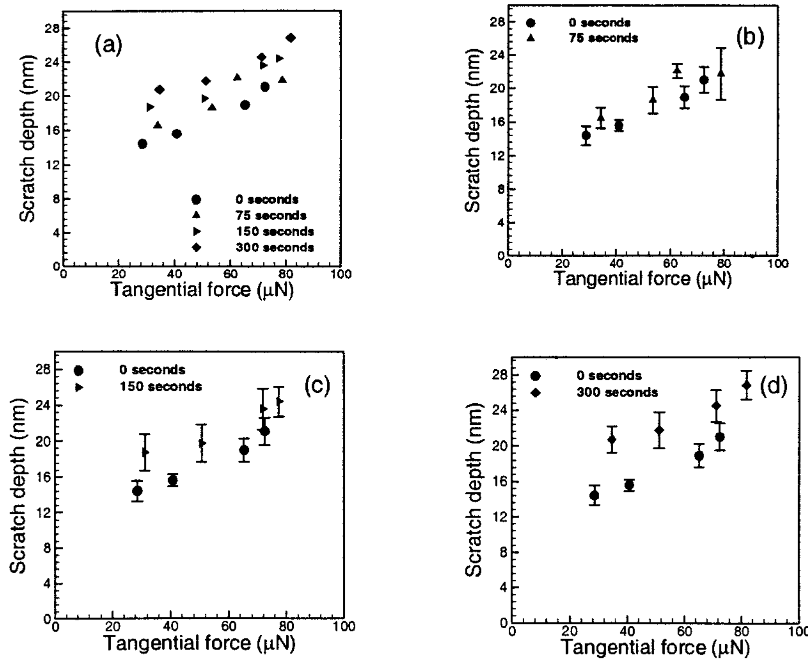

Fig 3.11 Variation of mean scratch depth with mean tangential force (5wt% H_2O_2).

The experimental results for the variation of mean scratch depth with mean tangential force for 0s, 75s, 150s and 300s chemical exposure time are shown in Fig 3.11 (a). The experimental data for them with the error bar are in shown in Fig 3.11(b, c d). For all these wet tests, the mean wet scratch depth is higher than that in dry test. These are the additional

evidence of soft layer formation on the surface.

The characteristics of the soft layers formed in 5wt% H_2O_2 will also be addressed in section 3.4.

C. 1.0wt% HNO_3+ 0.5wt% BTA

This slurry will form a non-native surface layer (Cu-BTA) after it is exposed to copper surface. This Cu-BTA film acts as an inhibitor to protect the subsurface from further chemical dissolution. Such inhibitor layer may have different mechanical properties and thickness based on the utilized slurry. An exposure time of 600s is picked to find out the layer thickness and property for this type of surface layer.

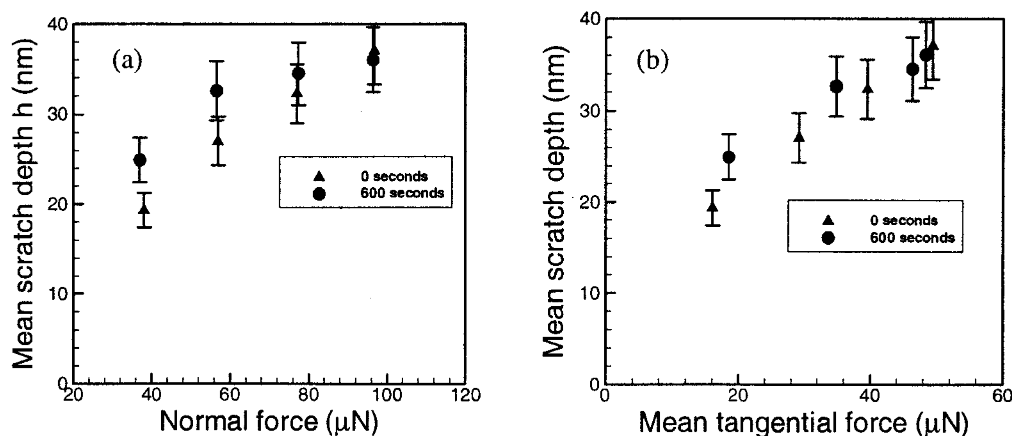

Fig 3.12 (a) Variation of mean scratch depth with nominal normal force, (b) Variation of mean scratch depth with mean tangential force (600s exposure by 1.0wt% HNO_3+ 0.5wt% BTA).

The experimental results are shown in Fig 3.12. Fig 3.12(a) shows the variation of mean scratch depth with nominal normal force, where wet scratch depth is larger than the dry scratch depth at same normal force. Fig 3.12(b) shows variation of mean scratch depth with mean tangential force, where wet scratch depth is larger than the dry scratch depth at same

tangential force. The selected testing normal force reaches the saturation range, since little difference between dry ant wet tests is observed for data with normal force 80μN and 100μN, meaning that the soft layer effect diminished as the scratch depth is much larger than the layer thickness.

The experimental results show soft layer formation when copper surface is dipped into the slurry. The characteristics of the soft layers formed in 1.0wt% HNO_3+ 0.5wt% BTA will be described in section 3.4.

3.4 Analytical Model for Scratch

The intent of this work is to understand the characteristics of the soft layer formed on the copper surface due to chemical dissolution. Following the approach by Fu et al (2001), a simple model is developed to estimate the thickness of the soft layer and the mean contact pressure of soft layer by comparing to the substrate property.

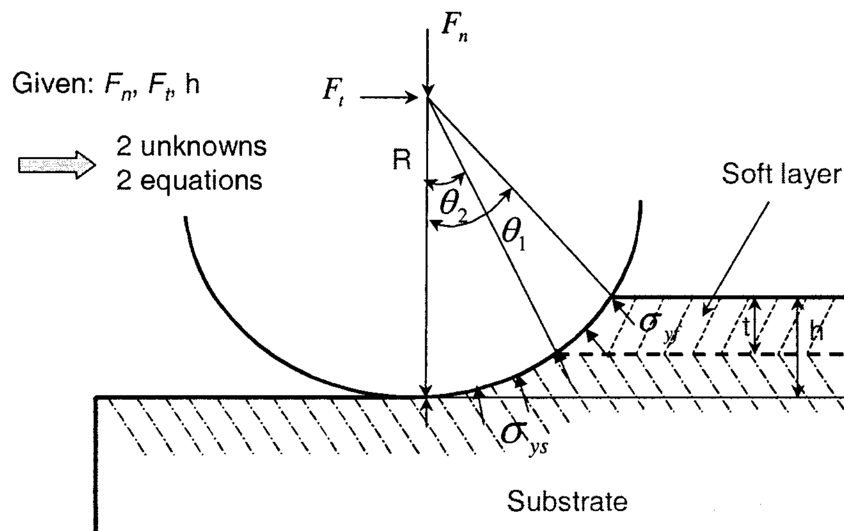

Fig 3.13 Schematic of abrasive particle-workpiece contact.

Neglecting the pile-up before the abrasive particle during plowing action, and assuming a frictionless spherical particle-workpiece interface, based on force equilibrium, forces on an individual abrasive particle can be expressed (referring to Fig 3.13) as

$$F_n = \int_0^{\pi}\int_0^{\theta_2} \sigma_{ys} \cos(\theta) R^2 \sin(\theta) d\theta d\varphi + \int_0^{\pi}\int_{\theta_2}^{\theta_1} \sigma_{yf} \cos(\theta) R^2 \sin(\theta) d\theta d\varphi$$

3.1(a)

$$F_t = \int_0^{\pi}\int_0^{\theta_2} \sigma_{ys} \sin(\theta)\sin(\varphi) R^2 \sin(\theta) d\theta d\varphi + \int_0^{\pi}\int_{\theta_2}^{\theta_1} \sigma_{yf} \sin(\theta)\sin(\varphi) R^2 \sin(\theta) d\theta d\varphi$$

3.1(b)

where θ_1 and θ_2 are the angle of contact as shown in Fig 3.13, σ_{yf} is the mean contact pressure of soft layer, σ_{ys} is the substrate mean contact pressure.

Assuming the angle of contact to be small, since the diameter of abrasive particle is much larger than the indentation depth, we have

$$F_n \approx \pi\sigma_{ys} R(h-t) + \pi\sigma_{yf} Rt \qquad 3.2(a)$$

$$F_t \approx \frac{4\sqrt{2}}{3}\sigma_{ys} R^{1/2}(h-t)^{3/2} + \frac{4\sqrt{2}}{3}\sigma_{yf} R^{1/2}\left[h^{3/2} - (h-t)^{3/2}\right] \qquad 3.2(b)$$

There are two unknown variables in the above two equations (3.2(a) and 3.2(b)), soft layer thickness *t*, and mean contact pressure of soft layer, σ_{yf}. The normal force, tangential force, indentation depth are given by the experimental scratch data under wet condition, which is given in appendix 1. The substrate mean contact pressure under scratch is estimated when the film thickness is 0 based on Eq. 3.2(a) and 3.2(b) by using the scratch data in the dry condition. The radius of the indenter is obtained by scanning the indenter tip on a calibration grating with a tip radius less than 10nm and tip angle less than 30 degree (tip

radius data are in the appendix 2). The film thickness and mean contact pressure are solved by iterative method. First, a reasonable film thickness is assumed, and put into Eq. 3.2 (b), and then film mean contact pressure solved by Eq. 3.2 (b) is put into Eq. 3.2 (a) and solve for the new film thickness. The actual film thickness is obtained when the solution is converged.

3.4.1 Results for 0.6wt% NH_4OH slurry

Based on the experimental data and 3D model describe above, the characteristics of soft layer formed in 0.6wt% NH_4OH are shown in Table 3.1 (detailed data are in appendix 1). The soft layer thickness is about 7.3 nm for 600s chemical exposure time, about 5.7 nm for 300s exposure time, and about 5.0 nm for 90s chemical exposure time. The average ratio of the film mean contact pressure to substrate mean contact pressure is about 0.45 to 0.52 based on three data sets. By assuming that the chemical product layers formed under different chemical exposure time are similar in material properties, the current method predicts approximately same mean contact pressure for the soft layers formed under different chemical exposure time, and the chemical product layer grows with chemical exposure time.

Table 3.1 Experimental result for 0.6wt% NH_4OH

Exposure time (s)	90	300	600
Film thickness (nm)	5.0 ± 0.2	5.7 ± 0.6	7.3 ± 0.8
$\sigma_{yf} / \sigma_{ys}$	~0.52	~0.48	~0.45

To verify the film thickness measurement from our model, X-ray photo-electron spectroscopy (XPS) was used to estimate the film thickness for soft layer formed by 0.6wt% NH_4OH at 90s, 300s and 600s exposure time. Following the method by Chawla et al (1992),

angle resolved XPS was used to model the thickness, structure and composition of the film. The experimental XPS signal intensity ratio for 90s, 300s and 600s chemical exposure time are shown in Fig 3.14. Chawla et al used a two-layer model. The 1st layer is hydroxyl and bound water, and the 2nd layer is cuprite, Cu_2O. In order to follow their method, we used the same two-layer model to calculate the thickness of those two layers. Then we assume that the two layers have the same material properties and use the overall thickness to compare to the thickness of our single-layer nano-scratch model. To reduce the effect of surface roughness on photo-electron angular distribution (Fadley et al, 1974), only high angle data (80 degree) are used to fit their equations. The calculated results are shown in table 2.

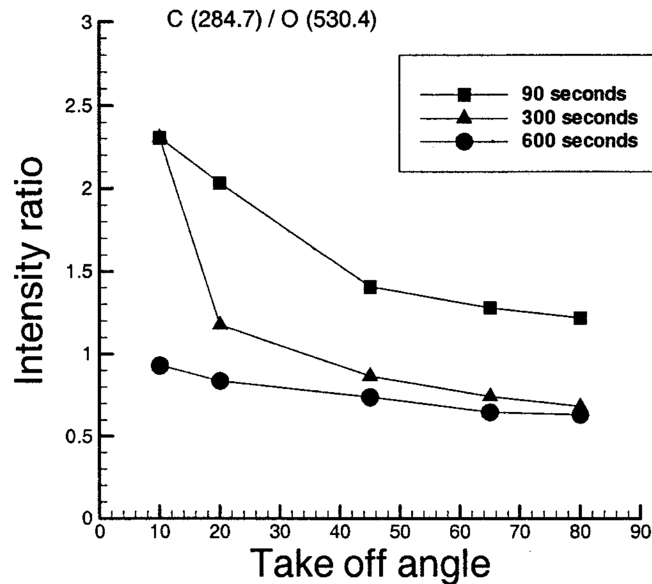

Fig 3.14 XPS signal intensity ratio with take of angle from Cu surface

From comparisons between table 3.1 and table 3.2, we can see that the thickness measurements of these two techniques are very close to each other, which confirms that our new developed technique is reliable.

Table 3.2 XPS result for 0.6wt% NH_4OH.

Chemical exposure time (s)	90	300	600
1st Layer thickness (nm)	0.8	0.6	0.5
2nd Layer thickness (nm)	4.0	5.2	6.6
Overall layer thickness (nm)	4.8	5.8	7.1

3.4.2 Results for 5wt% H_2O_2 slurry

The characteristics of soft layer formed in 5wt% H_2O_2 are shown in table 3.3 (detailed data in appendix 1). The soft layer thickness is about 16.8 nm for 300s chemical exposure time, about 13.2 nm for 150s chemical exposure time, and about 9.8 nm for 75s chemical exposure time. The average ratio of the film mean contact pressure to substrate mean contact pressure is about 0.63 to 0.69 based on three data sets. By assuming that the chemical product layers formed under different chemical exposure time are similar in material properties, the current method predicts approximately the same mean contact pressure for the soft layers formed under different chemical exposure time, and the chemical product layer grows with exposure time nearly linearly.

Table 3.3 Experimental result for 5wt% H_2O_2 slurry

Chemical exposure time (s)	75	150	300
Film thickness (nm)	9.8 ± 0.4	13.2 ± 0.8	16.8 ± 1.0
$\sigma_{yf} / \sigma_{ys}$	~0.69	~0.65	~0.63

From the XPS investigation, the copper surface can be modeled as a bi-layer structure

described by Chawla et al (1992). The 1st layer is hydroxyl and bound water, which is less than 1 nm, and the 2nd layer is cuprite. It is reasonable to assume that the 1st layer is much softer than the second layer. This bi-layer structure can be used to explain the difference in the mean contact pressure ratio between table 3.1 and table 3.3. It has been observed by many researchers (Steigerwald et al 1995, Nishizawa et al 2004) that cuprite, Cu_2O is going to form on the copper surface exposed to ammonium hydroxide and hydrogen peroxide. CuO may also form on the surface exposed to hydrogen peroxide (Nishizawa et al 2004). If we model the surface layers same as Chawla et al (1992). Then it is expected that the mean contact pressure ratio in table 3.3 should be a little higher than that in table 3.1), because the oxide layer formed in hydrogen peroxide is thicker, and the percentage of that hydroxyl layer in the overall surface layer is expected to be lower. The other reason could be the difference in material mechanical properties between Cu_2O and CuO, since the chemical product layers formed by this two slurry may not be exactly same.

3.4.3 Results for 1.0wt% HNO_3+ 0.5wt% BTA slurry

The characteristics of soft layer formed in 1.0wt% HNO_3+ 0.5wt% BTA are shown in table 3.4 (detailed data in appendix). The soft layer thickness is about 7.6 nm for 600s chemical exposure time. The average ratio of the film mean contact pressure to substrate mean contact pressure is about 0.2, since BTA is a polymer material. It is reasonable for Cu-BTA to have much lower mean contact pressure than copper substrate.

The thin film characterization technique developed here assumes a single layer on the substrate. It is applied to the following materials: copper oxide on copper and Cu-BTA on copper. The current method predicts approximately same mean contact pressure for the soft

layers formed under different chemical exposure time, and also chemical product layer grows nearly linearly with chemical exposure time as shown in table 3.1 and table 3.3. The mean contact pressure of non-native copper film, Cu-BTA, is much lower than that of copper oxide, which is in a reasonable range. The thickness measurement results between the XPS measurement and our nano-mechanical testing technique are very close to each other, which also indicts our technique is reliable for the current testing configuration.

Table 3.4 Experimental result for 1.0wt% HNO_3+ 0.5wt% BTA

Chemical exposure time (s)	600
Film thickness (nm)	7.6
$\sigma_{yf} / \sigma_{ys}$	0.2

3.5 Continuous Stiffness Measurement

As the research and development progresses to the nanoscale, macroscale characterization techniques are no longer sufficient for the demanding materials research required for many applications. Nano-mechanical characterization techniques have become the standard for gaining understanding of material behavior at the nanoscale and have been utilized for thin film, as well as bulk material analysis. However, the standard analysis techniques assume elastic-plastic material behavior and have many shortcomings for viscoelastic materials. (http://www.hysitron.com).

Compared to quasi-static indentation test, the dynamic testing technique can obtain much more information about the sample. It is primarily used to get the mechanical properties for materials display significant time dependent deformation and recovery,

however, it can also be used to get the variation of material properties with indentation depth.

3.5.1 Experimental procedure

Nano DMA test is done by the Hysitron nano-indenter. The testing procedure is elaborated below, which is designed to find out the modulus variation with the indentation depth for chemical etched copper.

1) Prepare the sample as described in section 3.2.
2) Start the nano-indenter following nano-DMA test procedures.
3) Calibration of electrostatic force constant calibration and dynamic constants.
4) Set up the desired dynamic load function.
5) Scan the surface before indentation.
6) Run dynamic indentation on copper surface at dry conditions (without chemical exposure). Repeat for more than 3 times.
7) After dry test, the copper is exposed to 0.6wt% NH_4OH for 90s chemical exposure time (300s and 600s of chemical exposure time are also done). Then the surface is carefully dried.
8) Run dynamic indentation on copper surface at wet conditions (with chemical exposure). Repeat tests for more than 3 times.

3.5.2 Dynamic load function

In a nano-DMA test, there are three user-defined parameters, quasistatic load, dynamic load amplitude and dynamic frequency. Usually one of the above three parameters is changed. For example, if only the dynamic frequency is changed, it is termed as ramping dynamic frequency test. In this test, the quasistatic load and dynamic load amplitude is fixed. If the

quasistatic load is varied in each progressive step, it is termed as ramping quasistatic load. During this test, the dynamic frequency is fixed, and the dynamic load can be held constant or varied with the quasistatic load. For our purpose, the dynamic load function is set as ramping quasi-static load while dynamic load is fixed percent of quasistatic load. A typical quasi-static with fixed percent dynamic load function is shown in Fig 3.15.

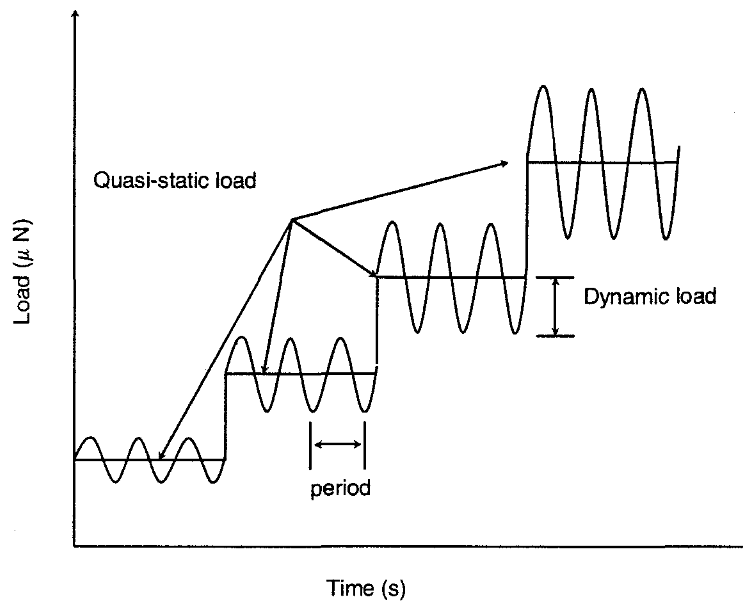

Fig 3.15 Schematic for ramping quasi-static load.

During this load function, the quasi-static load is changed in each progressive step. In each step, a fixed percent of quasi-static load is picked as dynamic load. A fixed frequency is also chosen for every step. For the current test, the quasi-static load is ramped from 10μN to 100μN with 10 steps, and frequency is 10Hz. The dynamic load is 50% of the quasi-static load.

3.5.3 Experimental results

The experiments results for nano DMA test with 0s, 90s, 300s and 600s chemical exposure time are shown in Fig 3.16. Fig 3.16 (a) shows the variation of measured modulus normalized by the substrate modulus with indentation depth for dry condition (0s chemical exposure time). A constant modulus is observed for the range of tested indentation depth with certain scatter of the data. Fig 3.16 (b), (c) and (d) shows the variation of measured modulus normalized by the substrate modulus with indentation depth for wet condition (90s, 300s and 600s chemical exposure time).

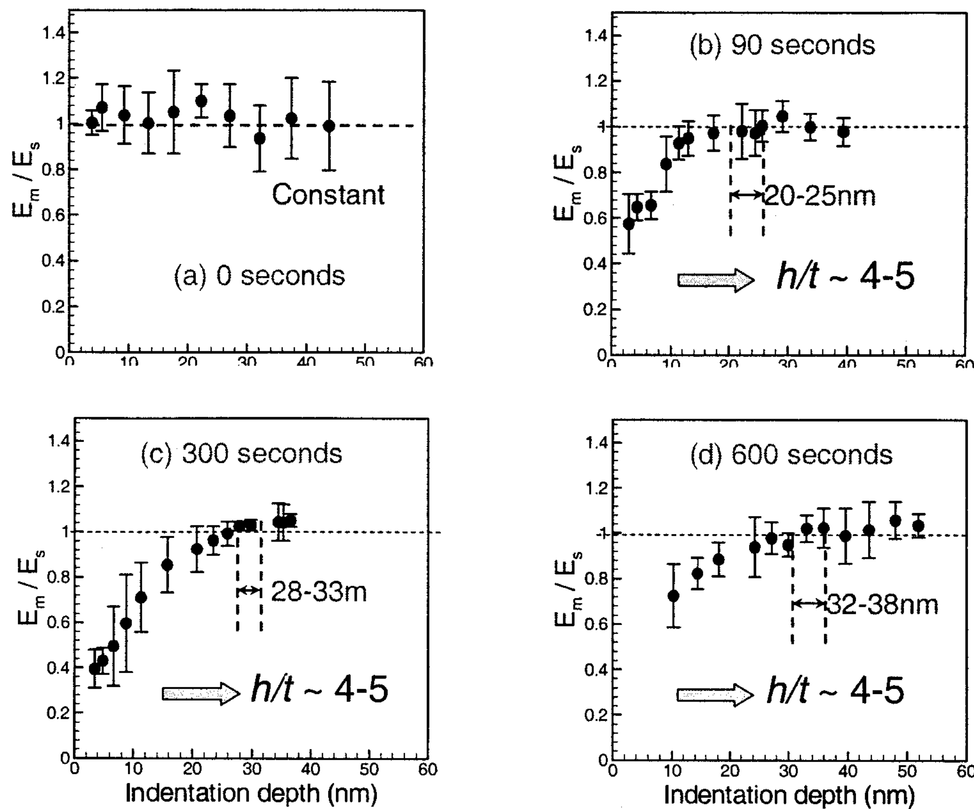

Fig 3. 16 Variation of measured modulus normalized by substrate modulus with indentation depth (a) 0s, (b) 90s, (c) 300s, (d) 600s.

An increasing trend is observed for the range of indentation depth tested, which is similar to the trend shown in the experiments done by Saha and Nix (2002) for soft layer on hard substrate. For 90s of chemical exposure time, at 15-20nm indentation depth, the measured modulus is approximately the substrate modulus. For 300s of chemical exposure time, at 25-30nm indentation depth, the measured modulus equals to the substrate modulus. For 600s of chemical exposure time, the experimental data saturates at about 35nm indentation depth. In Saha and Nix's experiment, the indentation depth doesn't exceed 2 times the layer thickness. When the ratio of film modulus to substrate modulus is about 1/6, no saturation is observed at indentation depth equal to two times film thickness. Based on the film thickness analysis in section 3.4, when the indentation depth is in the order of ~5 times the film thickness, the measured modulus is the substrate modulus as shown in the DMA experimental results. However, the ratio of film modulus to substrate modulus is still unknown. This ratio is deconvoluted by FEM simulation described in section 3.6.

3.6 Numerical Simulation for Single-Layer Structure

The intent of this work is to understand the characteristics of the soft layer formed on the copper surface due to chemical dissolution. The film thickness and the yield strength estimated based on the nano-scratch are used as an input to FEM model.

The modulus of the soft layer can be deduced by the nano DMA test combined with the FEM simulation. Following the approach of Chen and Vlasak (2001), indentation of a film-substrate structure is examined by FEM simulation using ABAQUS/Standard. The implemented axisymmetric model is shown in Fig. 3.17 (a). The abrasive particle is assumed rigid while the ploughed substrate has material parameters consistent to those of copper

(E=126GPa, σ_y=70MPa, σ_{ult}=220MPa). The film yield strength is taken to be 45% of the substrate yield strength. The film modulus is varied from 0.1 to 1 of the substrate modulus. An isotropic elastoplastic strain hardening material model is used with hardening exponent n=0.2 for both substrate and film. Since poisson's ratio is a minor factor for static indentation (Mesarovic and Fleck 2000), we take poisson's ratio to be 0.33 for both film and substrate. No friction is considered between the particle and the film, since it is also a minor factor (Mesarovic and Fleck 2000). For a typical axisymmetric indentation, the mesh contains about 20000 4-node elements. The mesh of the model is shown in Fig 3.18.

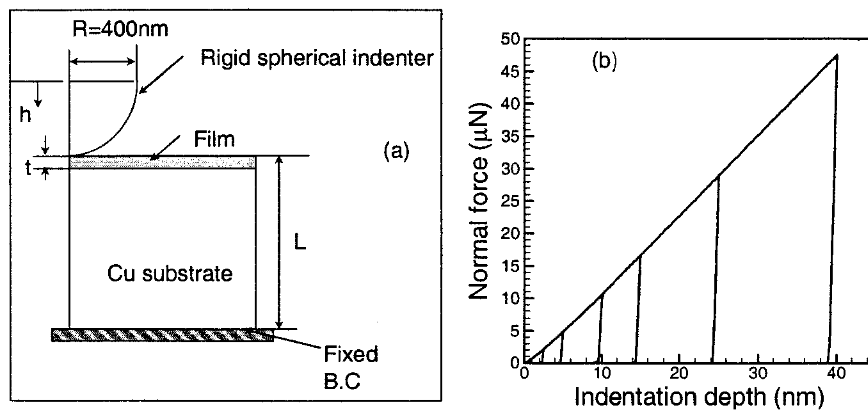

Fig 3. 17 (a) model description for axisymmetric indentation on film-substrate structure, (b) Force displacement curve showing simulation procedure.

Since elastic modulus at certain indentation depth is the interest, a series loading and unloading steps are performed for each simulation. The simulation procedure is shown in Fig 3.17 (b) for each case. There are 7 steps for each case. The largest indentation depth is chosen such that the indentation depth is 8 times the film thickness. The stiffness of the structure at certain indentation depth can be calculated based on the unloading curve, and

then modulus at that indentation depth is calculated based on equation

$$E = \frac{\sqrt{\pi} S}{2\beta\sqrt{A}} \tag{3.3}$$

Where β is a constant and depends on tip geometry. For spherical indenter, β is 1. A is the current contact area, and S is the contact stiffness.

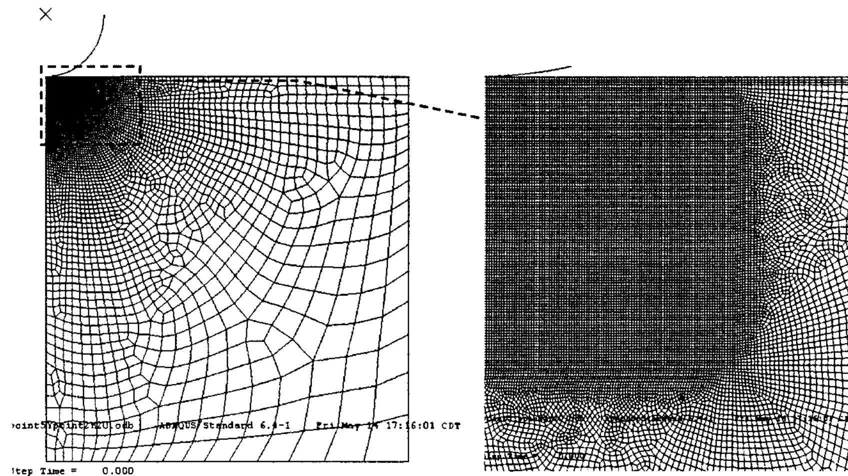

Fig 3.18 Mesh for the model

Based on the nano-scratch test and the model, the film thickness is estimated. Combined with the nano DMA test, the measured modulus approaches the substrate modulus when the ratio of indentation depth to film thickness is about 5 for different chemical exposure time (different layer thickness).

Fig 3.19 shows the result of the FEM simulation. When E_f/E_s is about 0.5, the measured modulus reaches the substrate modulus when h/t is about 2. When E_f/E_s is about 0.2, the measured modulus reaches the substrate modulus when h/t is about 5. When E_f/E_s is about

0.1, the measured modulus doesn't reaches the substrate modulus when *h/t* is about 8.So DMA test coupled with FEM simulation shows that the modulus of soft layer is about 20% of the modulus of the substrate.

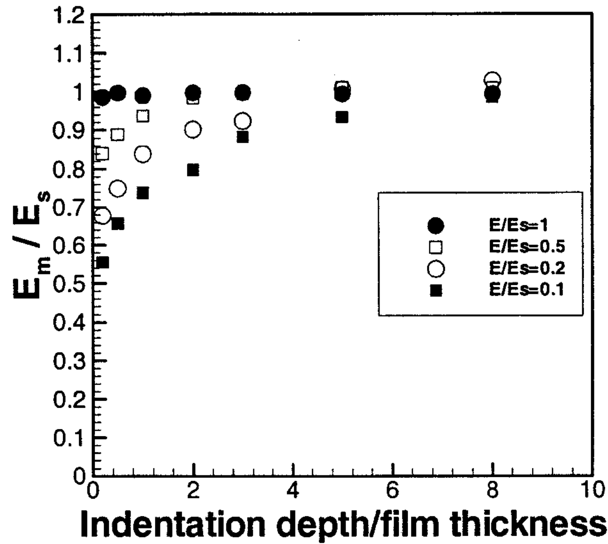

Fig 3.19 Normalized modulus with normalized indentation depth *h/t*.

3.7 Conclusions

Both experimental and modeling techniques have been used to explore the synergistic effect of chemical dissolution and mechanical abrasion during chemical mechanical planarization of copper. For our testing configuration, the properties of the soft layer formed on the copper surface due to chemical dissolution (three different slurries) are identified. The thickness of the soft layer grows with the exposure time and the yield strength of the soft layer is about 50% of that of the substrate for copper oxide. For non native copper film, Cu-BTA, the yield strength of the soft layer is about 20% of that of the substrate Utilizing data (ammonium hydroxide only) from nano-DMA tests coupled with the FEM simulation of a

film-substrate structure, the elastic modulus of the soft layer is about 20% of that of the substrate. It is also shown from the nano scratch experiment that the chemical softening will enhance the mechanical abrasion by as much as 70% for a fixed normal force at low cutting depth, and the softening effect on scratch depth is reduced at high cutting depth.

When the film thickness is small compared to indentation depth, the conventional indentation technique cannot be used and also when the other techniques (such XPS or ellipsometry) are difficult to apply, this method can be taken as nano-mechanical thin film characterization technique. It is noteworthy that this is a new technique to characterize the ultra thin film from the view of mechanics, and the experimental process is simple. Based on the technique discussed here, not only the thickness of the film, but also the elastic modulus and the hardness of the film can be measured.

3.8 References

1. ABAQUS User Manuals, Ver. 6.3.1, Hibbitt Karlsson and Sorensen Inc., Providence, RI, 2003.
2. Bastawros, A.-F., Chandra, A., Guo, Y., and Yan, B., Pad effects on material removal rate in chemical mechanical planarization, Journal of Electronic Materials, Vol. 31, No. 10 SPEC., pp 1022-1031, October 2002.
3. Brown, N.J., Some speculations on the mechanisms of abrasive grinding and polishing, Precision Engineering, Vol. 9, No. 3, pp 129-138, 1987.
4. Carpio, R., Farkas, J., and Jairath, R., Initial study on copper CMP slurry chemistries, Thin Solid Films, Vol. 266, No. 2, pp 238-244, Oct 1995.
5. Chandra, A., Profile rolling of gears: a boundary element analysis, J. Eng. Ind., ASME,

Vol. 111, pp 48-55, 1989.

6. Chawla, S. K., Rickett, B. I., Sankarraman, N.and Payer, J. H., An X-ray photo-electron spectroscopic investigation of the air-formed film on copper, Corrosion Science, Vol. 33, No. 10, pp 1617-1631, 1992.

7. Che, W., Guo, Y. Chandra, A. and Bastawros, A.-F, Mechanistic understanding of material detachment during micro-scale polishing, Journal of Manufacturing Science and Engineering, Transactions of the ASME, Vol. 125, No. 4, pp 731-735, 2003.

8. Chen, X. and Vlasak, J., Numerical study on the measurement of thin film mechanical properties by means of nanoindentation, Journal of Materials Research, Vol. 16, No. 10, pp 2974-2982, October 2001.

9. Fadley, C. S., Baird, R. J., Sickhaus, V., Novakov, T. and Bergstrom, S. A. L., Surface analysis and angular distributions in x-ray photoelectron spectroscopy, Journal of Electron Spectroscopy and Related Phenomena, Vol. 4, pp 93-137, 1974

10 Fu, G., Chandra, A., Guha, S. and Subhash, G., A plasticity based model of material removal in chemical mechanical Polishing (CMP), IEEE Trans. Semiconductor. MFG., Vol. 14, No. 4, pp 406-417, 2001.

11. Gahlin, R., Axen, A. and Jacobson, S., The influence of tip shape in abrasion studied by controlled multiasperity surfaces, Wear, Vol. 223, pp 150-156, 1998.

12. Gignac, L.M., Rodbell, K.P., Cabral, C., Jr., Andricacos, P.C., Rice, P.M., Beyers, R.B., Locke, P.S. and Klepeis, S.J., Characterization of plated Cu thin film microstructures, Materials Research Society Symposium - Proceedings, Vol. 562, pp 209-214, 1999.

13. Hokkirigawa, K. and Kato, K., Experimental and theoretical investigation of ploughing, cutting and wedge formation during abrasive wear, Tribology International, Vol. 21, pp

151-157, 1988.

14. Kaufman, F.B., Thompson, D.B., Broadie, R.E., Guthrie, W.L., Pearson, D.J., and Small, M.B., Chemical-mechanical polishing for fabricating patterned W metal features as chip interconnects, Journal of the Electrochemical Society, Vol. 138, No. 11, pp 3460-3465, Nov 1991.

15. Kuehn, J., Particle scale and wafer scale effects in Chemical and Mechanical Planarization (CMP), MS Thesis, Dept of Mechanical Engineering and Engineering Mechanics, Michigan Technological University, 2000.

16. Lange, K. and Kurz, N., Theoretical and experimental investigation of the "Groz" cold shape-rolling process, Inst. for Metal Forming Report, University of Stuttgart, Germany, 1984.

17. Luo, J. and Dornfeld, D.A., Material removal mechanism in chemical mechanical polishing: theory and modeling, IEEE Trans. Semiconductor. MFG., Vol. 14, No. 2, pp 112-133, 2001.

18. Luo, W., Campbell, D.R. and Babu, S.V., Chemical-mechanical polishing of copper in alkaline media, Thin Solid Films, Vol. 311, No. 1-2, pp 177-182, Dec 1997,

19. Mesarovic, S.D. and Fleck, N.A., Frictionless indentation of dissimilar elastic-plastic spheres, International Journal of Solids and Structures, Vol. 37, No. 46, pp 7071-7091, Nov 2000.

20. Nishizawa, H.; Tateyama, Y.; Saitoh, T, Ellipsometry characterization of oxidized copper layers for chemical mechanical polishing process, Thin Solid Films, Vol. 455-456, pp 491-494, May 1, 2004.

21. Saha, R. and Nix, W.D. Effects of the substrate on the determination of thin film

mechanical properties by nanoindentation, Acta Materialia, Vol. 50, No. 1, pp 23-38, Jan 2002.

22. Seok, J., Sukam, C. P., Kim, A. T., Tichy, J. A. and Cale, T. S., Multiscale material removal modeling of chemical mechanical polishing, Wear, Vol. 254, pp. 307-320, 2003.
23. Shaw, M.C., Metal Cutting Principles, Clarendon Press, Oxford, 1984.
24. Singh, R.K., Lee, S.M., Choi, K.S., Basim, G.B., Choi, W., Chen, Z. and Moudgil, B.M., Fundamentals of slurry design for CMP of metal and dielectric materials, MRS Bulletin, Vol. 27, No. 10, pp 752-760+748 , October, 2002.
25. Steigerwald, J.M., Murarka, S.P., Gutmann, R.J, Duquette, D.J., Chemical processes in the chemical mechanical polishing of copper, Materials Chemistry and Physics, Vol. 41, No. 3, pp 217, Aug 1995.
26. Steigerwald, J.M., Murarka, S.P., Gutmann, R.J, “copper CMP”, Chemical mechanical planarization of microelectronic materials, New York: J. Wiley, 1997.
27. Tomozawa, M., Oxide CMP mechanisms, Solid State Tech., Vol. 40, No. 7, pp 169-175, 1997.
28. Xie, Y, and Williams, J. A., The generation of worn surfaces by the repeated interaction of parallel grooves, Wear, Vol. 162-164, pp 864-872, 1993.
29 Weisenberger, L.M. and DurKin, B.J., Copper Plating, Electroplating, pp 167-175, McGraw-Hill, 1978.
30. Zhao, X. and Bhushan, B., Material removal mechanisms of single crystal silicon on nanoscale and ultra-low loads, Wear, Vol. 223, pp. 66-78, 1998.

Chapter 4 Material Removal Mechanism Part II: Mechanically Assisted Chemical Dissolution by Introducing Residual Stress in the Sub Surface through Wear Test

4.1 Literature Review

During traditional optical glass polishing, the material removal mechanisms that have been proposed over the years can be categorized as mechanical wear, plastic flow, chemical dissolution, and mechanical abrasion of chemically soften layer (Izumitani, 1979). It has been founded by Cook (1990) and Nogami et al (1984) that water would diffuse into silica surface as a function of uniaxial stress and hydrostatic pressure. The diffusion coefficient increased exponentially with increasing tensile stress and decreased exponentially with increasing compressive stress and hydrostatic pressure. However, the solubility of silica in water showed an opposite trend. Nogami et al (1984) showed that the diffusion depth of water into silica ranges from 0.5 to 12nm depending on particles diameter and local pressure. Cook et al (1987) obtained a layer depth of about 17nm for BK-7 optical borosilicate glass. The hydrated layer, $Si(OH)_4$, has a weaker mechanical strength compared to SiO_2, since the Si-O bond is stronger than Si-OH bond. Thus, the stress enhanced diffusion should increase material removal rate for oxide CMP.

Stress is well known to induce corrosion cracking in metal alloys. Chang et al (2001) investigated the notch formation during over-etching of poly-silicon. It was shown by their experiment that the compressive stress can retard notching because of the reduced rate of spontaneous etching of poly-silicon, and the tensile stress enhance notching indicating stress

enhanced etching. Vyvoda and Graves (1998) predicted stress-enhanced etching in the area close to the poly-silicon-gate oxide interface, by assuming a local etch rate proportional to the normal component of the surface strain energy density gradient. Although the stress enhanced etching occurs in the above case, a question remains if the same trend can be extended to the Cu CMP process? We will attempt to reach an answer in this chapter.

A nominally flat surface of an elastically stressed body is unstable with respect to the growth of perturbations with wavelengths greater than a critical wavelength (Srolovitz, 1989). For a solid constrained in one dimension and subject to a uniform dilatation, this wavelength scales as $\gamma E/\sigma^2$, where γ is the surface energy, E is Young's modulus, and σ is the nominal stress associated with the constrained dilatation. It has also been reported that for a flat surface with residual stress, the surface roughness with different spatial wavelength decays differently under chemical etching. Kim et al (1999) scanned the surface profiles of a stressed solid before and after etching, and they showed surface roughness with wavelength larger than a critical wavelength will grow, and surface roughness with wavelength smaller than a critical wavelength will decay. The critical wavelength in their model is also a function of the stress in the solid, elastic modulus and interfacial energy. They claimed that the difference between two profiles could be used to identify the stress state of the solid if the interfacial energy is known. This technique was verified with an aluminum alloy etched with Keller reagent. This phenomenon was also modeled by Yu et al (1999) by using a linear perturbation analysis. They showed that the effect of stress on surface reaction by changing either driving force (quadratic effect) or the mobility (linear effect). Both effects caused the surface roughness evolution with time. At near equilibrium state, the roughness change was mainly caused by quadratic stress effect. At far from equilibrium, it is caused by linear stress

effect. The surface roughness spectra for near and far from equilibrium are developed, which can be used as fingerprints to identify the stress state in the solid. For the nano wear tests we are conducting, the critical wavelength of the surface will be investigated according to their model. The gained result may be applied to understand how to achieve a good surface quality during CMP process.

In this study, the synergy between chemical dissolution and mechanical abrasion is studied by nano-wear tests to reveal the stress enhanced chemical dissolution mechanism. Mechanical wear tests followed by chemical etching are designed and conducted. The evolution of the wear depth and the surface roughness at certain wavelength are examined with the dissolution time for a mechanically abraded surface.

4.2 Experimental Modeling by Nano Wear Experiment

The nano-wear test is performed on a Hysitron nano-indenter to study the synergistic effect between the chemical dissolution and mechanical abrasion. The effect of chemical dissolution on mechanical wear is believed to form a soft surface layer as describe in chapter 3. Chemical exposure followed by mechanical wear test is studied to verify the idea. The effect of mechanical abrasion on the chemical dissolution is investigated by mechanical wear test followed by chemical dissolution. These two sets of experiment are schematically shows in Fig 4.1. Fig 4.1(a) shows the dry wear test (wear test on reference surface) and wet wear test (wear test on chemically exposed surface), chemical softening effect will be studied by comparing the dry wear depth to wet wear depth. Fig 4.1(b) shows the dry test and wet test (mechanical wear followed by chemical exposure) conditions, residual stress enhanced dissolution effect will be studied by comparing the dry wear depth to the wet wear depth. The

multi-pass wear test followed by chemical exposure, then followed by multi-pass wear test is also performed to study the interaction pattern of chemical dissolution and mechanical abrasion.

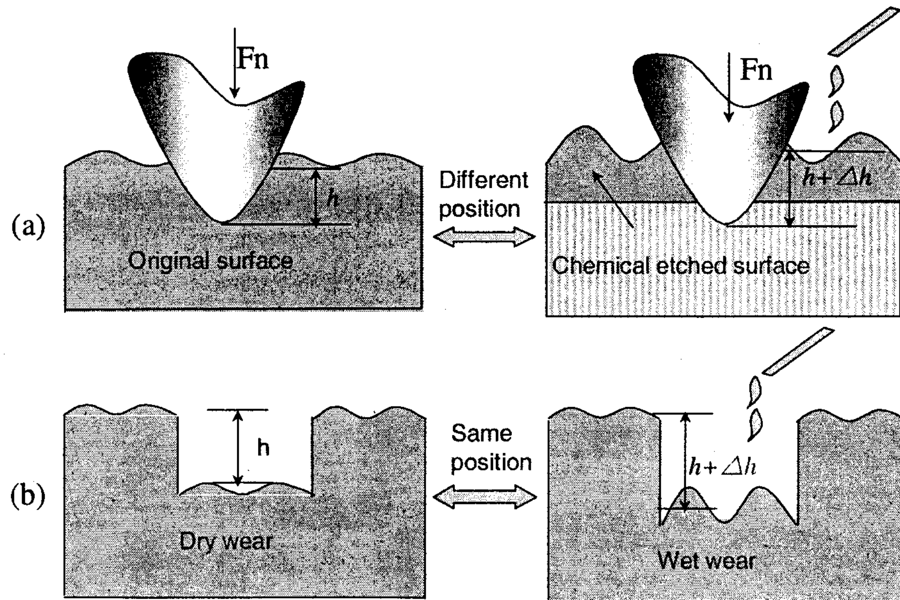

Fig 4.1 Schematic of nano wear test: (a) Chemical exposurefollowed by Mechanical wear (b) Mechanical wear followed by chemical exposure.

4.2.1 How nano-indenter do wear test

A wear test is performed on a region by repeatedly scanning that region with the applied contact force, and then the surface profile is scanned in a larger window containing the wear region with a normal imaging contact force.

During the wear test, the indenter tip rasters the surface in a scanning pattern using a three-axis piezo positioner. The X-Y piezo moves the tube across the surface, while the Z-axis position is controlled by a feedback loop to keep the applied normal force constant during rastering.

4.2.2 Experiment procedures of nano-wear test

The wear test can be run manually using "Imaging panel" or automatically using "Method". It should be noted that, for each wear test, after the tip engages on the surface, let the tip set there for 2 minutes to settle the piezo, then start scanning surface to get a reliable surface profile..

1. The general procedures for a wear test:

1) Pick the testing region on the copper specimen.
2) Set up the wear load function, including scan size, scan rate, set point (wear force), scan direction, scan pass.
3) Set up the imaging function, including scan size, scan rate, set point (usually 2 μN), scan direction (usually perpendicular to wear direction), scan pass.
4) Run the wear test at specified wear load function.
5) Scan on a larger region including wear region and save the image.

2. The experimental procedures for wear test I (chemical exposure followed by mechanical wear):

1) Prepare the copper sample and locate the testing positions.
2) Set up the wear load function, including scan size (e.g. 20μm by 20μm), scan rate (e.g. 1Hz), set point (adjusted-parameters), scan direction (e.g. 90°), scan pass (ex. Pass 1). Either set point or scan pass can be changed for a set of automatic wear tests. Here, set point is increased from 10μN to 40μN with an increment of 10μN.
3) Set up the imaging function, including scan size (e.g. 40μm by 40μm), scan rate (0.5Hz), set point (2μN), scan direction (0°), scan pass (e.g. 1).
4) Specify wear test patterns and wear test position groups (This will determine the

number of wear tests that are going to be run).

5) Run the dry wear tests automatically by using "Method Panel" and save the surface profiles with "post-scan" using imaging function.

6) Expose the surface to a slurry for a certain time (e.g. 0.6 wt% NH_4OH for 10 minutes.), then dry surface gently with pure air.

7) Set up the wear load function same as step 1.

8) Set up the imaging function same as step 2.

9) Select neighboring regions where dry test is done and run wear test as shown in step 3 and 4.

10) Look for the difference in surface profiles between dry and wet wear test.

3. The experimental procedures for wear test II (mechanical wear followed by chemical dissolution):

1) Prepare the copper sample and locate the testing positions.

2) Set up the wear load function, including scan size (e.g. 20μm by 20μm), scan rate (e.g. 1Hz), set point (e.g. 20μN and 40μN), scan direction (e.g. 90°), scan pass (ex. Pass 1).

3) Set up the imaging function same as wear test I.

4) Run dry wear test manually and save the surface profiles.

5) Expose the surface (including wear region) to 0.6 wt% NH_4OH slurry for 30s, and then dry the surface carefully with pure air.

6) Scan the worn regions again and save the surface profiles.

7) Repeat step 5 to step 6 with different exposure time until the difference in surface profile due to dissolution is very small between the two consecutive data.

8) Analyze the wear test data between dry and wet wear tests.

4. The experimental procedures for wear test III (multi-pass wear test, chemical exposure, multi-pass wear test):

1) Prepare the copper sample and locate the testing positions.
2) Set up the wear load function, including scan size (e.g. 20μm by 20μm), scan rate (e.g. 1Hz), set point (ex. 40μN), scan direction (e.g. 90°), scan pass (adjusted-parameters). Here, scan pass is increased from 1 to 4 with an increment of 1 manually.
3) Set up the imaging function, including scan size (e.g. 40μm by 40μm), scan rate (0.5Hz), set point (1μN), scan direction (0°), scan pass (e.g. 1).
4) Run the dry wear tests manually and save the surface profile for each wear pass until pass number 4.
5) Expose the surface to 0.6 wt% NH_4OH slurry for 90s, and then dry the surface carefully with pure air.
6) Scan the worn region after etching and save the surface profile.
7) Run another multi-pass wear tests on the same worn region. Save surface profile for each wear pass.
8) Analyze the multi-pass wear test data.

4.2.3 Data analysis of experimental data for wear test

The surface profiles taken from scanning have to be processed with background subtraction to remove the tilt of the specimen. There are different methods for background subtraction. The simplest one for tilt correction is linear regression. However, linear

regression method only works well for the surface without deep indent or scratch or recessed area. For the wear test, the middle region of the image is lower than the surrounding region, so zone subtraction technique has to be used to remove the surface background.

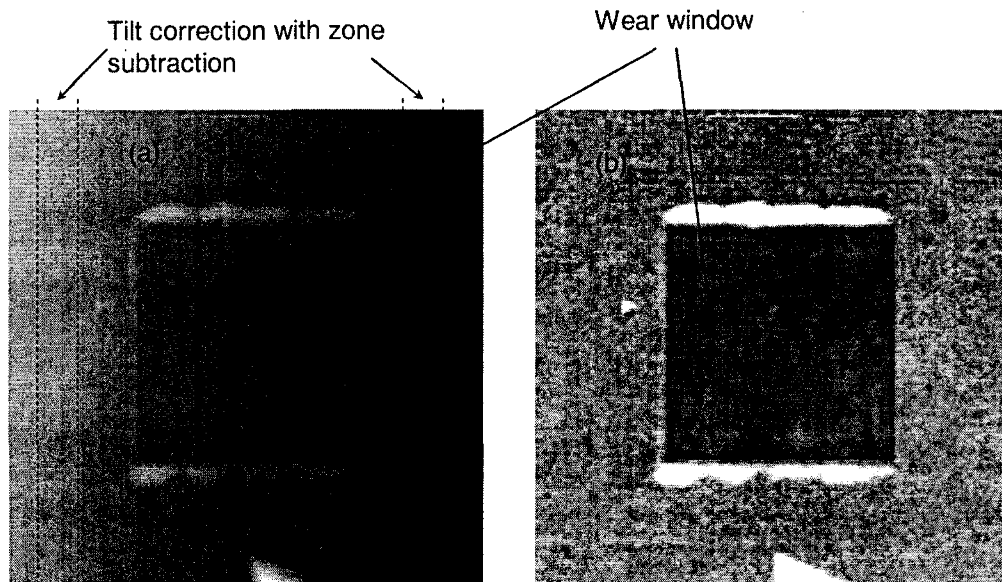

Fig 4.2 Tilt correction for wear surface profile (a) original data (b) Corrected data with zone subtraction

In zone subtraction, two zones on the surface (left and right non-wear region as shown in Fig 4.2) are selected and the surface slopes of the two zones are found. Assuming that the slopes of two zones are representative of the surface slope, then the surface slope can be removed. A typical wear image with and without background subtraction is shown on Fig 4.2. Fig 4.2 (a) is the original data that shows the surface profiles without zone subtraction. The gray scale presents the difference in the height. It is shown in Fig 4.2(a) that the wear region is recessed, and the surface is tilted since the left side is higher than the right side. Fig 4.2 (b) shows the images with background subtraction using zone subtraction technique. Since the

gray scale is nearly same for the surrounding region of wear area, it is clear that the surface background is subtracted from the surface (assumed to be 1st order).

1. Wear depth measurement.

One of the important parameters in the wear tests is wear depth or wear volume. In the current wear test (as shown in Fig 4.2), wear volume is simply the product of the wear depth and the wear area (known from wear window size). So wear depth can be used to study the difference of wear resistance of the material between dry and wet tests, or between single-pass and multi-pass test. A typical line profile across the wear region is shown in Fig 4.3. It can be seen that the wear is done from 10μm to 30μm in lateral displacement. The wear depth can be taken as the difference of mean height between non-wear region and wear region.

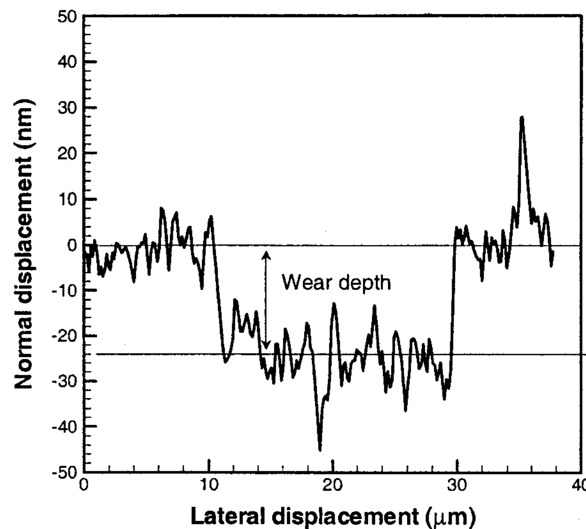

Fig 4.3 A typical line profile showing wear depth.

For each wear test, since there are about 128 line profiles showing the wear depth, the wear depth under the normal force is taken as the average of those data. So the wear depth

can be measured based on the mean height difference between the wear region and non-wear region as shown in Fig 4.4. After the surface background is correctly subtracted from the surface, three regions are picked as shown in Fig 4.4. Left region and right region are the non-wear regions, and middle region is the wear region. Wear depth is calculated by subtracting the mean height of the middle region from the average mean height of left and right regions. Usually the difference between the mean height of the left region and the right region is quite small (less than 2 nm) by correct zone subtraction, so zone subtraction technique is very reliable for surface background subtraction for our tests.

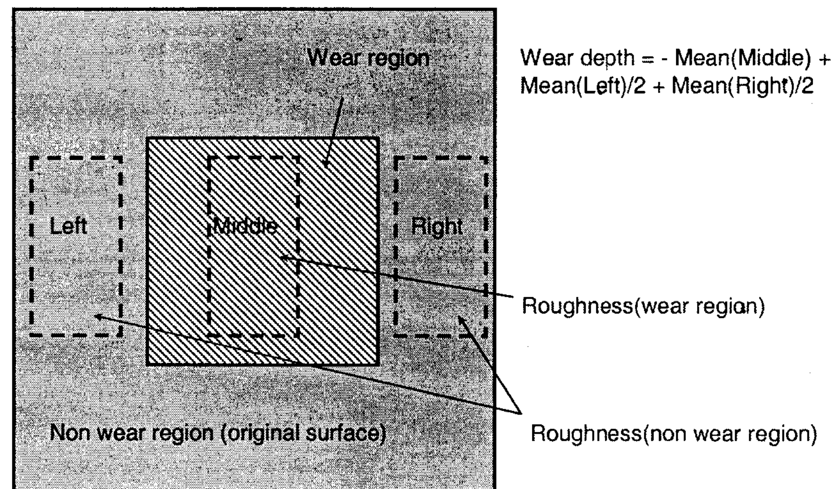

Fig 4.4 Schematic of region selection for wear data analysis

2. Surface roughness measurement.

The most widely used mean-line roughness parameters are arithmetic average R_a and root-mean-square (RMS). RMS is just the standard deviation in terms of the surface height

distribution.

The arithmetic average R_a, is the most widely used roughness parameter because of its ease of measurement. It is defined (in discrete form) as

$$R_a = \frac{1}{n}\sum_{i=1}^{n} X_i \tag{4.1}$$

where n is total number of data points, and X_i is the height for data point *i*.

Compared to R_a, RMS is more sensitive to the large deviations (peaks or valleys) from the mean line. It is defined (in discrete form) as

$$RMS = \sqrt{\frac{1}{n}\sum_{i=1}^{n}(X_i - R_a)^2} \tag{4.2}$$

If the surface height distribution is symmetrical Gaussian distribution, then the relationship between the RMS and R_a can be approximated by (Thomas, 1999)

$$RMS = 1.25R_a \tag{4.3}$$

3. Wavelength analysis

The wavelength of the surface roughness is extracted from 2-D discrete Fourier transform (DFT) of matrix *f(m,n)* (experimental surface height data with 256 by 256 data point), computed with a fast Fourier transform (FFT) algorithm.

2-D DFT is define as

$$F(\omega_1, \omega_2) = \sum_{m=-\infty}^{\infty}\sum_{n=-\infty}^{\infty} f(m,n) e^{j\omega_1 m} e^{j\omega_2 n} \tag{4.4}$$

where *f(m,n)* (refer to experimental data matrix) is a function of two discrete spatial variables *m* and *n*, which are related to lateral displacement in both surface directions. $F(\omega_1, \omega_2)$ is the 2-D fast Fourier transform of *f(m,n)*. The variables $\omega_1$and ω_2 are frequency variables with

unit radians per sample, which are ready to be converted to the unit 1/Length.

4.3 Experimental Results

The experimental results for the nano wear experiment described in section 4.2.2 are shown from section 4.3.1 to 4.3.3. The result of wavelength evolution will be discussed in section 4.6. Only wear depth and surface roughness data are presented in this section.

4.3.1 Chemical exposure followed by mechanical wear

1. 0.6wt% NH_4OH slurry

During CMP process, slurry containing active chemical agents will react with the surface. It has been shown in chapter 3 that a soft lay is formed for copper exposed to certain type of slurries (such as 0.6wt% NH_4OH). This softened chemical reacted product layer will increase the mechanical abrasion rate compared to the dry conditions at the same operating parameters. To verify this idea, a set of wear test is conducted on the copper surface exposed to 0.6wt% NH_4OH for 10 minutes, and the results are compared to the dry wear data.

The experimental results are shown in Fig 4.5. Fig 4.5(a) shows the variation of wear depth with normal force. Fig 4.5(b) shows the variation of roughness with normal force. In the figure, "dry" refers to wear tests on copper surface without etching; "wet" refers to the wear tests on chemically etched copper surface; "wear" refers to the data measured in wear region; and "nonwear" refers to data measured in the non-wear region. The applied wear force ranges from 10μN to 40μN. The dry wear depth ranges from approximately 4 nm to 10nm, and the wet wear depth ranges from 8 nm to 16nm. It clearly shows that chemical reacted product layer will increase the wear depth (caused by mechanical abrasion) by nearly 60% to 100%. It is evident that the percentage increase in MRR depends on the applied

normal force level (an operational parameter), the soft layer thickness of (controlled by the exposure time and the reaction rate) as well as mechanical properties of the soft layer. However, it is worth noting that this soft layer is not the only reason for the increase in the wear depth. From Fig 4.5(b), the roughness of the original surface is about 3nm, after etching, the roughness goes to about 6nm. The roughening effect caused by chemical dissolution leads to a topography favored mechanical abrasion that will also enhance mechanical abrasion. So for NH_4OH slurry, surface softening and roughening are the two possible mechanisms for the increase in wear rate. For other type of slurry, like 1wt% HNO3 +0.5wt%BTA, roughening my not be the case which will be shown later.

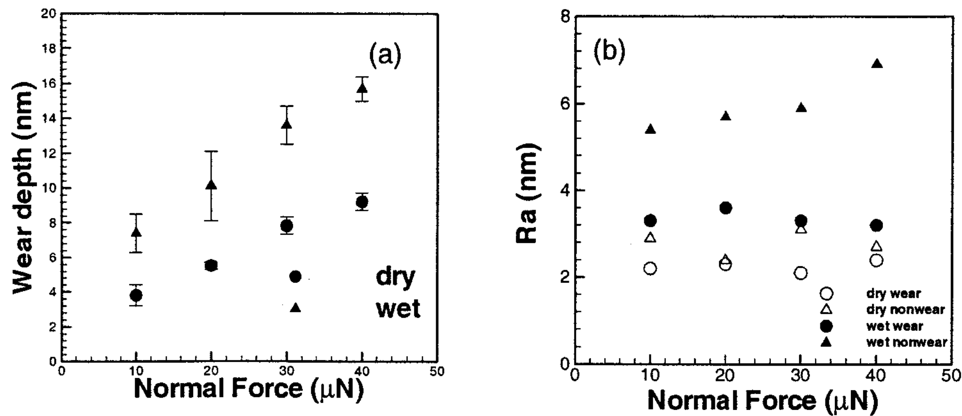

Fig 4.5 Experimental data for chemical exposure followed by Mechanical wear test, (a) Wear depth evolution, (b) roughness evolution (0.6wt% NH_4OH for 10 minutes).

4.3.2 Mechanical wear followed by chemical dissolution

From thermodynamics, chemical reaction rate are not only related to the change of free energy, but also surface energy and elastic strain energy. During wear test, residual stress will be introduced in the near surface that causes the change of elastic strain energy, so will

affect the chemical dissolution rate. To investigate this, a set of wear tests are done on the dry copper surface, then put chemically active slurry on the wear region and measure the topography evolution with etching time.

A. 0.6wt% NH_4OH slurry

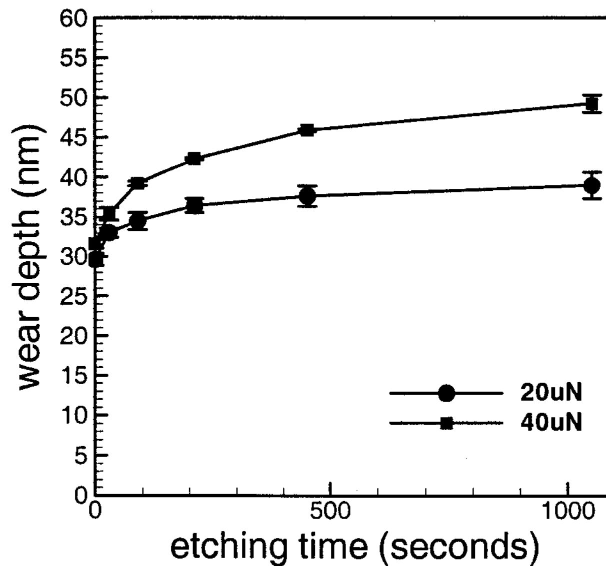

Fig 4.6 Variation of wear depth with chemical dissolution time for mechanical wear followed by chemical dissolution test (0.6wt% NH_4OH)

Fig 4.6 shows the variation of wear depth with exposure time for this type of test. Initially, 4 dry wear passes at 40μN or 8 dry wear passes at 20μN are employed to provide approximately the same wear depth but with different residual stress levels. The surface topographic evolutions are measured as a function of the exposure to the slurry. Starting with almost the same level of cumulative dry wear level, it is evident that the increase in the wear depth depends on the level of the accumulated residual stresses levels. It is evident also that the change of the wear depth with time follows an exponential decay rate until the whole

residually stressed layer is consumed. A net enhancement of the dry wear trench by ~15% to ~30% is clearly observed on different etching time.

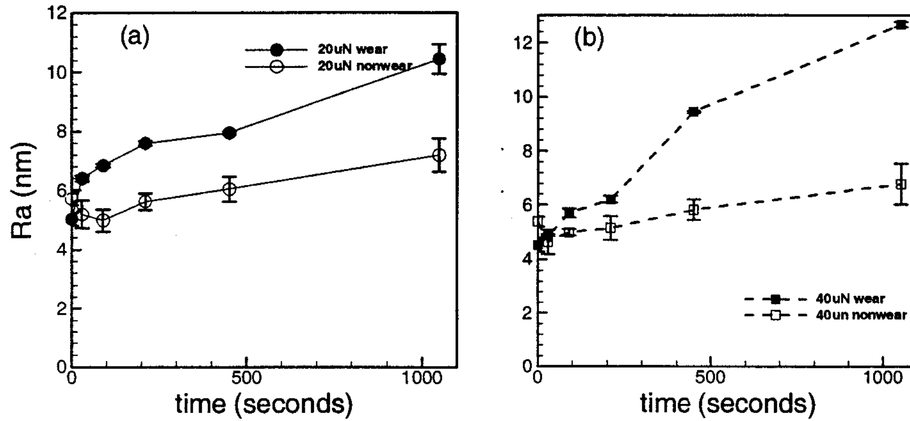

Fig 4.7 Variation of roughness with exposure time for mechanical wear followed by chemical dissolution (a) 20μN wear force, (b) 40μN wear force (0.6wt% NH_4OH).

The evolution of roughness with exposure time is shown in Fig 4.7. Fig 4.7(a) shows the data under 20μN wear force, and Fig 4.7(b) shows the data under 40μN wear force. It is shown that at the initial 90s, the wear region roughens quickly for both tests, which could be the stress induced roughening. The non-wear region smoothes a little bit or doesn't change due to data resolution. After the initial stage (about 90s exposure time), both regions roughen at about the same rate. This could be the reason for the evolution of wear depth shown in Fig 4.6. In Fig 4.7 (b), the roughness data shows a weird trend after 200s of exposure time. That could be some unforeseen factor when the experiment is done, such as some dirt, or particles falls in the data region. By comparing to other roughness data, the big jump from ~6nm to ~10nm in roughness after 200s exposure time for wet test under 40μN wear force is not reliable.

B. 1.0wt% HNO_3+ 0.5wt% BTA

The residual stress enhanced etching is observed in the experiment shown in Fig 4.6. Different slurry, 1wt% HNO3 +0.5wt%BTA, which is another common slurry used for Cu CMP, is tested for stress-enhanced etching. A set of wear tests ranges from 10μN to 40μN are done on the dry copper surface, then exposed to 1wt% HNO_3 +0.5wt%BTA slurry for 10 minutes. The experimental results are shown in Fig 4.8. In Fig 4.8, "dry" refers to wear tests on copper surface without chemical exposure; "wet" refers to the wear tests on chemically exposed copper surface; "wear" refers to the data measured in wear region; and "nonwear" refers to data measured in the non-wear region.

Fig 4.8(a) shows the wear depth variation with normal force, and Fig 4.8(b) shows the variation of roughness with normal force. From Fig 4.8(a), it shows the wet wear depth is larger than dry wear depth, meaning that the chemical reaction occurs due to the change of elastic energy. It is noted that there is a jump in wear depth between 20μN to and 30μN. That may be caused by indenter tip shape. For wear force smaller than 20μN, the wear depth is shallow. Only the spherical part of tip indented into the surface, and it is a spherical indentation. For wear force larger than 40μN, the wear depth is deeper. Not only the spherical part of tip, but also the conical part of the tip indented into the surface, and it is a spherical-conical indentation, which should cause larger indentation depth. The difference in wear depth between dry and wet test ranges from 2 to 4 nm for different wear force. Although the chemical dissolution rate seems very small, the stress-induced dissolution is observed for this type of slurry. It is shown in Fig 4.8(b) that surface roughness after wear is about 3nm, and roughness before wear is about 4nm. So the wear test is like a polishing process that smoothes the surface. Little difference in roughness is observed between "dry"

and "wet" test for both wear and non-wear region. Compared to Fig 4.5, this slurry doesn't roughen the non-wear region after 10 minutes etch, which shows this slurry is very inactive. Compared to Fig 4.7, this slurry doesn't roughen the wear region after 10 minutes exposure, so stress-induced roughening is not observed in the current test.

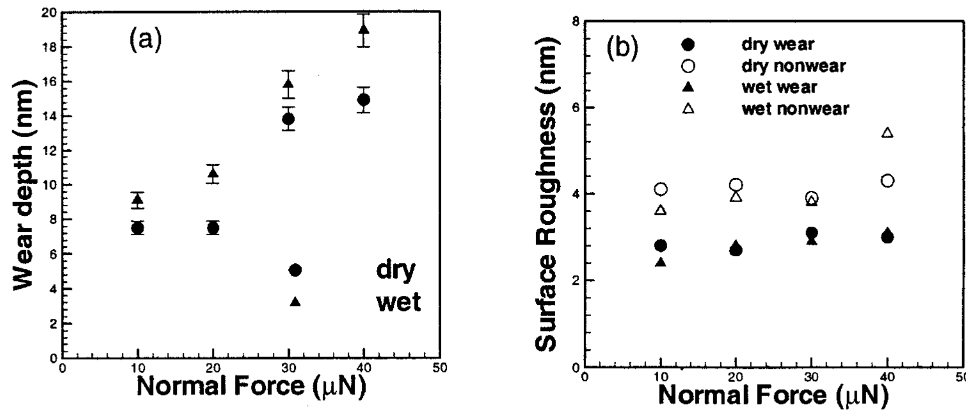

Fig 4.8 Experimental data for mechanical wear followed by chemical expsoure test, (a) wear depth evolution with etching time, (b) roughness evolution with etching time (exposed to 1wt% HNO_3 +0.5wt%BTA slurry).

It should be noted that the reported static etch rate for this slurry is close to 0 nm/min (Steigerwald, 1995). However, due to the change of elastic strain energy caused by wear, the reaction occurs for this inactive slurry. This fact ascertain that the increased etch rate is stress assisted chemical dissolution.

4.3.3 Wear test III (multi-pass wear test-chemical dissolution-multi-pass wear test, 0.6wt% NH4OH slurry)

To simulate the polishing process, a multi-pass wear test followed by chemical exposure,

then another set of multi-pass wear tests is done on the same area to investigate how material is removed from the surface. The experimental results of this test are shown in Fig 4.9. The solid circle represents the absolute value of wear depth, and hollow circle describes the increment in wear depth between two consecutive tests.

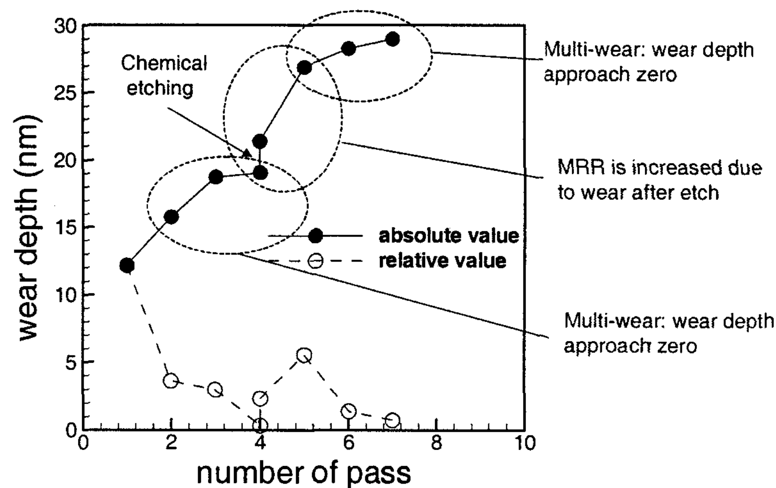

Fig 4.9 Wear depth evolution with number of wear pass (exposed to 0.6wt% NH_4OH slurry).

A compound multi-pass wear test is carried out to examine the mutual effects of both mechanisms on the material removal. The test is composed of 4-passes dry wear at 40μN normal force, followed by chemical slurry exposure to 0.6wt% NH_4OH for 90 seconds, then another set of 3-pass dry wear at the same force level. This figure shows the steady abrasion of dry wear, the instantaneous jump due to stress enhanced chemical dissolution, the chemical enhanced abrasion and the steady wear to follow after that. The first data point represents the initial unsteady wear due to interaction with the initial surface asperities and roughness. The depth increment is increased nearly by 15% due to residual stress enhanced

etching (5th point). The fifth wear path (6th point, immediately after exposure) shows the largest depth increment compared to other increments. This test clearly shows the synergistic significance between chemical dissolution and mechanical abrasion on material removal process. The wear rate caused by the interaction between chemical etching and mechanical abrasion is much larger than the pure mechanical abrasion rate or chemical etching rate alone. So material removal mechanism in CMP process is mainly mechanical-chemical.

4.4 Existing Thermodynamic Model for Wavelength Selectivity

It has been shown that a flat surface with residual stress in the near surface is unstable under chemical etching. Surface with spatial frequency below a critical value grows while surface roughness of higher frequency decays (Kim et al 1999, Suo et al 2000). Theory related to this is derived (Kim et al 1999, Suo et al 2000). Their model will be used to estimate the critical wavelength for our nano-wear experiment. Their model for reaction near equilibrium is briefly described below.

For a stressed solid with a curved surface, the driving force (such as the change of free energy) to change the shape of its reference configuration is represented by (Herring, 1951),

$$F = g - w - K\gamma \tag{4.5}$$

where F is driving force, g is free energy difference between two atoms in the two bulk phase, w is the strain energy density along the surface, γ is the surface energy density between solid-etchant interface, K is the surface curvature.

Assuming linear kinetic laws, the chemical reaction rate (A projection to the direction normal to the surface) is

$$\frac{dH}{dt} = R = MF\sqrt{1+|\nabla H|^2} \tag{4.6}$$

where H is the surface height, R the chemical reaction rate, M is the linear kinetic constant of etching, . ∇ is the two dimensional gradient operator.

During surface evolution, the projected average of the chemical potential is maintained constant (Gao, 1994), by assuming a shallow etching of nearly flat surface, the approximated surface roughness evolution is

$$\frac{dh}{dt} = M\left(\gamma\nabla^2 h + \Delta w\right) \tag{4.7}$$

where h is the surface roughness, $\Delta w = w - w_0$, w_0 represents strain energy density for a flat surface, which can be described by

$$w_o = \frac{\sigma_1^2 + \sigma_2^2 - 2\nu\sigma_1\sigma_2}{2E} \tag{4.8}$$

where σ_1 and σ_2 are the in plane principal stress, E is Young's modulus, ν is Poisson's ratio. The elastic strain energy density for a curved surface is (Yu et al 2000)

$$w = w_o - \frac{2(1+\nu)}{E}\left[(1-\nu)\left(\sigma_{11}^0\right)^2 + \left(\sigma_{12}^0\right)^2\right]\omega h \tag{4.9}$$

where σ_{11}^0 and σ_{12}^0 are the in plane stress, ω is the circular frequency of the surface in certain direction.

After Fourier transform of Eq. (4.7), by equating the surface roughness amplitude at a particular frequency after certain etching time to that at zero etching time, the critical wavelength is found to be

$$l_{cr} = \frac{E\gamma}{\sigma_1^2} \tag{4.10}$$

Based on this theory, surface roughness with wavelength larger than l_{cr} will grow under chemical etching, and surface roughness with wavelength smaller than l_{cr} will decay with chemical etching. Eq. (4.10) will be used to estimate the critical wavelength for our test configuration, and the calculated result will be compared to experimental data.

4.5 Numerical Simulation for Residual Stress under Double Indentation

According to Yu et al (2000), the critical wavelength is related to the stress level along the surface. To estimate the stress level in the near surface, wear process is simulated by a simplified double indentation using FEM software.

4.5.1 Numerical result for residual stress.

The residual stress under wear track is estimated by FEM simulation using ABAQUS/Standard. The implemented 2-D model is shown in Fig. 10.

The abrasive particle is assumed to be rigid while the ploughed substrate has material parameters consistent to those of copper (E=126GPa, σ_y=70MPa, σ_{ult}=220MPa). An isotropic elastoplastic strain hardening material model is used with hardening exponent n=0.2 for the substrate. It has been shown by Mesarovic and Fleck (2000) that poisson's ratio and friction between the two-body in contact are minor factors for static indentation. We take poisson's ratio to be 0.33 for the substrate, and no friction is considered between the particle and the substrate. The particle diameter is taken to be 400 nm, and the indentation depth is taken to be 10 nm. The contact radius is about 60nm. The first indent is 15nm offset from the symmetry line shown in fig 4.10.After unloading of first indent, the particle is offset to the other symmetric position. Then the 2nd indent is done and unloaded. The other offset distance, 30nm and 45nm are also simulated. The dimension of the copper substrate is "50a" high and

"100a" long to eliminate the edge effect (Storakers and Larsson, 1994). The bottom of the substrate is fixed.

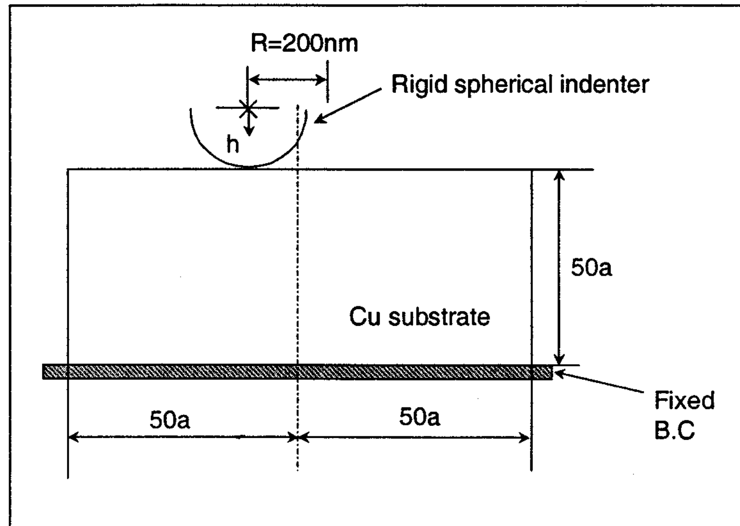

Fig 4.10 2-D double-indent FEM simulation model ("a" is contact radius after fully indentation)

For a typical 2-D indentation, the mesh contains more than 15000 4-node bilinear quadrilateral elements. Fig 4.11(a) shows the mesh close to the indentation region. From indentation position to "a", the mesh is finest, then become coarser and coarser from "a" to "2a", from "2a" to "5a", from "5a" to "50a" (Storakers and Larsson, 1994). The Mises stress contour plot after fully unloading is shown in Fig 4.11(b). At the valley shown in Fig 4.11(b), the residual stress level is estimated to be 180MPa and 200MPa along the surface directions for 15mm offset, 100MPa and 130MPa for 30mm offset, 120MPa and 160MPa for 45mm offset (All these values are approximate). At the crest shown in Fig 4.11(b), the residual stress level is estimated to be 40MPa and 20MPa along the surface directions for all the simulations.

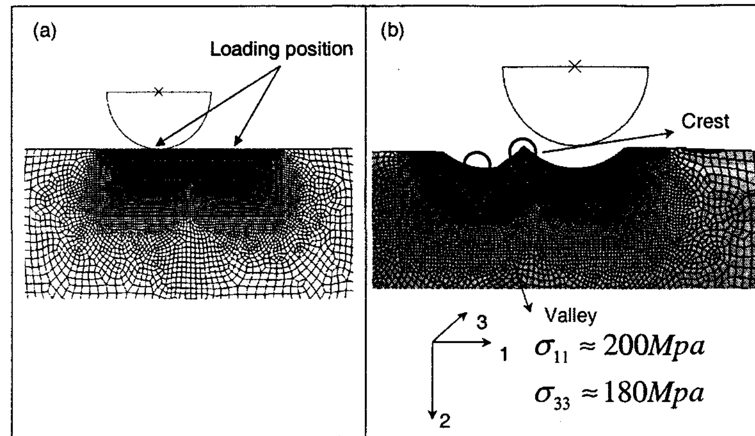

Fig 4.11 Estimation of residual stress under wear track by FEM simulation, (a) Model mesh before loading, (b) Mises contour plot after fully unloading

4.5.2 Analytical estimation for residual stress under single indentation

The residual stress after unloading from a plastically deformed state for single spherical indentation has been described by Johnson (1985). The residual stress is estimated by superposition of two stress states. The 1st stress state is the elastic plastic spherical indentation (loading stage). The 2nd stress state is elastic unloading given applied pressure distribution that is determined from loading state.

Assuming fully plastic indentation and uniform pressure distribution, the residual stress is found to be 40% of the substrate yield strength along the surface. At "0.64a" ("a" is contact radius here) below the indentation position, the residual stress is found to be 95% of the substrate yield strength, which is the maximum value.

Neglecting the difference of the stress state at the valley between single indentation and double indentation, the stress level in the near surface close to the valley ranges from

~100MPa to ~200MPa for copper by comparing analytical result of single indentation to FEM simulation of double indentation.

4.5.3 Experimental results for wavelength selectivity

For nano wear tests followed by chemical etching, the topographic measurements were made by 256 by 256 digital sampling over an area of 20μm by 20μm (or 40μm by 40μm) before etching and after etching at the wear area. Then the surface roughness at a specific frequency and etching time are evaluated numerically using a fast Fourier transformation code. The experimental results for surface etched by 1wt% HNO3 +0.5wt%BTA for 10 minutes are show in Fig 4.12. The Y-axis is related to the amplitude of the surface roughness, and the X-axis is the surface frequency. The amplitude of low frequency (frequency at left part of intersection point) after etching ("wet dry wear" in Fig 4.12) is higher than that before chemical exposure ("dry wear" in Fig 4.12), meaning surface roughness with long wavelength grows. The amplitude of high frequency (frequency at right part of intersection point) after etching is lower than that before chemical exposure, meaning that surface roughness with short wavelength decays. A critical wavelength of about 0.7μm can be identified from the intersection point of Fig 4.12.The experimental results for surface etched by 0.6wt% NH_4OH are show in Fig 4.13. A similar trend is observed, and a critical wavelength of about 1.4μm is observed based on the intersection point.

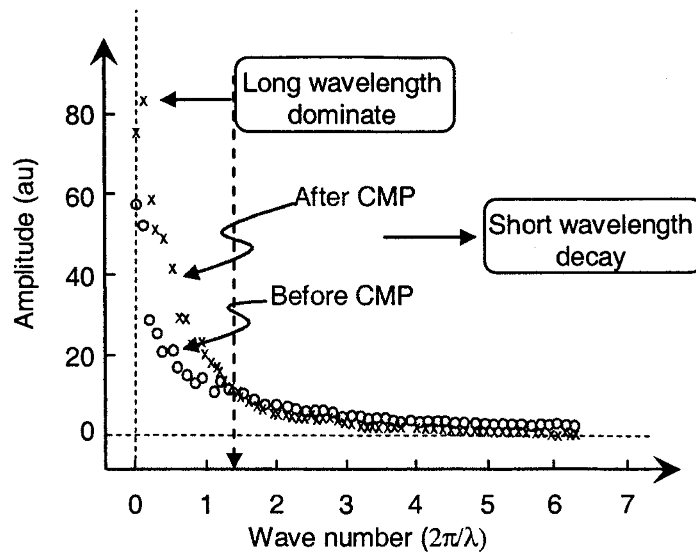

Fig 4.12 Experimental data showing long wave grows, and short wave decays for mechanical wear followed by chemical exposure to 1wt% HNO_3 +0.5wt%BTA slurry.

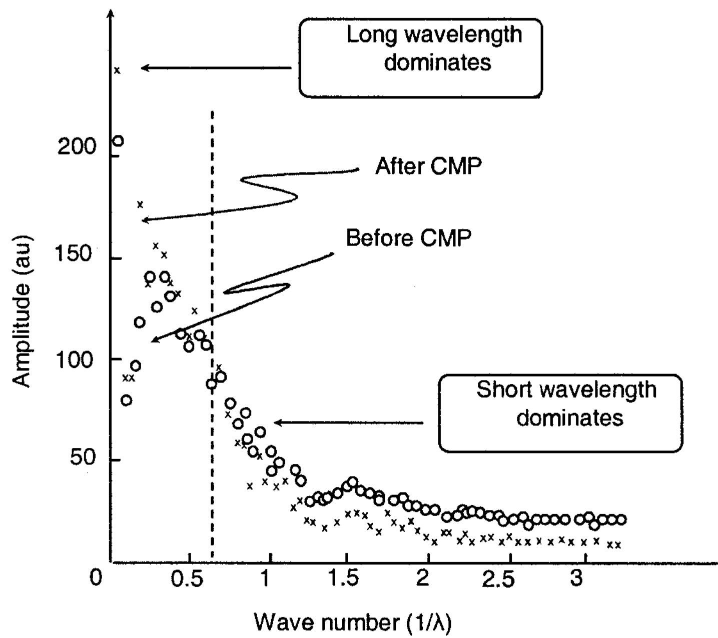

Fig 4.13 Experimental data showing long wave grows, show wave decays for mechanical wear followed by chemical exposure to 0.6wt% NH_4OH slurry.

Based on the results from 4.5.1 and 4.5.2, if reasonable interface energy ranges from 0.1 J/m^2 to 1 J/m^2 (Kim et al, 1999); a representative stress level is taken to be 160 MPa, and elastic modulus is 126GPa for copper. Then the estimated critical wavelength ranges from 0.5μm to 5μm. The experimental results we have for different type of slurry are within the range of the estimated value.

The wavelength selectivity for stressed solid under etching could be beneficial to achieve a global and local smooth surface, since the mechanical polishing helps smooth the long wavelength and the chemical etching helps smooth the short wavelength.

4.6 Conclusion

Systematic nano-wear tests have been designed and conducted on electroplated copper with and without chemical exposure. It has been observed that the synergy between chemical dissolution and mechanical abrasion play an important role in material removal during CMP process. The chemical enhanced mechanical abrasion increased the wear depth by as much as 100%, and the mechanical enhanced chemical etching increased the wear depth by as much as 30%. The percentage increase is determined by the operational parameters (i.e. applied pressure), properties and thickness of chemical product. The wavelength selectivity phenomenon due to residual stresses is also observed to enhance local planarization. It should be noted that all mechanisms exist in the actual polishing process. Their cumulative effects will control the effective MRR. Further studies are needed to render these models into practical design space parameters for CMP process optimization.

4.7 References

1. ABAQUS User Manuals, Ver. 6.3.1, Hibbitt Karlsson and Sorensen Inc., Providence, RI, 2003.
2. Chang, J.P. and Sawin, H.H., Notch formation by stress enhanced spontaneous etching of polysilicon, Journal of Vacuum Science and Technology B: Microelectronics and Nanometer Structures, Vol. 19, No. 5, pp 1870-1873, September/October, 2001.
3. Cook, L.M., Chemical processes in glass polishing, Journal of Non-Crystalline Solids, Vol. 120, pp 152-171, 1990.
4. Cook, L.M., Marker, A.J.III, Mader, K.-H., Bach, H. and Mueller, H., Leached antireflection surfaces: part 2. characterization of surfaces produced by the neutral solution process, Glastechnische Berichte, Vol. 60, No. 9, pp 302-311,1987.
5. Gao, H.J.S, Some general properties of stress-driven surface evolution in a heteroepitaxial thin film structure, Journal of the Mechanics and Physics of Solids, Vol. 42, No. 5, pp 741-772, May, 1994.
6. Herring, C., in The Physics of Powder Metallurgy, edited by Kingston, W.F., New York, McGraw-Hill, pp 143-179, 1951.
7. Izumitani, T., Treatise on Material Science and Technology, New York, Academic Press, Vol. 17, pp 115, 1979.
8. Johnson, K.L., Contact Mechanics, Cambridge, Cambridge University Press, 1985.
9. Kim, K.-S., Hurtado, J.A. and Tan, H., Evolution of a surface-roughness spectrum caused by stress in nanometer-scale chemical etching, Physical Review Letters, Vol. 83, No. 19, pp 3872-3875, Nov 1999.
10. Mesarovic, S.D. and Fleck, N.A., Frictionless indentation of dissimilar elastic-plastic

spheres, International Journal of Solids and Structures, Vol. 37, No. 46, pp 7071-7091, Nov 2000.

11. Nogami, M. and Tomozawa, M., Effect of stress on water diffusion in silica glass, Journal of the American Ceramic Society, Vol. 67, No. 2, pp 151-154, Feb 1984.

12. Srolovitz, D.J., on the stability of surfaces of stressed solids, Acta Metallurgica, Vol. 37, No. 2, pp 621-625, Feb 1989.

13. Steigerwald, J.M., Murarka, S.P., Gutmann, R.J, and Duquette, D.J., Chemical processes in the chemical mechanical polishing of copper, Materials Chemistry and Physics, Vol. 41, No. 3, pp 217, Aug 1995.

14. Storakers, B. and Larsson, P.-L., on Brinell and Boussinesq indentation of creeping solids, Journal of the Mechanics and Physics of Solids, Vol. 42, No. 2, pp 307-332, Feb 1994.

15. Thomas, T. R., Rough surfaces, London, Imperial College Press, 1999.

16. Vyvoda, M.A. and Graves, D.B., Stress evolution and notch formation during polysilicon gate electrode etching, Materials Research Society Symposium - Proceedings, Thin-Films - Stresses and Mechanical Properties VII, Vol. 505, pp 433-438, 1998.

17. Yu, H.H. and Suo, Z., Stress-dependent surface reactions and implications for a stress measurement technique, Journal of Applied Physics, Vol. 87, No. 3, pp 1211-1218, February 2000.

Chapter 5 Conclusion and Future Work

5.1 Conclusion

5.1.1 Phenomenological material removal models

A mechanism based MRR model based on scratch intersection is developed and applied to MRR prediction of CMP process. This is a departure from existing MRR models, where it is assumed that a moving abrasive particle removes material all along its track. The present model assumes that material is plowed to the track sides, and no net material is detached. However, it is only detached when two particle tracks intersect each other at a favorable angle. In contrast to existing practice where Preston constant has typically been used to fit the model predictions to experimental observations and usually poss unrealistic dimensional units, the proposed scratch intersection model is physically motivated, and provides predictions for Preston constants up to a dimemsionless constant with the same order as those measured experimentally for CMP of copper (Figs 2.10 and 2.11). To further realize the model utility of the scratch intersection concept, if one would compare any of the existing models that relies on the assumption of removal of materials along the entire track of the abrasive particle, then the predicted MRR would be about three order of magnitude higher than experimental measurements. Moreover, the scratch intersection model predictions of MRR variations with pressure and velocity are also very similar to observed experimental trends.

It has been observed in the literature (e.g., Zhou et al 2002, Mahajan et al 1999) that under different conditions, the MRR may show an increasing or decreasing trend with

increasing particle size and concentration. It is observed in our model developments that this apparent ambiguity is due to different regimes of slurry-pad interactions, which induce completely different deformation modes and its associated force partitioning in the CMP process. The proposed scratch intersection based CMP model delineates these different regimes of operation. It is noted that for soft pads subject to relatively small particle sizes and low particle concentrations, the pad undergoes a local deformation pattern where the abrasive particle indents the pad surface. The force partition associated with such a deformation mode causes increasing trend in MRR with increasing particle size and increasing particle concentration. As the particle size and concentration increases, the pad deformation mode changes from indentation at particle scale to a macroscopic cell flexing mode, where cells or strands on the pad surface deform entirely by bending. In this regime of slurry-pad interaction, the nature of force partition changes, causing decreasing trend in MRR with increase in either particle size or particle concentration. The proposed scratch intersection models can capture both regimes, and the model predictions correlate quite well to experimental observations.

The proposed model provides means to predict the Preston constant as a function of the full process parameters, including detailed pad morphology, particle size and concentration, polished surface mechanical properties as well as the external control variables of applied pressure and relative velocities. Such detailed model would provide the means to explore the design space and optimize the process parameters.

5.1.2 Synergy between mechanical abrasion and chemical dissolution

In order to understand the material removal mechanism during CMP process, the

synergies between chemical dissolution and mechanical abrasion during CMP of copper have been explored by both experimental and modeling techniques. We have investigated two plausible mechanisms of material removal from two parts; (i) chemical dissolution enhances mechanical abrasion and (ii) mechanical abrasion accelerates chemical dissolution.

For the mechanisms of chemical dissolution enhanced mechanical abrasion, it is proposed that a soft chemical product layer is formed on top of the polished surface due to chemical reaction with a rate much faster than the mechanical abrasion rate, and then it is followed by a gentle mechanical abrasion of that soft layer. A combined experimental and modeling technique has been devised to understand the mechanical properties of the soft layer as well as the layer thickness formed due to chemical exposure in CMP. The experimental approach utilizes nano-scratch and nano-dynamic mechanical analyzer (DMA) tests under dry (without chemical exposure) or wet conditions (with chemical exposure). In order to deduce the ratio of the soft layer yield strength to the substrate yield strength and as well as the layer thickness, the limit analysis solution of surface plowing under spherical traveling indenter has been used to analyze the nano-scratch experimental measurements. Three different types of slurries are used to form different type of surface layers as well as the layer thickness by varying the exposure time. The soft layer thickness is found to be in the order of few nanometers, and grows with the exposure time for the slurry tested. The yield strength of the soft layer is about 50% of that of the substrate for copper oxide. For non native copper film, Cu-BTA, the yield strength of the soft layer is about 20% of that of the substrate. The measured apparent modulus and hardness from a set of DMA tests at different indentation depth through the composite soft layer-substrate structure results are assessed in view of a detailed finite element simulation for the composite film-substrate structure to

deconvolute the ratio of film elastic modulus to substrate modulus. It is found that, for pure copper etched with ammonium hydroxide, the film modulus is about 20% of the substrate modulus.

It is shown from the nano scratch experiment that the chemical softening will enhance the mechanical abrasion by as much as 70% at low cutting depth with a fixed normal force for ammonium hydroxide. The gained results can be applied to slurry design optimization for yield improvements. The other insight gained from this exercise is a new nano-mechanical thin film characterization technique. When the film is very thin and the indentation depth has to be larger than the film thickness, the conventional indentation technique is very difficult to apply in this regime. The nano-mechanical testing technique developed here can be applied to characterize the film mechanical properties as well as film thickness.

For the mechanism of mechanical abrasion accelerating the chemical dissolution, the wear depth and surface topography evolution are investigated. We have made use of the established fact of stress enhanced chemical dissolution, wherein the flat surface of stressed solid is configurationally unstable under chemical dissolution. The roughness with wavelength above a critical value grows while roughness of lower wavelength decays during dissolution. Here, a study utilizing nano-wear experiment is performed to induce a local variation of the residual stress level, then followed by chemical dissolution to investigate the variation of the wear depth and the evolution of surface topography evolution due to dissolution. The residual stress enhanced dissolution is observed for slurry 0.6wt% NH_4OH and slurry 1wt% HNO_3 +0.5wt%BTA. It is found that the residual stress caused by the mechanical wear test enhances the chemical dissolution rate, as manifested by the increase of wear depth. The wavelength selectivity is also observed for stressed surface under chemical

dissolution, and the experimental observed critical wavelength falls in a reasonable range of the theoretical expectations. Chemical exposure followed by mechanical wear test is also investigated for 0.6wt% NH_4OH to verify the chemical enhanced mechanical abrasion. It is found that soft layer formation and surface roughening are two possible mechanisms for chemical enhanced mechanical abrasion. Combined with mechanical wear test followed by chemical dissolution, it is found that material removal rate (MRR) is increased by the synergistic effects between chemical dissolution and mechanical abrasion. The gained results from nano-wear tests could be applied to understand material removal mechanism during CMP process, and optimize process parameters and select the right type of slurry for a specific CMP process.

The developed understanding in this study can be used in future studies to understand the root causes of defect generation mechanism and render remedies for yield improvements. The results can also be used to optimize the process parameters, including (i) particle size and concentration, (ii) adapting slurry chemistry for required rates of chemical dissolution and mechanical abrasion and (iii) selecting pads with the proper surface morphology and stiffness.

5.2 Future Work

As predicted by the proposed scratch intersection model, the MRR trend with increasing particle size and concentration is found to change from an increasing trend to a decreasing trend when a critical value of particle size and concentration (relative to pad stiffness) is exceeded. Such a trend is clearly observed in the experimental data of Mahajan et al (2000). The transition point also shifts depending on specific particle size and concentration, and

other variables such as pad morphology and properties. From application prospective, determination of such transition points would be of great interest, since it could directly predict the MRR trends with particle size and concentration so as to maximize the MRR and improve the yield. Moreover, by including the details of the pad morphology, one would be able to predict the performance degradation and generation of defects due to pad wears and pore clogging.

For the material and slurry tested in this study, the film mechanical properties for copper oxide and copper-BTA as well as the film thickness are found by utilizing nano-scratch and nano-DMA tests and the methodology are generalized as a thin film characterization technique. The currently developed technique should be justified and refined against a much widely used engineering materials (which is currently being done in collaboration with Hysitron, Inc.). To achieve this, the pile up behavior for film-substrate structure for a variety of materials should be investigated experimentally and numerically. The current model doesn't consider stain hardening effect, which will affect the pile up behavior in elastic-plastic and fully plastic regime. If the pile up changes the contact area significantly, the current model has to be modified to consider the pile up effect. Interfacial film decohesion is also needed to be considered. The current model assumes a stable elastic-fully plastic plowing action. If film delamination occurs during scratch, the energy release rate from the advanced crack has to be considered in the formulation of the total potential energy of the system.

The developed understanding in material removal mechanism describes the synergy between chemical dissolution and mechanical abrasion, and dictates how material is being detached during CMP process. This framework would help in understanding the root causes

of defect generation mechanism and render remedies for yield improvements. The current test configuration only involves three different types of slurries on copper CMP, and only major chemicals in the slurry are considered. There are several different types of slurries used in copper CMP, oxide CMP and tungsten CMP. Each of these groups of slurry has various amounts of different oxidizer, inhibitor and surfactant. The Chemical reaction rate has to be taken into consideration when the current testing methodology is applied to screen the proper composition of the slurry chemistry to achieve a desired level of MRR. In each case, experimental validation should ascertain and verify the model prediction.

Appendix 1: Experimental Scratch Data and Film Thickness Measurement Data

1a. Experimental scratch data for 0.6wt% NH_4OH slurry

Table Appendix 1.1 Experimental scratch data for 600s exposure time

Scratch conditions	Applied normal force	Mean Fn (μN)	Mean Ft (μN)	Mean h (nm)	Error in Ft	Error in h
0s	10uN	10.83	1.9	5.1	1	0.7
	20uN	20.80	3.6	7.7	1	0.7
	30uN	30.77	7.0	10.3	2	1.5
	40uN	40.30	10.8	12.1	2	1.8
600s	10uN	9.73	3.2	9.0	1	1.1
	20uN	21.33	4.7	12.0	1	0.7
	30uN	29.00	7.6	14.1	2	0.9
	40uN	38.75	10.7	15.2	2	0.5

Table Appendix 1.2 Experimental scratch data for 300s exposure time

Scratch conditions	Applied normal force	Mean Fn (μN)	Mean Ft (μN)	Mean h (nm)	Error in Ft	Error in h
0s	10uN	12.00	2.60	3.55	1	0
	20uN	22.67	4.83	6.08	1	1.1
	30uN	30.83	6.97	8.74	2	2.0
	40uN	40.47	10.83	11.16	2	1.0

Table Appendix 1.2 (continued)

300s	10uN	10.00	2.50	6.00	1	0
	20uN	21.07	4.87	8.65	1	0.5
	30uN	30.63	7.33	11.33	2	0.6
	40uN	39.50	9.90	13.26	2	0.2

Table Appendix 1.3 Experimental scratch data for 90s exposure time

Scratch conditions	Applied normal force	Mean Fn (μN)	Mean Ft (μN)	Mean h (nm)	Error in Ft	Error in h
0s	10uN	13.00	2.00	4.61	0.8	0.4
	20uN	22.03	4.50	6.46	0.9	0.5
	30uN	30.77	7.60	8.73	1.00	1.3
	40uN	40.97	10.33	10.80	2.00	1.5
90s	10uN	11.00	1.83	6.61	0.8	0.3
	20uN	21.17	4.50	8.13	0.9	0.6
	30uN	31.23	6.97	9.88	1.0	1.0
	40uN	40.57	9.50	12.03	1.5	0.5

1b. Film thickness measurement data for 0.6wt% NH_4OH slurry

Table Appendix 1.4 Film thickness measurement data for 600s exposure time

F_n (μN)	10	20	30	40
h (nm)	9.0	12.0	14.1	15.2

Table Appendix 1.4 (continued)

t (nm)	8.5	7.3	8.0	6.5
$\sigma_{yf} / \sigma_{ys}$	0.51	0.45	0.45	0.45

Table Appendix 1.5 Film thickness measurement data for 300s exposure time

F_n (μN)	10	20	30	40
h (nm)	6.0	8.6	11.3	13.3
t (nm)	5	6.1	6.0	6.0
$\sigma_{yf} / \sigma_{ys}$	0.39	0.51	0.55	0.60

Table Appendix 1.6 Film thickness measurement data for 90s exposure time

F_n (μN)	10	20	30	40
h (nm)	6.61	8.13	9.88	13.3
t (nm)	5.0	5.2	5.0	5.0
$\sigma_{yf} / \sigma_{ys}$	0.46	0.61	0.77	0.73

2a. Experimental scratch data for 5wt% H_2O_2 slurry

Table Appendix 1.7 Experimental scratch data for 5wt% H_2O_2

Scratch conditions	Applied normal force	Mean Fn (μN)	Mean Ft (μN)	Mean h (nm)	Error in Ft	Error in h
0s	60uN	56.02	27.83	14.60	2.78	1.68
	80uN	77.47	40.50	15.55	4.05	1.53

Table Appendix 1.7 (continued)

	100uN	97.41	65.29	19.30	6.53	1.64
	120uN	116.83	72.99	21.56	7.30	2.26
75s	80uN	82.12	53.46	17.50	5.35	2.00
	100uN	98.11	60.63	22.12	6.06	1.08
	120uN	118.22	78.76	21.79	7.88	3.89
150s	60uN	58.40	32.21	16.48	3.22	1.69
	80uN	78.80	51.65	19.84	5.17	3.40
	100uN	98.26	73.09	21.66	7.31	3.08
	120uN	117.67	75.59	22.35	7.56	2.08
300s	60uN	57.84	34.68	20.71	3.47	1.84
	80uN	78.65	51.29	21.76	5.13	2.54
	100uN	96.78	71.26	24.54	7.13	3.11
	120uN	115.60	81.80	25.65	8.18	2.06

2b. Film thickness measurement data for 5wt% H_2O_2 slurry

Table Appendix 1.8 Film thickness measurement data for 300s exposure time

F_n (μN)	60	80	100	120
h (nm)	20.71	21.76	24.54	25.65
t (nm)	18.5	17.5	16.5	16
$\sigma_{yf} / \sigma_{ys}$	0.52	0.63	0.66	0.8

Table Appendix 1.9 Film thickness measurement data for 150s exposure time

F_n (μN)	60	80	100
h (nm)	16.48	19.84	21.66
t (nm)	15	14.5	13.5
$\sigma_{yf} / \sigma_{ys}$	0.65	0.69	0.8

Table Appendix 1.10 Film thickness measurement data for 75s exposure time

F_n (μN)	80	100
h (nm)	17.50	22.12
t (nm)	10.5	9
$\sigma_{yf} / \sigma_{ys}$	0.8	0.68

3a. Experimental scratch data for 1.0wt% HNO_3+ 0.5wt% BTA slurry

Table Appendix 1.11 Experimental scratch data for 600s exposure time

Scratch conditions	Applied normal force	Mean Fn (μN)	Mean Ft (μN)	Mean h (nm)	Error in Ft	Error in h
0s	40uN	38.10	16.00	19.32	1.60	1.93
	60uN	57.00	29.17	27.03	2.92	2.70
	80uN	77.00	39.50	32.30	3.95	3.23
	100uN	96.67	49.33	37.03	4.93	3.70
600s	40uN	37.00	18.50	24.91	1.85	2.49
	60uN	56.57	34.78	32.61	3.48	3.26
	80uN	77.33	46.30	34.49	4.63	3.45

Table Appendix 1.11 (continued)

	100uN	96.33	48.33	36.02	4.83	3.60

3b. Film thickness measurement data 1.0wt% HNO_3+ 0.5wt% BTA slurry

Table Appendix 1.12 Result for film thickness measurement

F_n (μN)	38.10	57.0
F_t (μN)	16.00	29.17
h (nm)	24.91	32.61
t (nm)	7.5	7.75
$\sigma_{yf} / \sigma_{ys}$	0.18	0.22

Appendix 2: Tip Radius Calibration.

The indenter tip radius is calibrated by scanning on a silicon calibration spike. The spike has an include angle less than 20 degrees, with tip radius less than 10nm. The interspacing between two adjacent spikes is about 2μm.

A typical image is shown in Fig appendix 2.1 below.

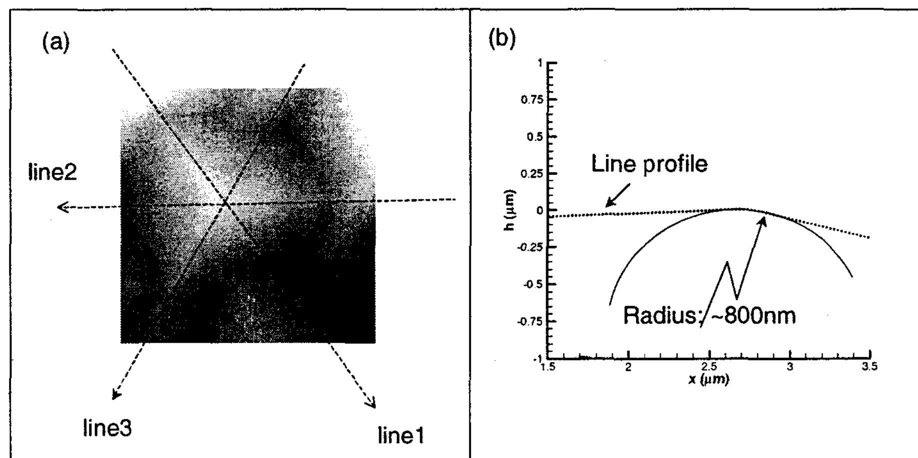

Fig appendix 2.1 Indenter tip shape (a) surface profile of indenter tip, (b) typical line profile across the top of the tip.

Fig appendix 2.1(a) shows the tip image by scanning on a calibration spike. Three line profiles across the top of the tip are plot as shown in Fig appendix 2.1(a). Then the line profiles close to the top of the tip are fitted with a circle to find the radius as shown in Fig appendix 2.1(b). All three line profiles yield the same tip radius, approximately 800nm.